Collision induced dissociation of polycyclic aromatic hydrocarbons in a quadrupolar ion trap : Differentiation of isomeric structures in cosmic dust components

Mickaël Carlos

THÈSE

En vue de l'obtention du

DOCTORAT DE L'UNIVERSITÉ DE TOULOUSE

Délivré par : *l'Université Toulouse 3 Paul Sabatier (UT3 Paul Sabatier)*

Présentée et soutenue le *03/02/2020* **par :**

MICKAËL CARLOS

Dissociation induite par collisions d'hydrocarbures aromatiques polycycliques dans un piège à ions quadripolaire. Séparation des structures isomériques des composantes de la poussière cosmique.

JURY

M. CRISTIAN FOCSA	Professeur	Rapporteur
M. SERGE MARTIN	Directeur de Recherche	Rapporteur
MME JOËLLE MASCETTI	Directeur de Recherche	Rapporteure
M. JOSE CERNICHARO	Professeur	Examinateur
M.PAUL M. MAYER	Professeur	Examinateur
M. J.-M. L'HERMITE	Directeur de Recherche	Examinateur
MME CHRISTINE JOBLIN	Directrice de Recherche	Directrice de thèse
M. HASSAN SABBAH	Maître de Conférence	Co-directeur de thèse

École doctorale et spécialité :
SDU2E : Astrophysique, Sciences de l'Espace, Planétologie

Unité de Recherche :
IRAP(UMR)

Directeur(s) de Thèse :
Christine Joblin et *Hassan Sabbah*

Rapporteurs :
Mme Joëlle MASCETTI, *M. Serge MARTIN* et *M. Cristian FOCSA*

à Rafaël,
Sacha, Agostinho, Joaquim,
ma femme et toute ma famille.

Acknowledgments

Many people have inspired me through my thesis and lift me to be able to perform all this work, I hope I will not forget to mention anyone because I will not forget meeting them. First I would like to thank Dr Christine Joblin and Dr. Hassan Sabbah for their trust and patience. The constant debate and guidance helped me to see through the process of getting the marrow of my work leading me here today. Thank you for pushing me, showing me that I always have to be painstacking in my research and in understanding things. Thank you both for participating in showing me both sides of astrophysics. Then I would like to than Patrick Moretto-Capelle my Ph.D. godfather, for the shared moments, teachings and jokes. I would like to give a very special thank you to Josette Garcia for always being there to answer to my numerous questions and administrative issues, secondly I'd like to thank here for her zest for life and her friendship. Then I would like to thank Dr Generiere Soucail and the people from the école doctorale SDU2E for their understanding.

Separately I would like thank both laboratories I had the opportunity to be appart. First in the LCAR, thanks to the interesting discussions about science (or not) to Jean-Marc L'Hermite, Sebastien Zamith, Juliette Billy, Bruno Lepetit, Pierre Cafarelli. Special thank you to my appraised fellow Ph.D. students, to name a few: Olivier, Eric M & Qi, Eric M, Julien, Evgeny, Maxime, Julie, Maxime, Vincent, Gabriel, Pierrot, Bastien for coffee, frisbee interreds, football tricks, for always making me smile, for the music and discussions.

Again for all their help and support I'd like to thank Patricia, Fanny, Malika and Emmanuelle. In the engineering department I would like to thank Daniel, Laurent, Stéphane and Michel.

In IRAP, special thank to Loic Noget and Anthony Bonamy for their patience and help. Thanks to Karine Demyk, Olivier Berné, Isabelle Ristorcelli for making me feel home. Then I would like to point out some people which from accompanied me through this journey: Shubadip, Rémi, Mingchao, Sacha, Gaby, Fabrizio, Dianailys, Sujay, Sarah, Paolo, Abraham. Thank you very much for all this moments.

I would like to adress a special thank you to the people from the europah project and the people met at the europah Ecole de physique des Houches for the friendship, the discussions and the scientific exchanges thanks to Ambra, Ameek, Dario, Elena, Frederik, Georgios, Julianna, Lindsey, Lorenzo, Martin, Ozan, Rijutha, Rushdi, Sanjana, Shreyak, Thiebaut, Thomas, Yaolin.

Thank you very much to each and every one of the people a could meet during this Ph.D.

I acknowledge support from the European Research Council under the European Union's Seventh Framework Programme ERC-2013-SyG, Grant Agreement n. 610256 NANOCOSMOS". I acknowledge support from La Region Occitanie, Grant n. 15066466. Finally, all the comic strips are used with the permission of Jorge Chan, check out his website 'Piled Higher and Deeper', www.phdcomics.com

Contents

Description [fr]

Le cycle de vie et de mort des étoiles est intimement lié à l'évolution physico-chimique de la matière. Cette évolution concerne la synthèse d'éléments lourds comme le fer dans les processus de nucléosynthèse stellaire. D'autre part, la matière se complexifie formant une grande variété de molécules ainsi que des petits grains de poussière. Le carbone est un élément central de cette matière. La majorité des molécules observées sont des molécules organiques. De plus le milieu interstellaire est peuplé de très grandes molécules carbonées de type hydrocarbures aromatiques polycycliques (HAP) qui sont révélées par des bandes à 3.3, 6.2, 7.7, 8.6 et 11.3 μm qui sont observées en émission sous l'excitation des photons ultraviolets des étoiles jeunes. Le carbone est également impliqué dans la formation des poussières dans l'enveloppe des étoiles de la branche asymptotique des géantes (étoiles AGB) et dont le rapport carbone-oxygène est supérieur à 1. Ces grains carbonés ont un lien possible avec la formation des HAP comme cela est connu dans notre environnement pour le cas des suies. Le modèle HAP en astrophysique est confronté jusqu'à ce jour au manque d'identification d'espèces individuelles de cette famille. Il faut noter cependant que l'identification de signatures spectrales spécifiques du fullerène C_{60} et de son cation confirme la présence de grandes molécules carbonées dans les milieux astrophysiques. La question des mécanismes mis en jeu dans la formation des HAP et des fullerènes dans ces milieux est donc cruciale.

Le projet NANOCOSMOS financé par le Conseil européen de la recherche a pour objectif de mieux comprendre les processus qui mènent à la formation des poussières d'étoiles en général et des HAP en particulier. Le projet combine l'observation détail-

lée de la composition moléculaire et des conditions physiques des enveloppes d'étoiles AGB à des expériences de laboratoire afin d'élucider les mécanismes chimiques mis en jeu et de produire des analogues de ces poussières. Plusieurs scénarios ont été proposés pour rendre compte de la formation des HAP dans les processus de combustion comme le mécanisme HACA (*hydrogen abstraction carbon addition*). Dans le projet NANOCOSMOS, différents réacteurs sont utilisés pour produire des poussières et la machine Stardust a été construite spécifiquement pour simuler la chimie des AGB. Le contenu moléculaire des échantillons produits est ensuite analysé avec le dispositif AROMA qui est au centre de ce travail de thèse.

Le dispositif AROMA présente la particularité de combiner des techniques laser pour la production des ions, un piège ionique et un spectromètre de masse par temps de vol. La source d'ions est constituée d'un laser à 1064 nm qui permet une désoprtion douce des espèces moléculaires et d'un laser à 266 nm qui permet une ionisation efficace dans le cas des HAP. Les ions peuvent ensuite être stockés dans le piège à ions avant d'être transférés vers la partie spectrométrie de masse. L'objectif de ce travail de thèse est de tirer profit du piège d'AROMA afin de réaliser des expériences de dissociation induite par collisions (CID pour *collision induced dissociation*) qui pourraient être utilisées pour obtenir des informations complémentaires sur la structure des molécules analysées par spectrométrie de masse. En particulier, un certain nombre d'échantillons étudiés y compris des météorites comme Murchison et Allende, présentent un pic en masse dominant à m/z = 202 qui correspond à la formule chimique $C_{16}H_{10}$. Plusieurs isomères sont possibles dont le pyrène et le fluoranthène qui sont souvent considérés comme les composants principaux des différents échantillons (synthétiques ou naturels) qui ont été étudiés dans ce travail. De structures compactes, l'un peut être considéré comme précurseur des grands HAP plans et l'autre de structures carbonées à trois dimensions (espèces intermédiaires vers les fullerènes) qui sont favorisées par la présence d'un cycle à cinq carbones.

Ce travail s'articule autour d'une caractérisation de l'utilisation du dispositif AROMA et de la mise en place d'une procédure expérimentale CID. Le chapitre II présente une description détaillée du dispositif AROMA, de ses fonctionnalités et de ses performances. Le chapitre III présente ensuite la procédure CID comprenant l'isolation de

l'espèce parent à 1 m/z et une optimisation du refroidissement des ions afin d'améliorer le contrôle du processus de dissociation. La CID est activée par collisions obtenues par l'accélération des ions piégés en présence d'un gaz rare (Ar, He). Nous avons exploré différentes conditions d'excitation. Avec une excitation hors résonance une cascade de dissociation est observée mais ne permet pas de tracer l'origine de chaque fragment. Nous avons donc préféré des expériences d'excitation en résonance qui permettent *a priori* de cibler les ions parents que l'on souhaite exciter. Il faut néanmoins pour cela utiliser un voltage très bas qui est à la limite de la stabilité du voltage de piégeage. Nous avons donc utilisé un voltage un peu plus élévé pour notre travail de différenciation des isomères à m/z = 202.

Le chapitre IV est consacré à l'étude de la différenciation par CID de trois isomères de $C_{16}H_{10}$ que sont les deux structures compactes : pyrène et fluoranthène, ainsi que la structure alkylée du 9-éthynylphénanthrène. Nos études montrent que la présence de ce dernier peut être facilement mise en évidence mais qu'il est beaucoup plus compliqué de différencier les deux isomères compacts même en utilisant des énergies de collision plus élevées. En plus des corps purs et de leurs mélanges, nous avons analysé des échantillons complexes produits dans un plasma poussiéreux d'acétylène et provenant de la météorite Allende. Les résultats obtenus montrent que pour tous ces échantillons sauf un du plasma poussiéreux le pic à m/z = 202 comprend principalement des structures condensées comme le pyrène et le fluoranthène.

Au cours de ce travail de thèse, des simulations numériques correspondant aux expériences effectuées ont été menées afin de mieux appréhender le comportement des ions dans le piège. Ceci comprend la simulation de la dynamique des ions dans le piège avec ou sans gaz, ainsi que l'accélération des ions lors de la procédure CID. De cette modélisation nous avons pu extraire des distributions d'énergie cinétique des ions et de temps de collision. Nous avons utilisé ces distributions dans une méthode Monte-Carlo à deux dimensions qui calcule l'augmentation de l'énergie interne en fonction des conditions expérimentales. Ces simulations sont présentées dans le chapitre V et nous ont permis d'obtenir un certain nombre de résultats. En particulier, nous avons mis en compétition l'augmentation d'énergie interne lors de l'excitation des ions avec leur taux de dissociation. Nous avons ainsi pu ajuster les courbes de dissociation

du pyrène mesurées dans nos expériences en optimisant la valeur du paramètre η. Ce paramètre représente le taux de transfert entre énergie cinétique et énergie interne dans nos conditions expérimentales. Nous avons montré que la même valeur du paramètre η permet de rendre compte de la courbe de dissociation du fluoranthène. Dans le cas du 9-éthynylphénanthrène, nous avons pu déterminer un taux de dissociation en accord avec l'énergie d'activation prévue pour cet ion.

Enfin, le chapitre VI conclut ce travail et propose quelques perspectives.

List of Tables

List of Figures

Chapter I

Introduction

Contents

"Piled Higher and Deeper"by Jorge Cham www.phdcomics.com

1.1 Astrophysical context

From the big bang to nowadays, the study of the universe and its history, helps us understanding the laws of physics and testing our models. Each piece of information that we can get about the outer space gives us new fitting constrains that helps us to "converge" towards the best models. In the following, we briefly describe the evolution of interstellar matter that is intimately coupled to the star life cycle. This matter is composed of gas and tiny dust particles.

1.1.1 Cycles of star life and interstellar matter

The evolution of matter in a galaxy is intimately linked to the star life cycle (see Fig. 1.1). Dense molecular clouds can collapse by gravitational instability and form new stars with associated planetary systems. These stars are powered by nuclear fusion reactions, burning hydrogen in their main sequence stage and then helium and heavier elements in more evolved stages. Depending on the mass of the star, low- and medium-mass versus high-mass ($M>8M_{\odot}$), the star will evolve on the Asymptotic Giant Branch branch of the Hertzsprung–Russell diagram (later AGB stars) or become a supernova. AGB stars are characterized by a strong mass loss, leading to the formation of large circumstellar envelopes. These envelopes are the sites of formation of molecules and dust grains that are then ejected into the diffuse interstellar medium (ISM). The

elemental composition of these envelopes depends on the evolution stage of the central star, leading to either oxygen-rich or carbon-rich envelopes. The AGB star will evolve into a relatively short-lived post-AGB phase. Then the mass-loss process will stop and the object will evolve into a planetary nebula powered by a very hot central star.

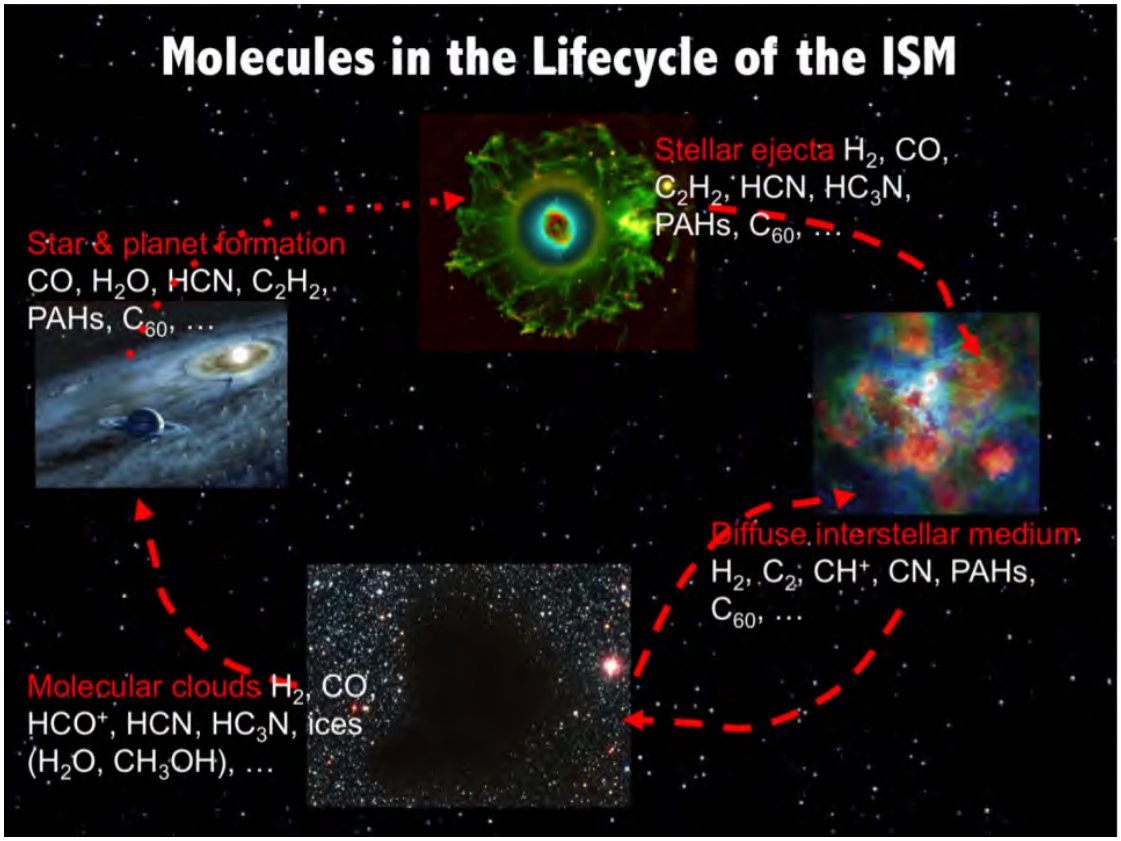

Figure 1.1 The lifecycle of the interstellar medium (ISM) is related to the star evolution from their formation in molecular clouds to the end of their life when they eject matter either in the form of a wind or through a supernova explosion in the case of massive stars ($M>8M_\odot$). During its stay in the ISM (τ ~100 Myr), the matter circulates between diffuse phases and denser molecular clouds, which are the nursery of new stars. Once formed, stars evolve on a few billion years timescale for a low mass star such our Sun. Different molecules can be used to trace the different steps in the lifecycle of the ISM as illustrated here. From Tielens [2013].

High-mass stars will lead to supernova explosion at the end of their lives. Supernovae are a major source of heavy elements in the interstellar medium from oxygen through to rubidium. All the matter ejected from dying stars will replenish the ISM in new matter, that will form new clouds that can at some point lead to the formation of new stars. The matter therefore cycles within one galaxy in close relation with the stellar evolution cycle.

1.1.2 Interstellar molecules and dust

Interstellar matter is mainly composed of hydrogen and helium, the main constituents at the birth of the Universe. The other elements (C, N, O, Fe, Mg, Si, S...) that were synthesized by the successive generations of stars represent only 1.5 % of the mass of the ISM. These are the building blocks for an increased complexity leading to a large variety of molecules and dust grains. The list of molecules that were detected so far in the ISM as well as in circumstellar environments is given in Table 1. A large number of these molecules are organic. The largest molecule identified so far is the fullerene C_{60} and its cation C_{60}^+ (and possibly C_{70}, cf. Sect. 1.1.3). Identified aromatic molecules are limited to benzene (Cernicharo et al. [2001]) and benzonitrile (McGuire et al. [2018]).

Interstellar space is populated by tiny dust grains, less than 1 μm in size. It is generally considered that dust grains are formed in evolved stars and evolve in the different phases of the ISM (see Fig. 1.1). The grains absorb and scatter stellar light, in particular in the visible and ultraviolet (UV), and reemit their energy in the infrared (IR). The combined study of the extinction curve with the IR emission spectrum has led to models in which the grains are described by three main populations (Desert et al. [1990]; Draine and Li [2007]; Compiègne et al. [2011]). These populations consist of large grains of typical size 0.1 μm composed of silicates and covered by amorphous carbon, very small grains of sizes between a few and a few tens of nanometers made of carbon and including possibly metals, and large carbonaceous molecules such as polycyclic aromatic hydrocarbons (PAHs) as discussed in the next section.

Dust grains play a key role in the chemistry. They are responsible for the production of the simplest molecule, H_2 (Wakelam et al. [2017]). In dense molecular clouds which are protected from UV photons, the grains are very cold. Atoms and molecules stick to their surface forming icy mantles (cf. Fig. 1.2). The ices are formed through accretion and grain surface chemistry which can build new molecules. Molecular complexity is expected to increase upon energetic processing including UV irradiation, cosmic ray bombardment and thermal processing (Ehrenfreund and Charnley [2000]). In particular, when new stars form, the evolution of the ices in the circumstellar envelopes and disks of young stellar objects is dominated by thermal processes with a possible con-

tribution of UV irradiation especially in the environment of high-mass stars (Boogert et al. [2015]). These complex molecules are expected to be common ingredients for new planetary systems (Herbst and van Dishoeck [2009]).

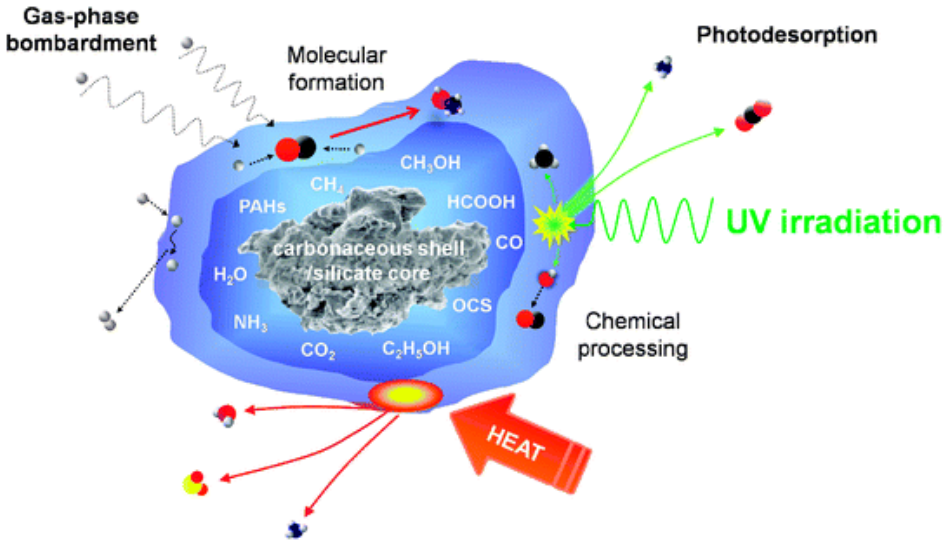

Figure 1.2 Scheme of an icy interstellar grain and the mechanisms involved in its processing. The labelled molecular species represent the most common species detected in interstellar ices. From Burke and Brown [2010].

2 atoms	3 atoms	4 atoms	5 atoms	6 atoms	7 atoms	8 atoms	9 atoms	10 atoms	11 atoms	12 atoms	12+ atoms
H_2	C_3^*	c-C_3H	C_5^*	C_5H	C_6H	CH_3C_3N	CH_3C_4H	CH_3C_5N	HC_9N	c-$C_6H_6^*$	C_{60}^*
AlF	C_2H	l-C_3H	C_4H	l-H_2C_4	CH_2CHCN	$HC(O)OCH_3$	CH_3CH_2CN	$(CH_3)_2CO$	CH_3C_6H	n-C_3H_7	C_{70}^*
AlCl	C_2O	C_3N	C_4Si	$C_2H_4^*$	CH_3C_2H	CH_3COOH	$(CH_3)_2O$	$(CH_2OH)_2$	C_2H_5OCHO	i-C_3H_7CN	C_{60}^{+*}
C_2^{**}	C_2S	C_3O	l-C_3H_2	CH_3CN	HC_5N	C_7H	CH_3CH_2OH	CH_3CH_2CHO	$CH_3OC(O)CH_3$	$C_2H_5OCH_3$	c-C_6H_5CN
CH	CH_2	C_3S	c-C_3H_2	CH_3NC	CH_3CHO	C_6H_2	HC_7N	CH_3CHCH_2O			
CH^+	HCN	$C_2H_2^*$	H_2CCN	CH_3OH	CH_3NH_2	CH_2OHCHO	C_8H	CH_3OCH_2OH			
CN	HCO	NH_3	CH_4^*	CH_3SH	c-C_2H_4O	l-HC_6H^*	$CH_3C(O)NH_2$				
CO	HCO^+	HCCN	HC_3N	HC_3NH^+	H_2CCHOH(?)	CH_2CHCHO(?)	C_8H^-				
CO^+	HCS^+	$HCNH^+$	HC_2NC	HC_2CHO	C_6H^-	CH_2CCHCN	C_3H_6				
CP	HOC^+	HNCO	HCOOH	NH_2CHO	CH_3NCO	H_2NCH_2CN	CH_3CH_2SH(?)				
SiC	H_2O	HNCS	H_2CNH	C_5N	HC_5O	CH_3CHNH	CH_3NHCHO				
HCl	H_2S	$HOCO^+$	H_2C_2O	l-HC_4H^*	$HOCH_2CN$	CH_3SiH_3 (2017)	HC_7O				
KCl	HNC	H_2CO	H_2NCN	l-HC_4N	$H_2NC(O)NH_2$						
NH	HNO	H_2CN	HNC_3	c-H_2C_3O							
NO	MgCN	H_2CS	SiH_4^*	H_2CCNH (?)							
NS	MgNC	H_3O^+	H_2COH^+	C_5N^-							
NaCl	N_2H^+	c-SiC_3	C_4H^-	HNCHCN							
OH	N_2O	CH_3^*	HC(O)CN	SiH_3CN							
PN	NaCN	C_3N^-	HNCNH	C_5S (?)							
SO	OCS	PH_3	CH_3O	MgC_4H							
SO^+	SO_2	HCNO	NH_4^+								
SiN	c-SiC_2	HOCN	H_2NCO^+								
SiO	CO_2^*	HSCN	$NCCNH^+$								
SiS	NH_2	H_2O_2	CH_3Cl								
CS	H_3^+(*)	C_3H^+	MgC_3								
HF	SiCN	HMgNC									
HD	AlNC	HCCO									
FeO?	SiNC	CNCN									
O_2	HCP	HONO									
CF^+	CCP	MgC_2H									
SiH?	AlOH										
PO	H_2O^+										
AlO	H_2Cl^+										
OH^+	KCN										
CN^-	FeCN										
SH^+	HO_2										
SH	TiO_2										
HCl^+	C_2N										
TiO	Si_2C										
ArH^+	HS_2										
N_2	HCS										
NO^+?	HSC										
NS^+	CO										
HeH^+	aNC										

Table 1 Molecules detected in the interstellar medium and circumstellar shells (as of 10/2019). Extracted from the Cologne Database for Molecular Spectroscopy. https://cdms.astro.uni-koeln.de/classic/molecules

1.1.3 Aromatic Infrared bands, C_{60} and the astro-PAHs

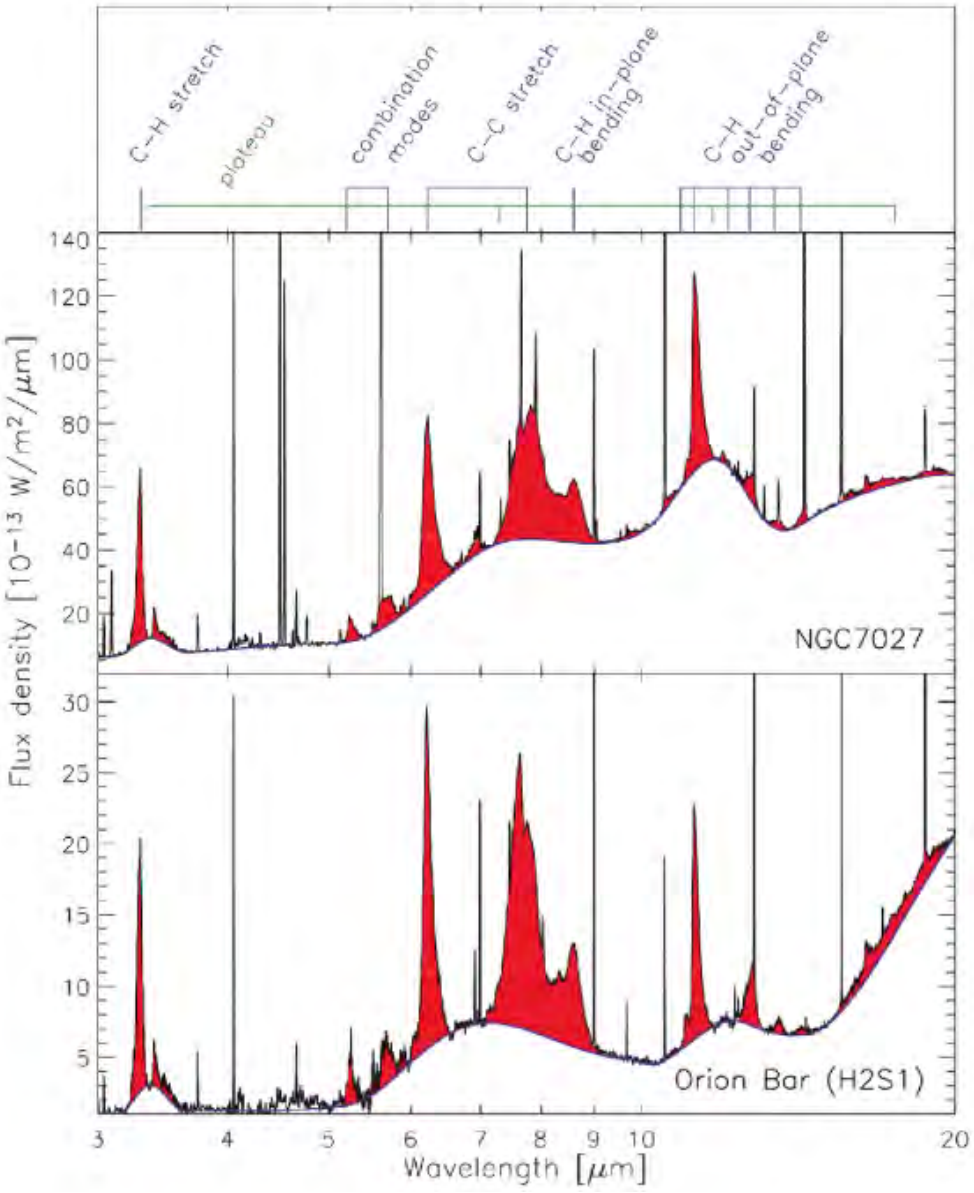

Figure 1.3 The mid-IR spectra of UV-irradiated regions such as the Orion bar associated with a massive star-forming region and the planetary nebula NGC 7027 (evolved star), are dominated by emission features that are assigned to aromatic CC and CH modes. More specifically, these bands are attributed to polycyclic aromatic hydrocarbons (PAHs). The underlying broad plateaus and continua are likely due to carbonaceous nanograins including PAH clusters. From Peeters et al. [2004].

The aromatic infrared bands (AIBs) are a set of emission features in the mid-IR that are well observed in regions that are submitted to UV irradiation (cf. Fig. 1.3; Peeters et al. [2004]). The positions of the AIBs at 3.3, 6.2, 7.7, 8.6 and 11.3 μm are characteristic of aromatic CC and CH bonds. In addition, the emission mechanism implies that the carriers are of small (molecular) size (Sellgren [1984]). Leger and Puget

[1984] and Allamandola et al. [1985] proposed the PAH model in which the AIBs arise from the radiative vibrational emission from PAHs excited by UV irradiation. Examples of PAH structures are provided in Fig. 1.4. PAHs are expected to be the most abundant molecules after H_2 and CO (Leger et al. [1989]).

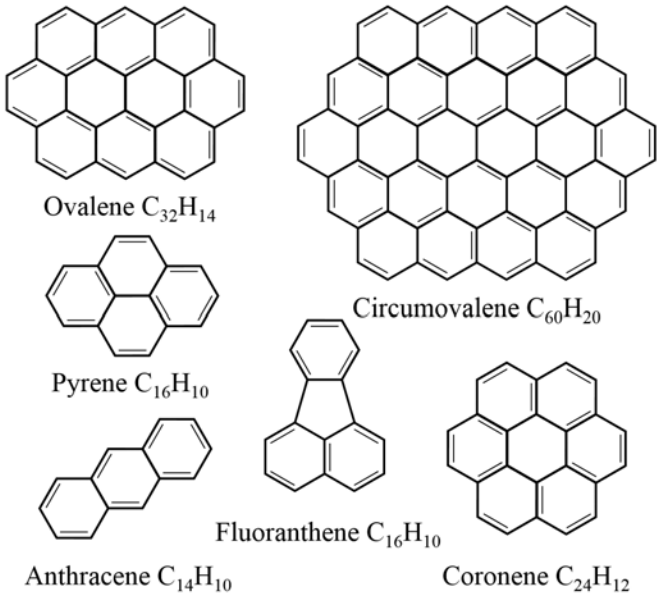

Figure 1.4 Examples of PAHs with their structures and chemical formulae.

The main drawback with the PAH model is that so far no individual molecules could be identified from neither the analysis of the AIB spectra nor the identification of diffuse interstellar bands through the near-UV to near-IR range with specific electronic transitions of PAHs (Salama et al. [1999]; Salama et al. [2011]). Some related fullerene species were however recently detected, which confirmed the presence of large carbonaceous molecules in the gas-phase and the excitation mechanism as proposed in the PAH model. C_{60} was the first to be identified thanks to its four IR active modes. The emission bands were found to be especially intense and not mixed with PAH emission in the planetary nebula Tc 1 (Fig. 1.5; Cami et al. [2010]). The authors discussed that C_{70} could be present as well although its assignment remains tentative. The IR bands of C_{60} have been detected in star-forming regions (Sellgren et al. [2010]; Castellanos et al. [2014]), in evolved stars (García-Hernández et al. [2011b]; García-Hernández et al. [2011a]; Otsuka et al. [2014]) and in the diffuse ISM (Berné et al. [2017]), which shows that this large molecule is present in various environments.

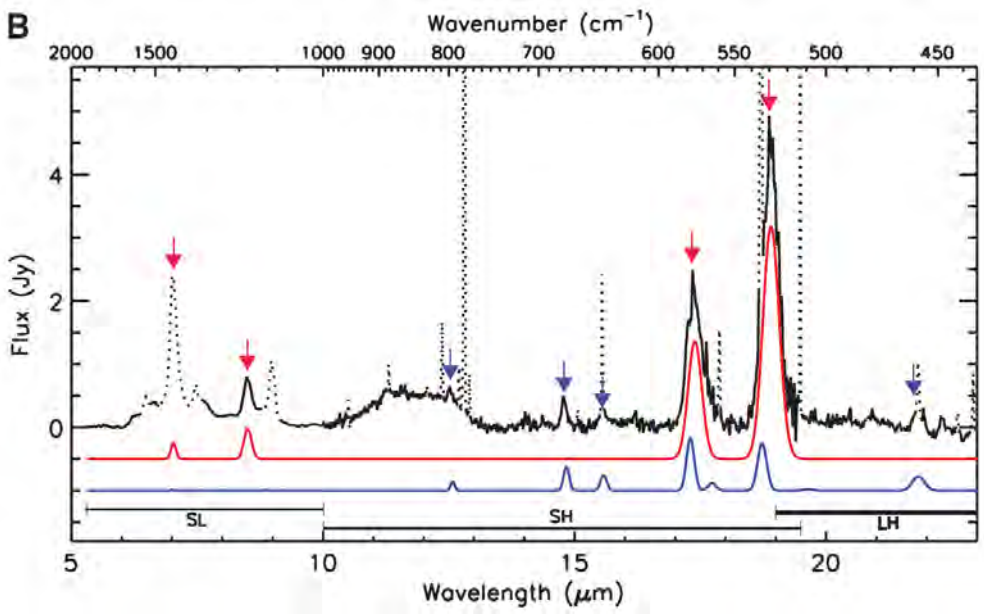

Figure 1.5 Detection of the four IR active bands of C_{60} (in red) in the planetary nebula Tc1 and tentative detection of C_{70} bands (in blue). From Cami et al. [2010].

1.2 The key question of the formation of astro-PAHs

1.2.1 Insight from combustion chemistry

Polycyclic aromatic hydrocarbons (PAHs) are organic compounds containing only carbon and hydrogen and are composed of two or more fused aromatic rings (cf. Figure 1.4). They have received increased attention in recent decades in air pollution studies due to their carcinogenicity and mutagenicity. They are produced during pyrolysis and combustion of organic matter, fossil fuels, petrochemicals and open biomass burning.

PAHs in space are supposed to be formed in the circumstellar envelopes (CSE) of AGB stars. A combustion-like process (Frenklach and Feigelson [1989]; Cherchneff et al. [1992]) has been proposed to describe their formation, in which small hydrocarbon carbon chains (e.g., acetylene C_2H_2) form PAHs that nucleate into larger-size PAHs and, ultimately, into soot-like nanograins. Several chemical pathways have been proposed to describe the formation and growth of these species in the combustion and laboratory astrophysics communities. The hydrogen-abstraction/acetylene-addition (HACA) mechanism (Frenklach and Wang [1991]) has been exceptionally cited. In this model, a key role has been given to mid-size PAHs, especially pyrene ($C_{16}H_{10}$), in the formation of the critical nucleus from the gas phase ensuring the transition toward the

solid phase (Frenklach and Wang [1991], Wang and Frenklach [1997]). The detailed mechanism describing the gas-phase chemistry includes the pyrolysis and oxidation of species with one or two carbons, the formation of higher, linear hydrocarbons up to six carbon species, the formation of benzene C_6H_6 and further reactions leading to PAHs, as well as the oxidation pathways of the aromatic species. The difference between an acetylene flame and the CSE of a carbon-rich AGB star is the presence of oxygen in the former, which is absent in the latter, where it is locked in the very stable CO molecule.

Alternative models have been proposed to explain PAH growth in flames. These include the phenyl-addition-cyclization (PAC) mechanism (Shukla et al. [2008]; Shukla and Koshi [2010]), the methyl-addition-cyclization (MAC) mechanism, which involves the addition of two or three methyl radicals on PAHs. Recently a new mechanism has been presented, known as the hydrogen-abstraction-vinylacetylene-addition (HAVA) (Zhao et al. [2018]) to explain the growth from pyrene to more complex PAHs such as benzo(e)pyrene $C_{20}H_{10}$. HAVA has an advantage for low-temperature environments as explained in Shukla and Koshi [2012a] because it represents a barrier-less reaction pathway and leads to PAH growth through six-membered ring expansions via a single collision event (Kaiser et al. [2015], Kaiser et al. [2012]). It could therefore be a relevant process in the ISM.

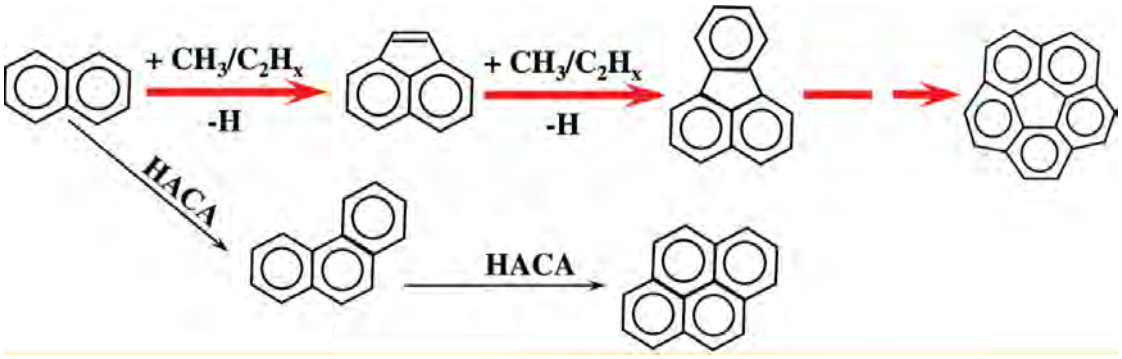

Figure 1.6 Presentation of the HACA and HAVA processes in the growth of PAHs from naphthalene. The red arrow means that HACA, HAVA and MAC can be involved. From Shukla and Koshi [2012a].

1.2.2 Investigation in laboratory astrophysics

Different activities are carried out in the laboratory in relation with the formation of cosmic dust as shown in Table 2. Some consist in the production of cosmic dust

analogues. Others focus on the study of the kinetics of individual reactions in particular in the case of the formation of PAHs Marin et al. [2020].

Several techniques have been used for the production of dust analogues as summarized in Table 2 from Martínez et al. [2019]. The Table presents the precursors used, the temperature range at which the experiments have been carried out and specifies if ionic species were involved in the chemistry. The involved pressure is not specified since its value is poorly defined. The list of references within the table is representative but not exhaustive. In the inner layers of CSEs, dust nucleation is driven by neutral-neutral reactions in the temperature range ∼1500-2500 K. These conditions differ from most of the techniques presented in Table 2. The Stardust machine though has been specifically designed to approach them Martínez et al. [2018]. In particular, thermalized atoms are used as precursors for dust formation.

Technique	Precursors	T(K)	Ion chemistry	Wall effect	Refs
Laser ablation	Graphite + quenching gas	$\geq$ 4000K	Yes	No	Kroto et al. [1985], Jager et al. [2008]
Combustion/ Flames	Hydrocarbons	1800-2500K	weak	No	Carpentier et al. [2012]
Pyrolysis (laser induced)	Hydrocarbons	1000-1700 $\geq$ 3500	no	depending on reactor	Jager et al. [2006], Jäger et al. [2009]
Pyrolysis	Hydrocarbons	600-2000K	no	depending on reactor	Biennier [2009]
Dusty Plasmas	Hydrocarbons	600-2000K	weak	yes	Kovačević et al. [2005],Contreras and Salama [2013], Maté et al. [2016]
SGAS: Sputter Gas aggregation sources Stardust	Graphite + H_2	$\leq$ 1000K	weak/no	No	Martínez et al. [2018]

Table 2 Comparison between typical laboratory techniques used to synthesize cosmic dust analogues. From Martínez et al. [2019]

1.2.3 PAHs in meteorites

The content of meteorites in organics has been previously reviewed (Pizzarello et al. [2006], Sephton [2005]). A variety of techniques have been employed to probe the

presence and nature of aromatic hydrocarbons, including PAHs. Solvent or supercritical fluid extraction combined to gas-chromatography mass spectrometry (GC-MS) have been used (Pizzarello et al. [2006]). Correlations between the detected molecular weight of aromatic compounds and the extraction methods have been observed. Using these techniques, Basile et al. [1984] detected 30 polycyclic aromatic compounds in a Murchison solvent extract with fluoranthene and pyrene as the most abundant components. A series of studies on carbonaceous chondrites has been achieved in the 1980s and 1990s on Murchison and Antarctic CM2 meteorites. In all cases, the most abundant compounds in the extracts were phenanthrene, fluoranthene and pyrene (Sephton [2002]).

Laser desorption laser ionization mass spectrometry (L2MS) has become a powerful tool to detect and characterize the distribution of PAHs and related aromatic species in meteorites and extraterrestrial materials (Spencer et al. [2008]). It requires minimal sample processing and handling, thus minimizing the risk of additional sample contamination. It offers the advantage of studying the spatial distribution of the detected species. It has been shown to be the most sensitive method for these compounds (attomoles range) (Sabbah et al. [2017]). However, this technique lacks the possibility of isomeric differentiation for which the most reliable method is provided by GC-MS. Still, in a recent work (Sabbah et al. [2017]) showed the capability of L2MS to demonstrate that pyrene is the most abundant isomeric species at m/z = 202 in Murchison. This has been done using collision induced dissociation in the AROMA setup, which is at the core of this work.

The Murchison meteorite has been the most extensively studied chondrite for its aromatic content, but PAH studies have also been performed on a variety of chondrites. The list of species found in these chondrites includes benzene, toluene, alkyl benzenes, and PAHs such as naphthalene, phenanthrene, pyrene, and alkylated derivatives, and larger PAHs with up to 5 and 6 rings (Basile et al. [1984], Naraoka et al. [2000]). Using GC-MS, Naraoka et al. [2000] examined the molecular and carbon isotopic abundances of PAHs in Asuka (A)-881458, an Antarctic carbonaceous chondrite. They identified more than 70 PAHs ranging from naphthalene to benzo(ghi)perylene, with fluoranthene and pyrene being the most abundant. They concluded that two reaction pathways of

extraterrestrial PAH formation can be distinguished leading to respectively the "pyrene series" and the "fluoranthene series".

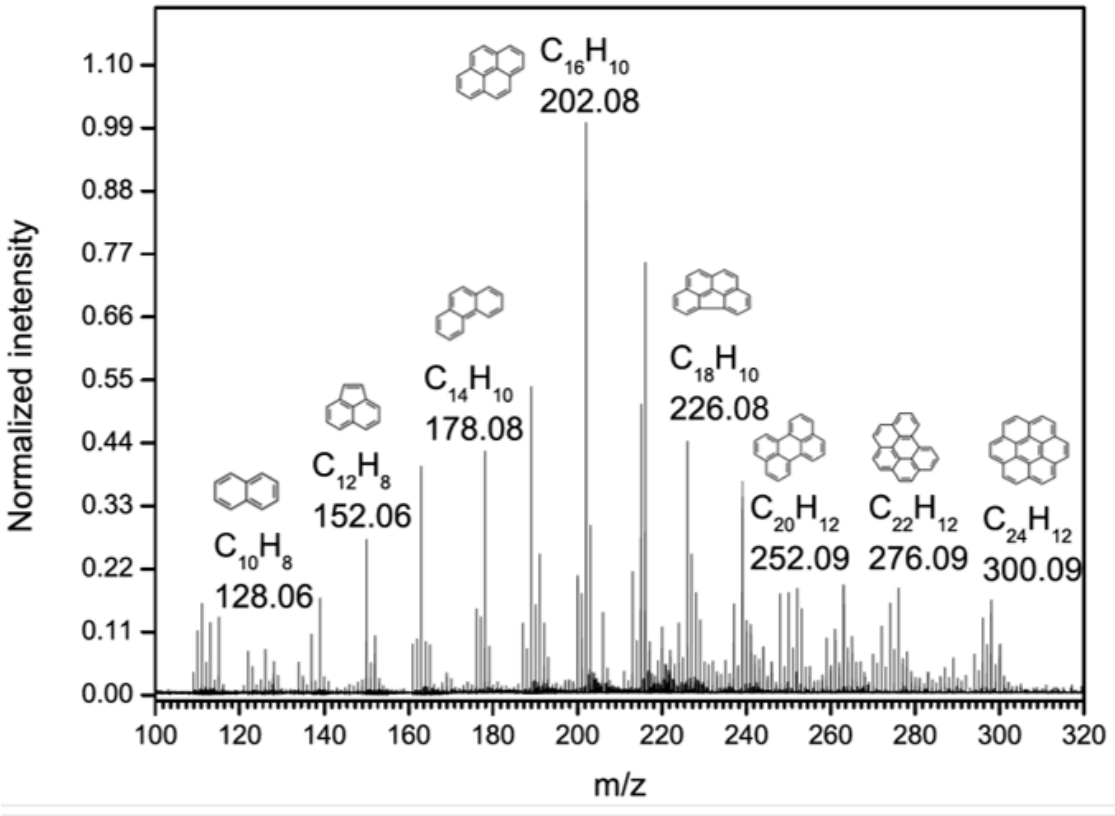

Figure 1.7 Analysis of the PAH content in the Murchison meteorite using the AROMA setup (Sabbah et al. [2017]).

1.2.4 The key m/z=202 species

The peak at m/z = 202 is found to be a dominant PAH peak in samples such as soot samples Faccinetto et al. [2011] and cosmic dust analogues Pino et al. [2019]. It is also a dominant peak in the Murchison (Sabbah et al. [2017]) meteorite. A key role has been attributed to this PAH, often identified as pyrene, in models of soot formation. In particular, Frenklach and co-workers (Frenklach [2002]) proposed that the nucleation of soot occurs via physical association of PAHs as small as pyrene. However, a combined experimental and theoretical study on pyrene dimerization (Sabbah et al. [2010]) has seriously challenged this model by showing that pyrene molecules cannot condense efficiently at temperatures characteristic of combustion environments (>1000 K). Therefore, other chemical pathways are required for PAH growth and soot

nucleation at high temperature.

In this respect, a recent work on pyrene synthesis at high temperature (1400 K) show that along with the HAVA mechanism, molecular mass growth processes from pyrene may lead through systematic ring expansions to more complex PAHs and ultimately to 2D graphene-type structures (Zhao et al. [2018]).

Different pathways lead to different isomers at m/z = 202, i.e. pyrene and fluoranthene (Shukla and Koshi [2012b], cf. Figure 1.6). These will then lead to the formation of different species along formation pathways. For instance, a route to the formation of fullerenes such as C_{60} could be driven by fluoranthene (Shukla and Koshi [2012b]) thanks to the appearance of the first 5-carbon ring which enables 3D structures. From fluoranthene and via the HACA mechanism, the two consecutive species at m/z = 226 and 250 should most probably be benzo[ghi]fluoranthene and corannulene. The latter, is a part of C_{60} fullerene structure and an essential component of the curved graphene layers observed in soot particles in the core region (Müller et al. [2007]).

1.3 Framework

1.3.1 The NANOCOSMOS project

NANOCOSMOS is a project that is supported by the European Research Council over the 2014-2020 period. It relies on a synergy between CSIC in Madrid under the responsibility of José Cernicharo and José-Àngel Martín Gago and CNRS in Toulouse under the responsibility of Christine Joblin. NANOCOSMOS combines new observational strategies with state-of-art laboratory studies to change our view on the origin and evolution of stardust. A major topic concerns the production of stardust analogues in the laboratory and the identification of the key species and steps that govern the formation of these nanograins. As introduced in Sect. 1.2.2 the Stardust machine in Madrid (Martínez et al. [2018]) is an innovative setup that has been designed to simulate dust formation in the atmosphere of evolved stars. Other reactors are used in the project to get insights into the chemistry that leads to the formation of nanograins in general and PAHs in particular. These involve the cold plasma reactors at Laplace (Calafat et al. [2007]; Despax et al. [2012]).

The dust samples that are produced in the different reactors are analyzed at the molecular level using the AROMA setup, another machine that has been build in Toulouse for NANOCOSMOS. This hybrid mass spectrometer has been at the center of my PhD work as described below.

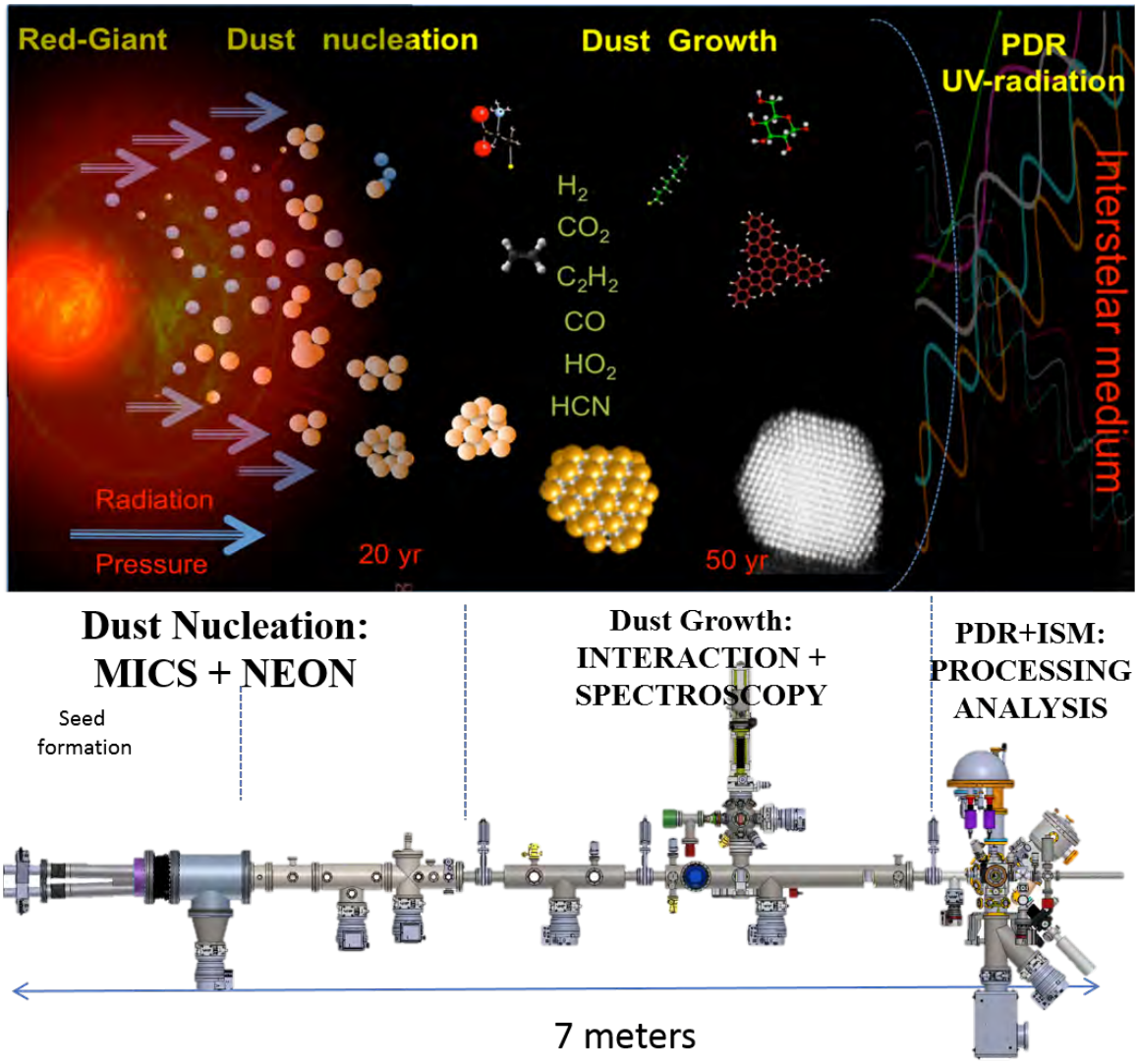

Figure 1.8 The Stardust machine in Madrid has been developed in the framework of the NANOCOSMOS project to mimic the formation of dust in evolved stars (Martínez et al. [2018]).

1.3.2 Objectives of this work

The AROMA analyzer combines laser and ion trap techniques to mass spectrometry in a high vacuum environment. Through its two laser steps ion source, this setup is particularly suited to detect PAHs in dust samples, including cosmic dust analogues

generated in a variety of reactors and also meteorites, which are of interest as a potential stardust source in the laboratory. A limitation though in the molecular analysis is that a peak in a mass spectrum can be attributed to a given chemical formula but not to a given structure. Still having information on the structure is crucial to get information on the chemical pathways involved in the growth of PAHs and associated particles as discussed in Sect. 1.2.1 and 1.2.4. The objective of this work is therefore to optimise the ability of AROMA to get further structural insights through collision induced dissociation (CID) experiments.

AROMA is not a commercial setup in which the CID procedure has already been implemented. Therefore part of this work has been to get better knowledge on the characteristics of the setup and investigate the CID conditions that are best suited for our scientific objectives. In parallel of implementing a procedure for isomer differentiation, we have investigated the possibility of extracting molecular data from our measurements, in particular dissociation rates that are crucial to determine the stability of PAHs in astrophysical environments (cf. Sect. 1.1.3). Finally, simulations of PAH ion dynamics and energetics were performed to guide the experimental procedure and support the analysis of the results.

Chapter II

Molecular Analyser : AROMA

Contents

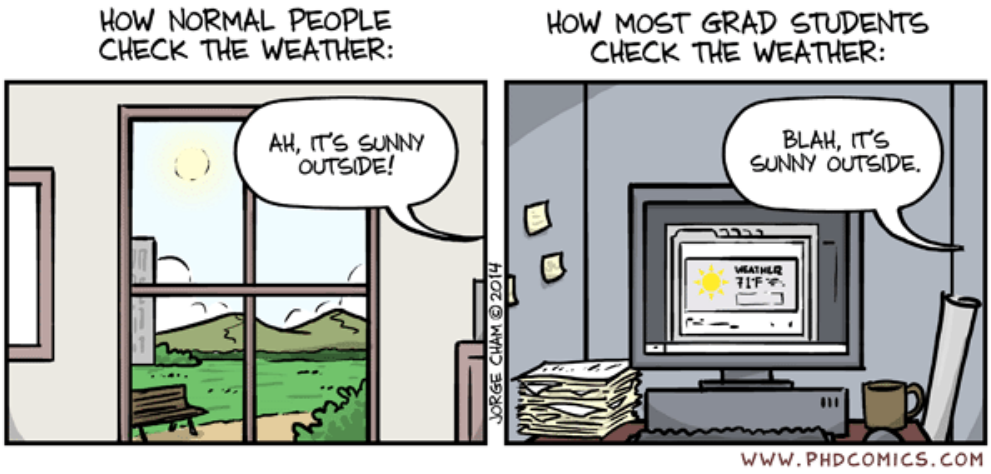

Figure 2.1 Working with AROMA

2.1 Overview

In this chapter, I describe the experimental apparatus used during my PhD. AROMA is a hybrid mass spectrometer consisting of a time-of-flight spectrometer combined with a quadrupolar ion trap. It is coupled to a laser desorption/ionization source. First, I introduce these various techniques and then focus on the specificity of AROMA and its functionalities including ion generation, ion trapping, collision induced dissociation (CID) and mass spectrometry analysis.

2.1.1 Mass spectrometry techniques

Mass spectrometry (MS) is a powerful analytical technique, which measures the mass to charge ratio (m/z). The value of z represents the charge number and the mass is defined in dalton (Da) or unified atomic mass unit (u) as 1/12 of the mass of the atom of ^{12}C in its lowest state.

The masses of the nucleons are 1.672649×10^{-27} kg for protons and 1.674930×10^{-27} kg for neutrons. This leads to the values listed in Table 3 which can be used to calculate the mass associated with a given chemical formula containing these elements. From table 3 we can see that an oxygen atom O has a mass of 15.995 whereas CH_4 as a mass of 16.021. Both are close to 16 with a negative mass defect for O and a positive mass defect for CH_4. They can be differentiated for a high enough mass resolution

(typically 1000). Approaching the exact mass is very important to differentiate species with close m/z in complex mixtures.

Name of Element	Symbol	Mass in u
Hydrogen	$^{1}_{1}$H	1.007
Helium	$^{4}_{2}$He	4
Carbon	$^{12}_{6}$C	12.000
Nitrogen	$^{14}_{7}$N	14.003
Oxygen	$^{16}_{8}$O	15.995
Argon	$^{40}_{18}$Ar	39.96

Table 3 Typical elements found in our studies and their masses in u.

Different types of instruments are used in MS (cf. Table 4) depending on the needed resolution, sensitivity, ion generation techniques, etc... We very briefly present these MS techniques below.

Analyzer type	Symbol	Principle of separation
Electric sector	E or ESA	Kinetic Energy
Magnetic sector	B	Momentum
Quadrupole	Q	m/z (trajectory stability)
Ion trap	IT	m/z (resonance frequency)
Time of flight	TOF	Velocity (Time)
Fourier transform ion cyclotron resonance	FTICR	m/z (resonance frequency)
Fourier transform orbitrap	FT-OT	m/z (resonance frequency)

Table 4 Types of mass analysers and their separation principle. Table adaptated from Hoffman and Stroobant [2007].

Sector mass spectrometry Magnetic sectors deflect ions according to their momentum. In this type of mass spectrometer, ions leaving the ion source are accelerated to a high velocity. The ions then pass through a magnetic sector in which the magnetic field is applied in a direction perpendicular to the direction of ion motion. Thus, ions are deflected to a circular motion of a unique radius, of curvature according to its m/z ratio, in a direction perpendicular to the applied magnetic field. In a similar way, electrostatic sector analyzers deflect ions based on their kinetic energy. The electric sector applies a force perpendicular to the direction of ion motion, and therefore has the form

of an arc. In single mode configuration (single magnetic sector), the mass resolution is limited by the fact that ions leaving the ion source do not all have exactly the same energy and therefore do not have exactly the same velocity. To reach high resolution an electric sector should be added to focus ions according to their kinetic energy. Conventional magnetic sector instruments are generally double - focusing systems, which means that they use a single electric sector and single magnetic sector.

Quadrupole mass analyzer It consists of four parallel metal rods, or electrodes. The ions are accelerated by a potential of 5-15 V and injected into the area between the 4 rods. An electrical quadrupole field is applied. Opposite electrodes have potentials of the same sign; one set with $(U + Vcos(\omega t))$ and the other with $-(U + Vcos(\omega t))$. U is a direct (DC) voltage and ω is the frequency of the alternating (AC) voltage of amplitude V. The applied voltages affect the trajectory of ions traveling down the flight path centered between the four rods. For given DC and AC voltages, only ions of a certain m/z ratio pass through the quadrupole filter and all other ions are thrown out of their original path. In this manner, the ions of interest are separated and could be monitored on the detector.

Ion trap mass analyzer The ion trap is a variation of the quadrupole mass filter, and consequently is sometimes refer to as a quadrupole ion trap. It consists of ring electrode and a pair of end-cap electrodes. The trap contains ions in a three-dimensional volume rather than along the center axis. Helium gas is added to the trap causing the ions to migrate toward the center. Radio- frequency voltage is applied and varied to the ring electrode. As radio-frequency voltage increases, heavier ions stabilize and lighter ions destabilized and then collide with the ring wall. After trapping, the ions are detected by placing them in unstable orbits, causing them to leave the trap to the detector.

Time of flight Time of flight (TOF)-MS is achieved by differentiating the ions through the time needed for an ion to go from one point to another. All the ions are prepared with a specific kinetic energy and thus their velocity depends on their m/z ratio. This technique used in AROMA is described in more details in Appendix A.2.

Fourier Transform Ion Cyclotron Resonance Fourier Transform Ion Cyclotron Resonance (FTICR)-MS consists in exciting the ions into their cyclotronic frequency in a fixed magnetic field. The ion current image is recorded as a function of time and a Fourier transform is performed on the signal to give a mass spectrum. With orbitrap this is the technique that provides the highest mass resolution.

FT orbitrap The general principle of an orbitrap is similar to the FTICR technique but without using a magnetic field. This is the newest MS technique that is only commercialized since 2005.

2.1.2 Quadrupolar Ion trap

2.1.2.1 Introduction to quadrupolar ion traps

Quadrupolar ion traps (QIT) are a powerful tool for mass-selective detection, storage, and excitation of the ion motion and they have been widely used since their development (Paul and Steinwedel [2014]; March [1997]; March and Todd [2005]; March [2009]). For mass analysis, they can be used as a stand-alone instrument or combined with other mass analyzers (section 2.1.1). The ions are "sensed" by their motion in the trap by superimposing a specific signal on the electrodes and observing its variation induced by charge motion in the trap. QIT can also be operated as mass filters before further study of the ions, the so-called MS/MS experiments. This functionality is also a common way to record the mass spectrum by selectively ejecting the ions depending on their mass and sending them to a detector. Key developments are summarized in Table 5.

QIT exist in two main configurations: linear form and three-dimensional form. Linear quadrupole ion traps (LQIT) are widely used in MS instruments for the trapping and cooling of atomic and molecular ions. Their advantages are their high injection efficiency and high storage capability. The total number of ions that can be stored in a three-dimensional ion trap is limited by space charge effects.

1953	First disclosure (Paul and Steinwedel [1953])	Mass-selective detection
1959	Storage of microparticules (Wuerker et al. [1959])	
1959	Use as a mass spectrometer(Fischer [1959])	
1962	Storage of ions for RF spectroscopy (Dehmelt and Major [1962])	
1968	Ejection of ions into an external detector (Dawson and Whetten [1970b, 1968]); use s a mass spectrometer (Dawson and Whetten [1970a])	Mass-selective storage
1972	Combination of QUISTOR with quadrupole mass filter for analysis of ejected ions (Bonner et al. [1972a]); Characterization of the trap, CI, ion/molecule kinetics, etc. (Bonner et al. [1972b])	
1976	Collisional focusing of ions (Bonner et al. [1976])	
1978	The selective ion reactor (Fulford and March [1978] Fulford and March)	
1979	Resonant ejection of ions (Armitage et al. [1979])	
1980	Use as a GC detector (Armitage [1979])	
1982	Multiphoton (IR) Dissociation of ions (Hughes et al. [1982])	
1984	Disclosure of the ion trap detector, (ITD)^{TM} (Stafford et al. [1984])	Mass-selective ejection
1985	Ion trap mass spectrometer ITMS^{TM} (Kelley et al. [1985])	
1987	MS/MS, CI, Photo-dissociation, injections of ions, mass-range extension, etc. Fourier transform quadrupole ion trap (Syka and Fies [1987])	
1984: 1988	Deliberate addition of contributions from non-linear field using stretched geometry and non-hyperbolic electrode surfaces (Syka [1995])	
1989	Extension of mass/charge range via resonant ejection (Kaiser et al. [1989])	
1990	High resolution mode of operation (Schwartz et al. [1991], Syka [1995])	
1995: 2001	Linear ion traps (Bier and Syka [1995], Syka [1995], Hager [2001])	
1997	Use of ion/molecule reactions in isotope ratio measurements (Barber et al. [1998])	
2002	Digital ion trap (Ding and Kumashiro [2001])	

Table 5 Milestones in the mass spectrometric development of quadrupole ion traps from March [2009] and March and Todd [2015].

2.1.2.2 About ion trapping

A quadrupolar ion trap has m/z operating stability regions which are defined by the Mathieu equations (See Appendix A.1) and can be represented in a [a_u, q_u] plane. Figure 2.2 shows in blue the stability region in the x direction of the trap and in red the stability region in the y direction. These areas overlap in purple corresponding to the couple [a_u, q_u] of values which enable the trapping of specific m/z species. We can then find the solutions for the specific case of our trap by tuning its operating conditions according to the following equations:

$$\begin{aligned} a_x &= \frac{4eU}{mr_0^2\omega^2} \\ q_x &= -\frac{2eV}{mr_0^2\omega^2} \end{aligned} \tag{1}$$

with U the DC voltage applied on the electrodes, V the AC amplitude, ω the RF pulsation and $2\,r_0$ the distance between opposite electrodes. From the symmetry in the geometry in the trap we find that $a_x = -a_y$ and $q_x = -q_y$.

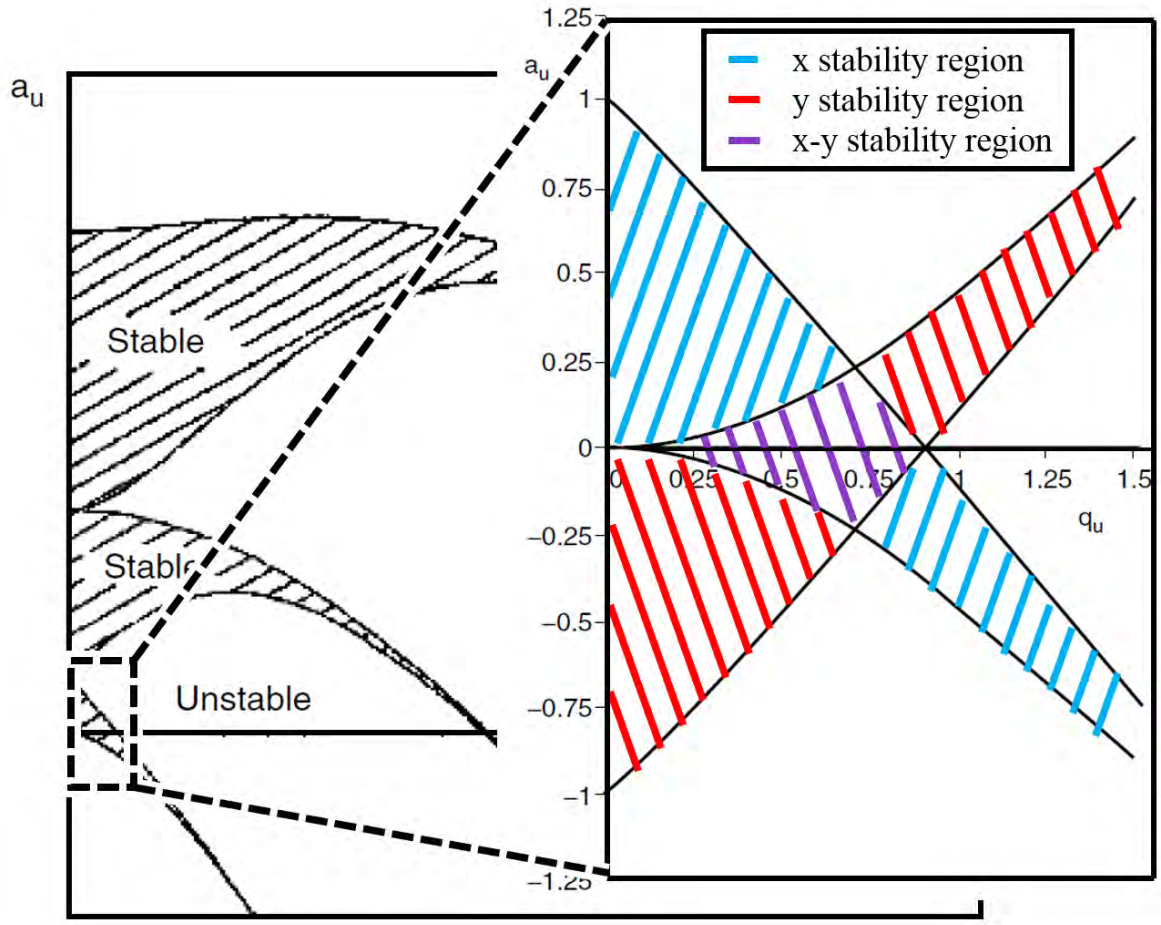

Figure 2.2 Representation of stable and unstable regions in the $[a_u, q_u]$ space. Adapted from March and Todd [2005].

2.1.3 Laser ion sources techniques

Laser light has interesting properties for the production of ions from different types of samples in MS analysis. These include pulsed operation, narrow range of wavelength and precise spatial impact distribution. Here we describe the essential steps of ion production achievable through laser light: laser desorption, laser ionisation and the resonance enhanced multi-photon ionization (REMPI) principle.

2.1.3.1 Principle of REMPI

The efficiency of the laser ionization determines the number of ions and is a key parameter for selective ion production. As can be seen in Figure 2.3, molecules can be ionized through different photo-processes depending on their ionization energy and electronic

structure. Vacuum ultraviolet single-photon ionization (SPI) has been proposed as a universal soft ionization method for organic compounds and has been applied to study asphaltenes as well as surfaces, materials, aerosols, drugs, and peptides. In AROMA, we use a REMPI scheme in which the first photon has to be resonant with intermediate electronic states of the molecule before the second photon is absorbed towards the ionization continuum.

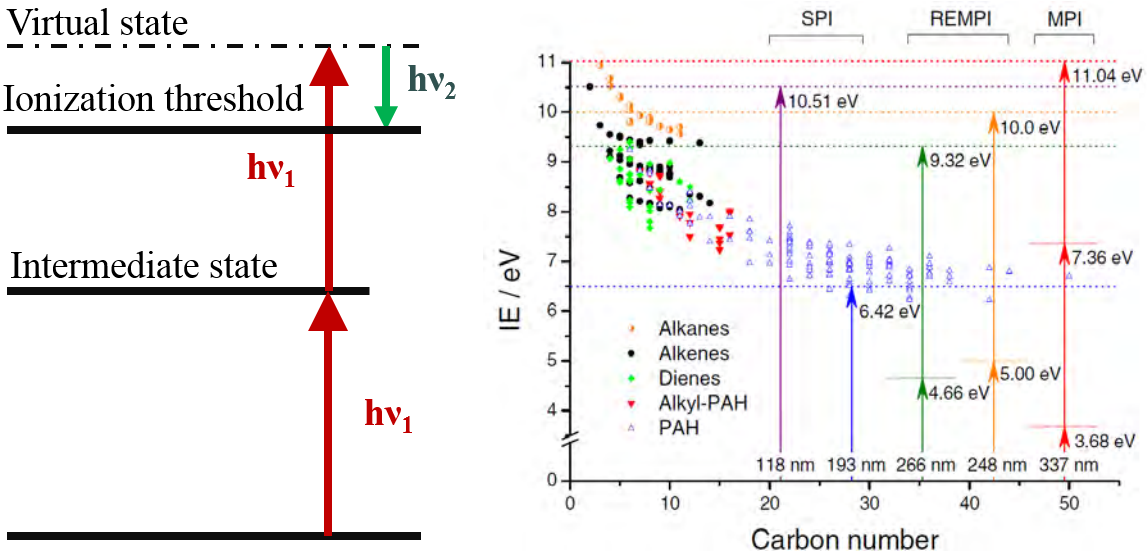

Figure 2.3 *Left*: [1+1] REMPI scheme used in AROMA. It involves the absorption of two photons from the same laser pulse and implies a resonant intermediate state and a virtual state higher in energy that the ionization threshold, *Right*: Ionization energies for different classes of molecules as a function of the number of carbons from Desgroux et al. [2013]. The blue triangles correspond to PAHs.

This technique has been chosen rather than electron impact ionization because it is less energetic and therefore leads to less fragmentation of the molecular population that is submitted to mass analysis.

2.1.3.2 Laser mass spectrometry

Laser mass spectrometry techniques with high sensitivity and microprobe spatial resolution were widely introduced to the analytical chemistry community in the 1970's (Dietze and Zahn [1972]; Moenke-Blankenburg [1972]; Hillenkamp et al. [1975]; Dietze et al. [1976]). These techniques were amongst the first capable of directly probing solid sample surfaces, an area that was at the time largely unexplored by mass spec-

trometry. This sparked an explosion of instruments coupling lasers to mass analyzers and led to the development of two powerful techniques during the 1980's and 1990's: matrix-assisted laser desorption/ionization mass spectrometry (MALDI-MS) (Karas et al. [1985]; Karas et al. [1987]; Karas et al. [1990]; Hillenkamp et al. [1991]) and laser desorption laser ionization mass spectrometry (L2MS) (Voumard et al. [1993]; Zenobi [1994]). These two techniques opened the door for investigations in the analysis of non-volatile species including large biomolecules and other organic species in native or artificial matrices. The ability to directly probe molecules in their native environments represented a significant advance in the utility of these techniques, largely eliminating the requirement for time-demanding extraction procedures.

LDI In MALDI-MS and its simpler cousin LDI-MS, desorption/ionization occurs during a single laser pulse. Despite the lack of clear understanding regarding the involved mechanisms, these techniques have proven to be a powerful tool for probing a wide variety of chemical systems. These include meteoritic samples (Hammond and Zare [2008]; Becker et al. [2001]), polydisperse polymers (Schriemer and Li [1996]; McEwen et al. [1997]), large biomolecules (Chaurand et al. [1999]; Jackson et al. [2005]) and fractions of petroleum (Acevedo et al. [2005], Herod et al. [2007]). However, obtaining an artifact-free signal from any of these samples requires a careful combination of optimized instrumental parameters and selection of the matrix. Without such considerations, the resulting spectra can be obscured by excessive fragmentation, plasma-phase reactions resulting in detectable ion clusters, or, worse, the absence of any signal at all.

L2MS In L2MS, desorption and ionization are separated in time and are realized by different lasers. The technique has been developed at Stanford University in the laboratory of Professor Richard N. Zare (Hahn et al. [1987]; Hahn et al. [1988]; Zenobi et al. [1989]) and applied to PAH analysis successfully by several groups (Kovalenko et al. [1992], Morrical et al. [1998]). It has been proven to be of high interest and capabilities in the study of organic compounds and characterization of aromatic species in extraterrestrial materials Engelke et al. [1987]; Hahn et al. [1987]; Kovalenko et al. [1992]; Spencer et al. [2008]; Faccinetto et al. [2008]; Sabbah et al. [2012].

The combination of focused laser-assisted thermal desorption and ultra-sensitive laser ionization provides sensitivity, selectivity, and spatial resolution capabilities that are unmatched by traditional methods of analyses. It has been shown that the detection limit is very low (down to the attomole (10^{-18}mole)) (Hahn et al. [1987]) thus the analysis only needs a very small quantity of the studied sample. As an example of such studies, PAH compounds were unexpectedly detected within the Almahata Sitta meteorites and their distribution within meteorite fragments provided important clues as to the identity and history of the asteroid parent body (Sabbah et al. [2010]).

2.2 The AROMA setup

AROMA "Astrochemistry Research of Organics with Molecular Analyzer" (Figure 2.4) is a unique molecular analyzer setup developed in the framework of the NANOCOSMOS project. AROMA main purpose is to analyze, with micro-scale resolution, the molecular content of cosmic dust analogues, including the stardust analogues that are produced in the NANOCOSMOS Stardust machine in Madrid (cf. Figure 1.8). It can also be used to analyze the content of other dust analogues created in plasma reactors and natural samples such as meteorites (see Section 4.3). The set-up has been constructed by the Greek company, Fasmatech, following design guidelines provided by the IRAP team. It is mainly composed of three parts, which achieve different steps in the performed experiments. These will be described later in further details. They consist in:

- a laser desorption/ionization source that offers the possibility of probing PAHs, carbon clusters and fullerenes in solid samples by performing either LDI in a single step or L2MS in two steps.
- A segmented LQIT (see Section 2.1.2.1) that allows trapping and isolating desired species and further performing CID experiments as well as photodissociation studies.
- An orthogonal TOF (oTOF) mass analyzer equipped with a two-stage reflectron and a fast microchannel plate (MCP) detector operating at a pressure of 10^{-7} mbar.

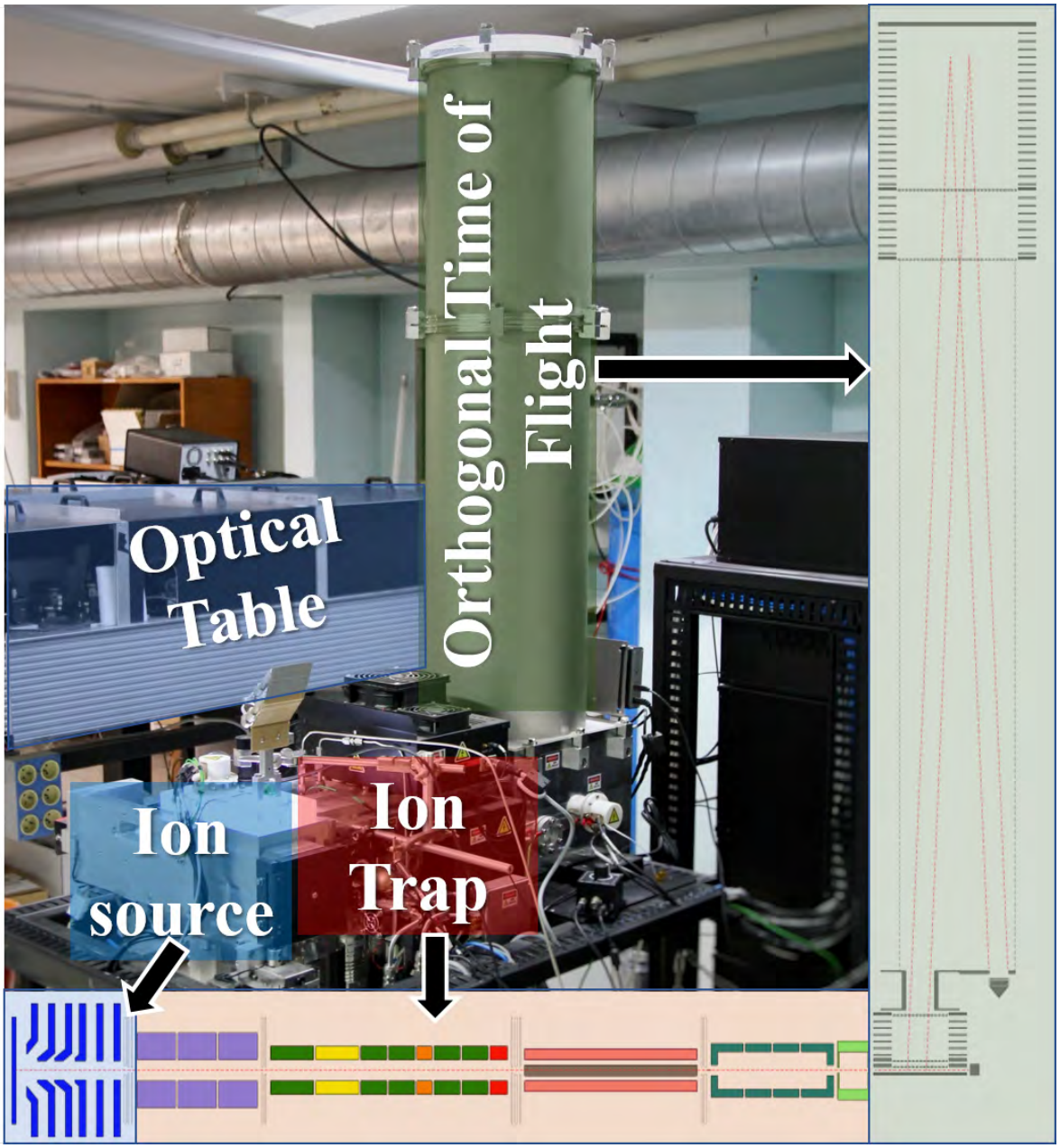

Figure 2.4 AROMA scheme and picture: ion source using laser beams coming from the optical table, ion trap in which the ions are stored, eventually processed by collisions or photons and sent to the orthogonal time of flight for detection.

2.2.1 Ion production

2.2.1.1 Description

Sample preparation We perform our experiments using a stainless steel sample holder. In Figure 2.5 we can see the plate with squares of different sizes and depths in order to be able to use different samples of different size and shapes with two rectangular

holes 3.5cm×3cm×1mm and 2.5cm×3cm×1.5mm as height×width×depth.

Figure 2.5 Stainless steel sample holder.

The sample is positioned vertically thus special care is needed to attach it on the sample holder. Three type of samples are analyzed with this configuration:

- Pure samples:

  Pure PAHs were dissolved to 1 mg/ mL solutions in toluene. From each solution, two to three 5 μL drops were successively spotted onto a 6 mm or 10 mm stainless steel sample disk. The disks are then fixed to the sample holder by a copper or carbon conductive tape. All samples were introduced into the system via a vacuum interlock, after allowing 1/2 h for the toluene to evaporate under ambient conditions.
- Meteorite samples:

  One to few milligrams of meteorite sample is powdered in order to be analyzed. It is crushed using a pestle. Then the powder is stuck on the stainless-steel plate (Figure 2.5) using copper conductive tape which does not contribute to the background signal.
- Cosmic dust analogues:

  Samples of cosmic dust analogues were delivered on a substrate. They can be put on our stainless-steel sample holders, respecting the size constraints, by sticking them with carbon conductive tape.

In order to introduce a new sample in AROMA, we open the load lock to insert the

stainless steel plate. Then the entry lock is closed, and pumped to achieve the same pressure (around 10^{-6} mbar) as the ion source. The entry lock is then opened on the side of the ion source and the stainless steel plate is positioned with the sample in front of the middle of the trap.

Laser technicalities Figure 2.6 shows the path of the laser beams on the optical table (see Figure 2.4). A polarizer/analyzer is positioned in the middle of the light path to control the intensity of the pulse. Then almost at the end of the path of the beams on the optical table, a 50/50 mirror is placed to redirect 50% of the flux to a detector which gives us the information on the power of the lasers. The actual energy arriving in the ion source has been measured to be >50% of the first measurement.

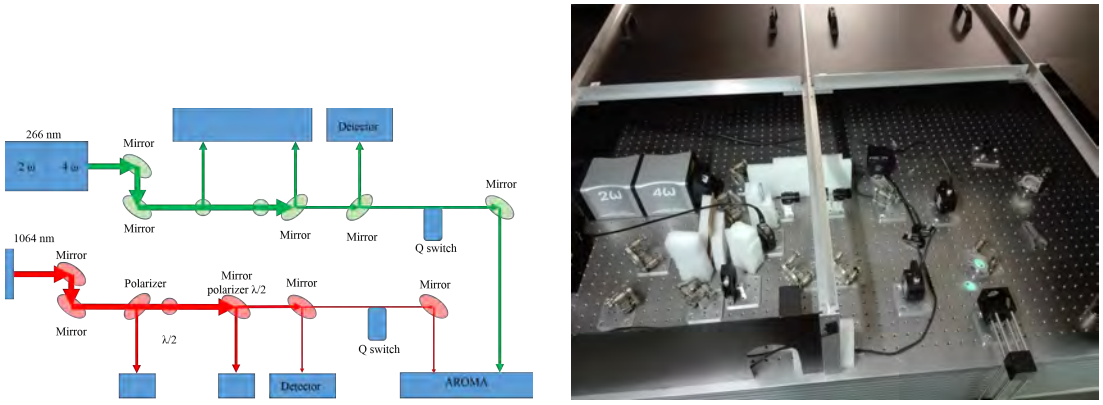

Figure 2.6 Laser scheme and picture of the optical table.

L2MS has been implemented in AROMA and this is the configuration I have used in my PhD work. As shown in Figure 2.7, it consists in desorbing, with a pulsed infrared laser beam, the solid material into the gaseous phase, with minimal fragmentation, and then crossing the desorption plume with an ultraviolet (UV) laser to selectively ionize the gas-phase aromatic organic molecules. Interestingly, the technique does not require any treatment to prepare the sample. In addition, the use of the UV laser for ionization allows us to detect PAHs with a very high sensitivity, down to tens of attomoles (Sabbah et al. [2017]). The IR and UV laser pulses are synchronized using a delay generator, with a precision in the range of 10^{-12} sec (picoseconds).

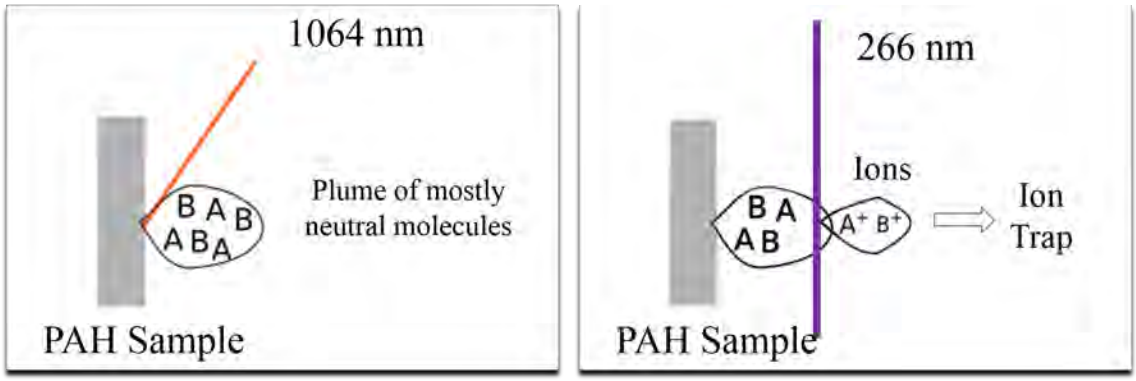

Figure 2.7 Desorption/ionization scheme in the ion source.

2.2.1.2 Performances

Desorbing laser The samples are positioned vertically in the ion source chamber at low pressure (10^{-6} mbar) and are observed by a microscopic camera. The laser desorption (LD) is achieved by irradiating the sample with the fundamental wavelength of a Nd:YAG IR (1064 nm) pulsed laser with pulse duration of 5 to 7 nanoseconds (Q-Smart450, Quantel). This leads to thermally exciting the molecules/atoms which will be detached from the surface leading to the formation of an expanding plume. The typical energies used in the experiments are 40-500 μJ/pulse on a 300 μm spot. It can be distinguished from ablation techniques due to its low photon fluence. As shown by Haglund Jr [1996], laser desorption can be distinguished from ablation by the fact that only the first mono-layers of the sample are affected. It corresponds therefore to a "soft ablation". It is achieved by tuning down the laser fluence. The interaction with the laser leads to a very fast heating process with rate of 10^8 K/s which can be opposed to other thermal desorption techniques with a 10-50 K/s (Deckert and George [1987]). This has also the advantage of favoring desorption over fragmentation for the molecules in the sample. The extraction of molecules from the surface happens indeed to be faster than the fragmentation of molecular bounds. The "soft ablation" produces an expanding plume of mostly neutral molecules and atoms. At the basis of the plume the density of molecules can be very large allowing three body reactions and modifying chemical composition of the desorbed molecules. Such a regime has not been observed in our experimental tests on pure PAH compounds. When performing LDI this laser is also the ionizing laser. This configuration is favorable to observe species such as small

carbon clusters using a similiar energy of $\sim 100\,\mu$J/pulse as the one used to desorb PAHs.

Ionizing laser The desorbed plume is intercepted perpendicularly by a second laser in the UV domain using the fourth harmonic output at 266 nm. The typical pulse energy used for this experiment is 3 to 5 mJ pulse^{-1}. The pulse duration is of 5 - 7 ns. The laser wavelength is made to selectively ionize aromatic species (see Figure 2.3). In practice, this gas-phase ionization creates a low-fraction of ions inside the plume, which is not commonly considered to be a plasma.

2.2.2 Time of flight mass spectrometry

2.2.2.1 Description

In the AROMA set-up, ions are mass-separated in a reflectron time of flight (TOF) using a modified Wiley- McLaren geometry (Wiley and McLaren [1955]). It is mounted in an orthogonal configuration as presented in Figure 2.8. Ions leaving the LQIT arrive in the acceleration zone and are orthogonally accelerated, using a high voltage pulse (-2000 V) of 80 μs duration, into the flight tube. A dual microchannel plate (MCP) set in a Chevron configuration, coupled with a large collector anode, is used as a detector. Orthogonal TOF (oTOF) decouples the conditions established in the laser desorption/ionization source with the initial conditions for TOF mass analysis, which results in enhanced mass resolving power over the entire mass range of interest.

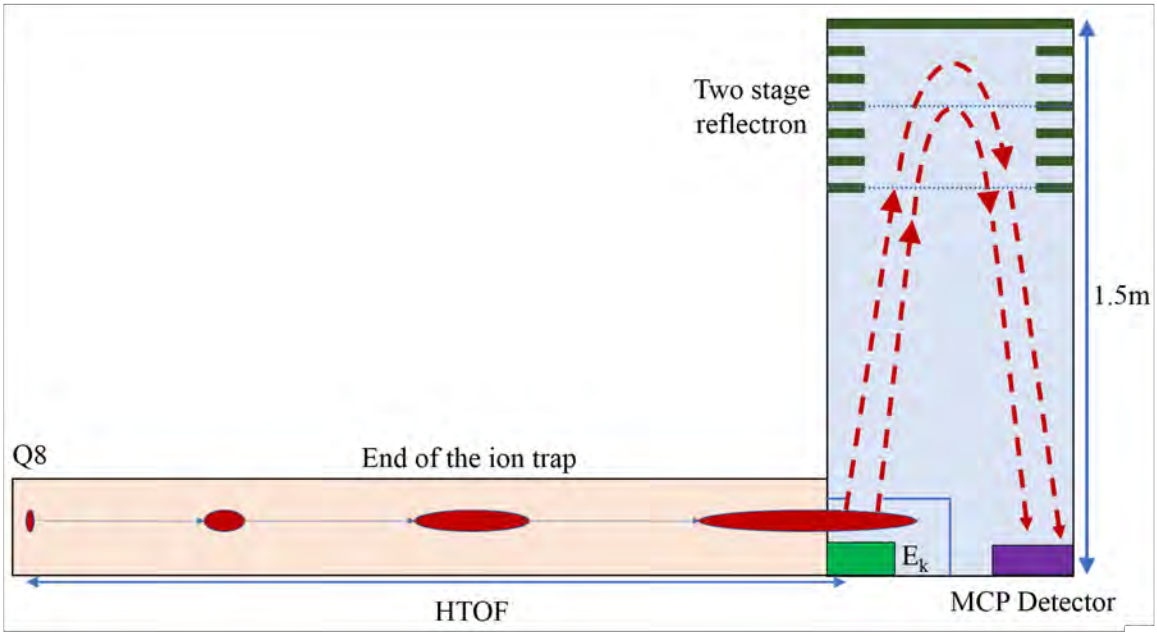

Figure 2.8 Scheme of the TOF in AROMA.

Since all the ions are not departing exactly from the same point, our TOF has a dual stage reflectron which enables the time focusing of the ions on the MCP receptors, thus increasing the resolution of the mass analyser. Indeed, it has been shown by experiments and calculations that a dual stage reflectron enables a second order (time and velocity) correction contrary to a single stage for which only the first order (time) correction is achieved (Doroshenko and Cotter [1999]). The high voltage in the first part of the reflectron drastically decreases the speed of the ions and the second one (from the bottom of the tube) timely focus them on the MCP detector.

The horizontal time of flight (HTOF) After their production, the ions are directed by a set of high-voltage lenses and focused through a small aperture into an octapole which aim is to collect, focus and kinetically cool the ion cloud to achieve the best possible ion transfer (Papanastasiou et al. [2008]). This is done by injecting a pulse of He gas. The ions are then transferred to the segmented LQIT for storing and processing. At the end of the LQIT (Q8 segment), the ions are sent with a kinetic energy kick of 45 eV through the hexapole and the ion focusing optics to the exciting electrode of the oTOF. This procedure is already a first time of flight that discriminate the ions as a function of their mass. We call horizontal time of flight (HTOF) the

delay between the departure of the ions from the Q8 segment to the application of the extraction voltage of the oTOF.

A first mass selection range is here performed by choosing a specific HTOF time. This time corresponds to a specific span of ions travelling at a certain speed enabling them to be sent in the oTOF in the next step. In order to achieve a fully representative spectrum of an experiment, we have to record different spectra while scanning the HTOF (Figure 2.9).

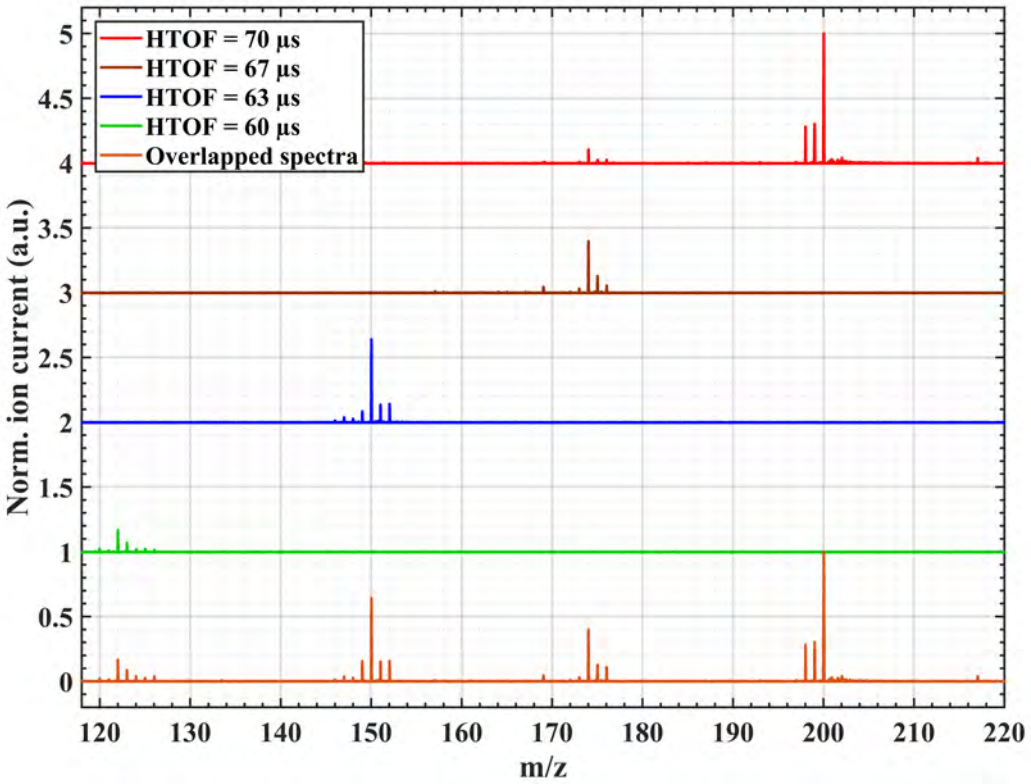

Figure 2.9 Example of 4 spectra obtained at different values of HTOF that are then overlapped to generate a complete mass spectrum.

2.2.2.2 Performances

In the following parts, we explain the procedure of the experiment starting here with some performances of the detection in AROMA. A very good mass resolution (m/Δm) of 8000-10000 at 200-300 m/z is achieved (see Figure 2.11), whereas common L2MS systems have a resolution of a few undreds to 1000 (Faccinetto et al. [2011]). Thanks to the combination of ion trap and oTOF we are not limited by the initial conditions (kinetic expansion of the ion cloud) of the ionization source. This high resolution is

combined to an extended mass range: from 20 to 10^4 m/z, and high mass accuracy up to 10 ppm. Thus we set the experimental procedure to access isolation at 1 m/z resolution, and to perform collision induced dissociation and photo-dissociation experiments in the future.

Figure 2.10 shows the L2MS spectrum obtained for pure pyrene, $C_{16}H_{10}$. In addition of the ^{13}C species, fragments are observed essentially corresponding to -H and -2H loss. The -H fragment is found to form efficiently a complex with H_2O.

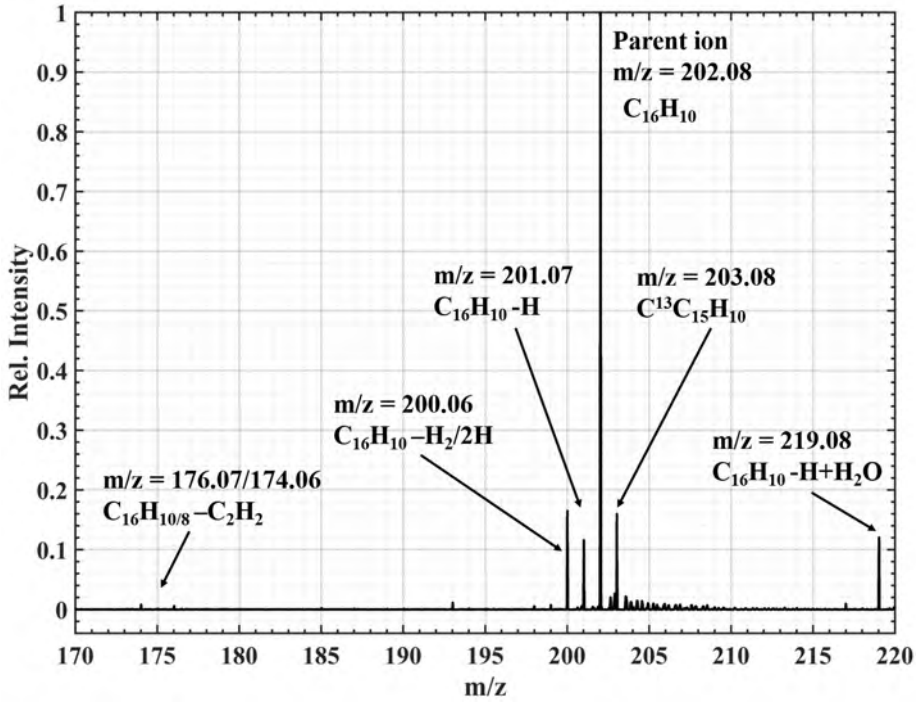

Figure 2.10 L2MS spectrum of a pyrene sample.

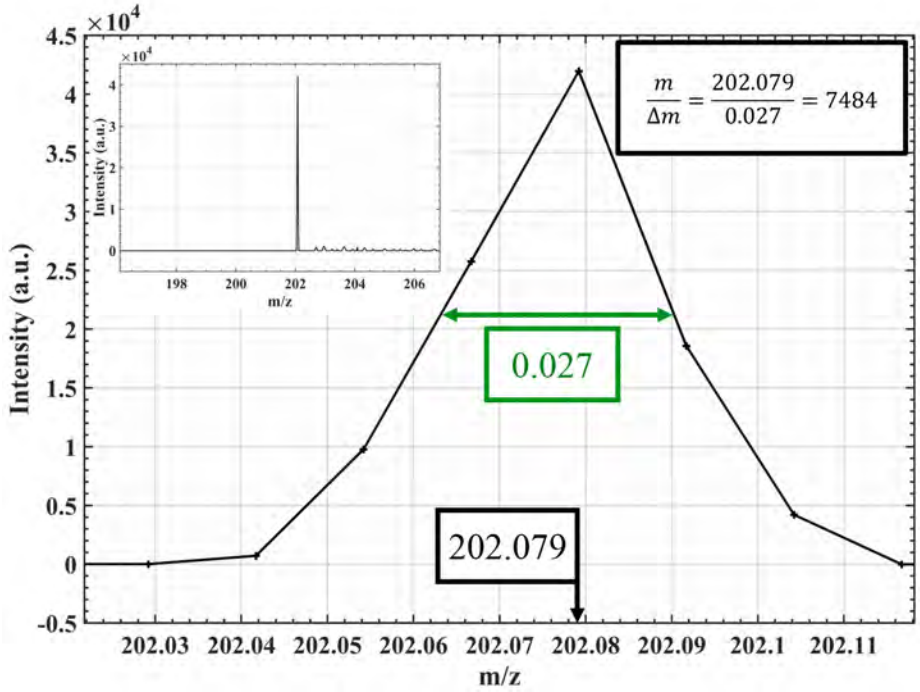

Figure 2.11 Experimental determination of the mass resolution in the AROMA set-up: example of a pure sample of pyrene.

As shown in Figure 2.11, we can easily achieve a resolution of > 7000. This resolution enables us to differentiate species such as C_{16} and $C_{15}H_{12}$, as shown in Figure 2.12 in the case of complexe samples here the Almahata Sitta meteorite.

When performing extensive experiments with pyrene ($C_{16}H_{10}$) we could using 10 μg on a gold disc of 1 cm, we could perform more than 10000 IR laser shots on the sample and still getting an intensity ≥ 5000 (accepting that a signal over 100 can be unambiguously be said not to be an artefact).

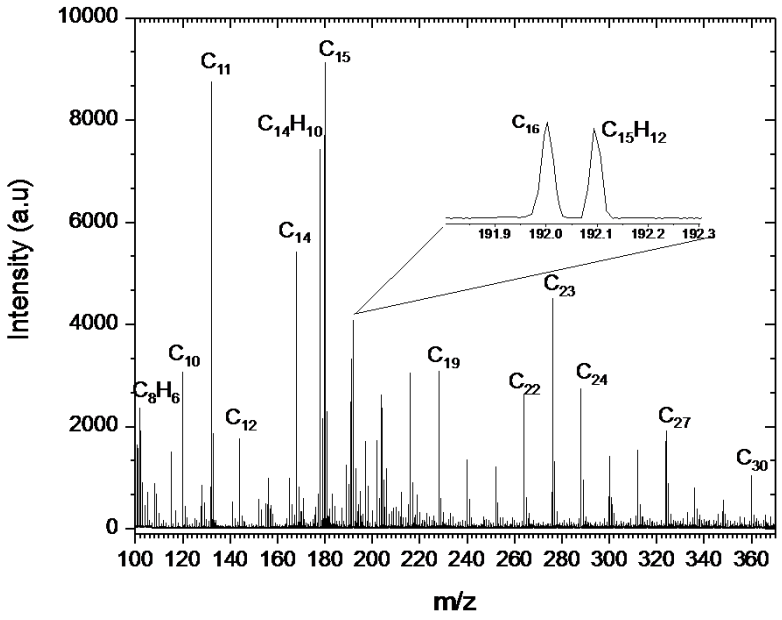

Figure 2.12 L2MS spectrum of a fragment of the Almahata Sitta meteorite from Sabbah et al. [2020].

2.2.3 Ion trap

2.2.3.1 Description

Combining an L2MS ion source to a Time of flight (TOF) has been done before: Hahn et al. [1987]; Hahn et al. [1988]; Zenobi et al. [1989]; Spencer et al. [2008]; Faccinetto et al. [2008]; Faccinetto et al. [2011]; Brédy et al. [2015]. In addition, AROMA comprises a trap (LQIT), which allows us to perform MS/MS experiments and therefore obtain information on ion structures.

Ion journey

Figure 2.13 describes the ion journey in the AROMA setup. After production in the ion source, the ions are directed towards the ion trap by an acceleration plate at 20-200 V. Then a set of high-voltage lenses slow and focus the ion cloud through a small aperture into the octapole as shown on panel a) of Figure 2.13. The purpose of the octapole is to collect, focus and kinetically cool with a buffer gas (Ar, He) the ion cloud. Ion transfer into the LQIT (panel b) of Figure 2.13) is therefore optimised.

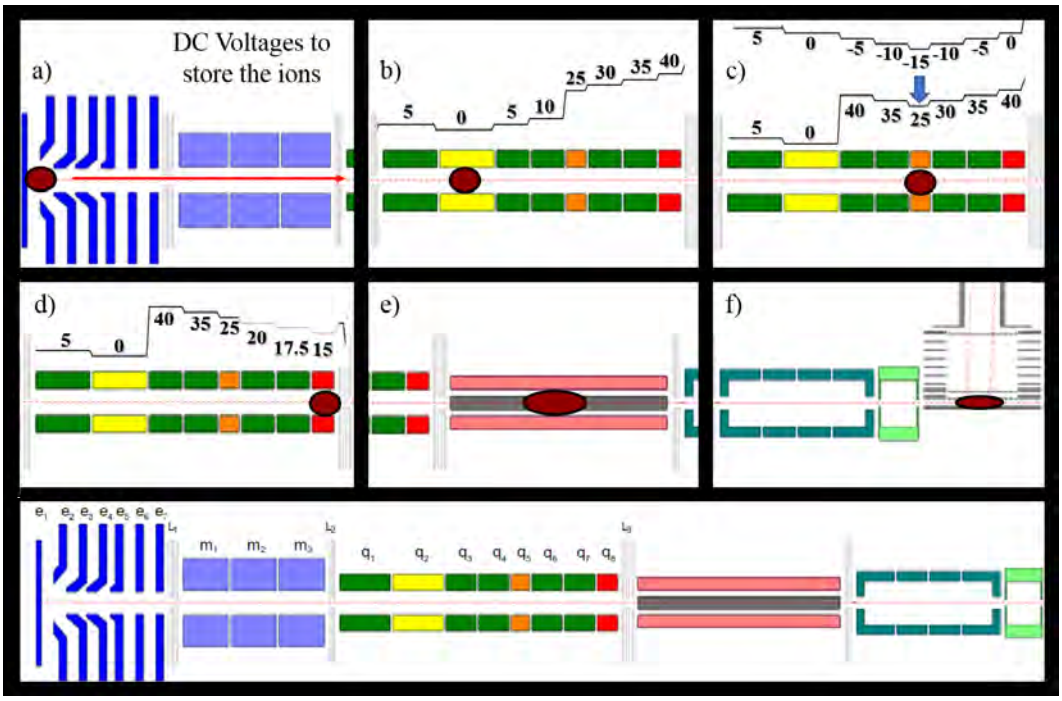

Figure 2.13 The journey of ions from the ion source to the extraction zone of the oTOF.

Linear quadrupole ion trap in AROMA

The LQIT (see scheme in Figure 2.14 and picture in Figure 2.15) is segmented into 8 parts from Q_1 to Q_8. Each DC potential applied on the segments can be tuned in order to control the global trajectory of the ions in the LQIT. The ions can be moved from a segment to another by changing the DC voltages. In standard experiments, the ions are stored in the second segment called Q2 by creating a little potential well (panel b) in Figure 2.13). A number of operations can be performed in Q2 such as CID as discussed below. For photo-dissociation experiments, the ions have to be sent to the Q5 segment (panel c) in Figure 2.13). After processing, the ions are then stored in the Q8 segment (panel d)) before being ejected with 25 eV through the RF hexapole ion guide (panel(e)) and on low voltage lens to focus the ions them oTOF (panel f)).

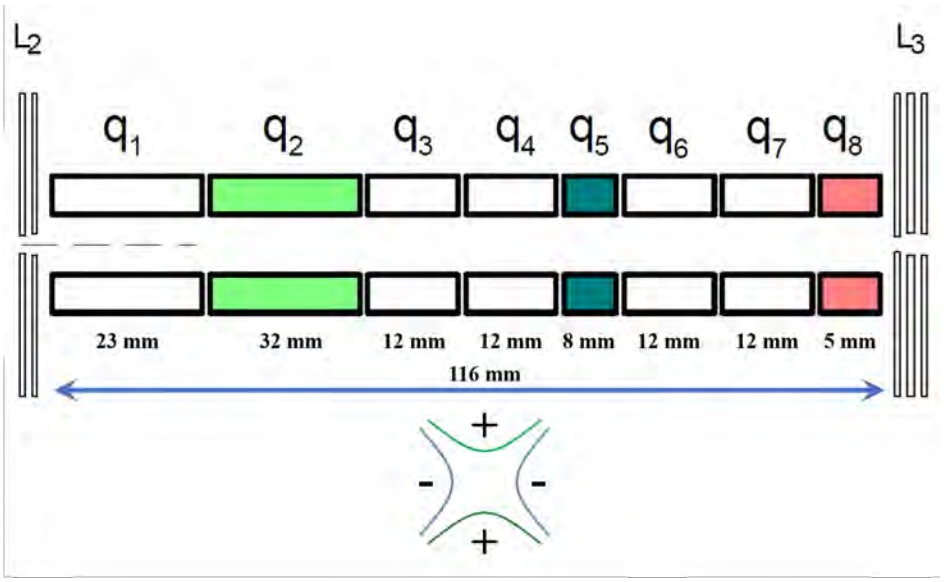

Figure 2.14 Schematic diagram of the LQIT with all its components.

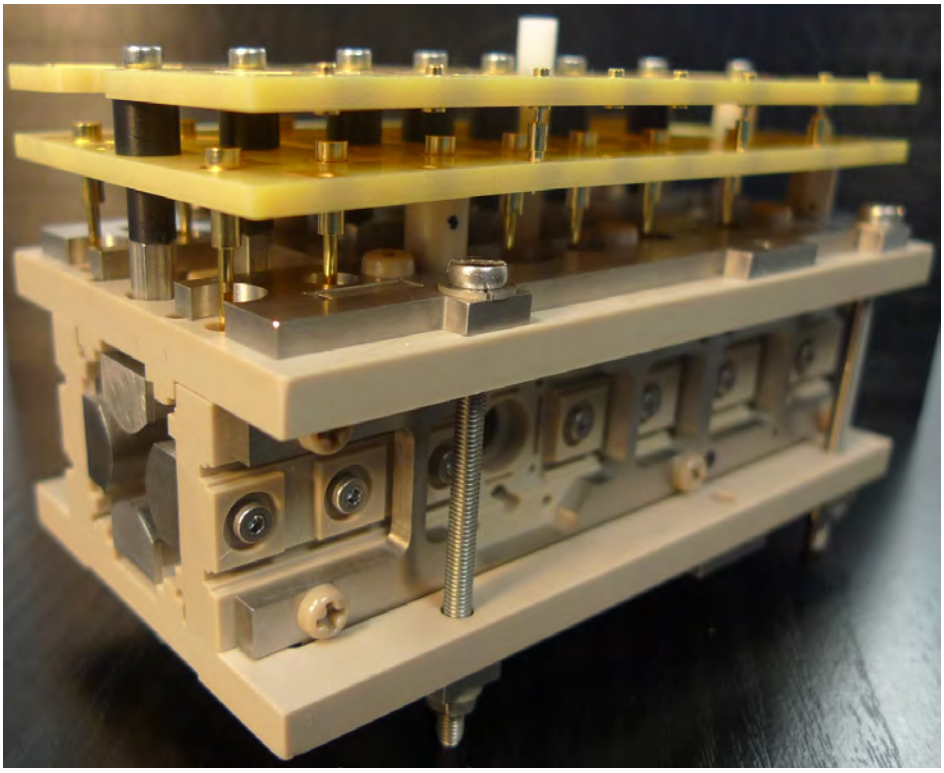

Figure 2.15 Picture of the LQIT present in the AROMA set-up.

2.2.3.2 Capabilities

Besides being able to store ions for times of the order of seconds the capabilities of the LQIT involve mainly three segments:

- In Q2, ions are stored, cooled and trapped. In this segment, isolation of a specific mass can be achieved using resolving DC technique or Filtered Noise Function (FNF) see 3.2.2. As we will show in the next Chapter, ion motion can be excited by applying dipolar excitation. Thus CID can be performed by pulsing gas in Q2 during this excitation.
- In Q5, there is the possibility to perform photo-dissociation studies on trapped ions.
- In Q8, ions are finally parked before sending them to the extraction region of the oTOF.

The rest of the segments are being used as potential walls to trap the ions or, on the opposite, as negative gradients to transfer them along the ion trap.

In Chapter III, I will further explain the different steps involved in AROMA experiments:

- internal and kinetic cooling of the ions through gas injection in the trap,
- isolation procedure leading to 1 m/z resolution isolation, which is important in dissociation studies,
- and, finally, the application of dipolar excitation in order to perform CID to achieve dissociation studies and isomer differentiation.

Chapter III

Collision induced dissociation procedure

Contents

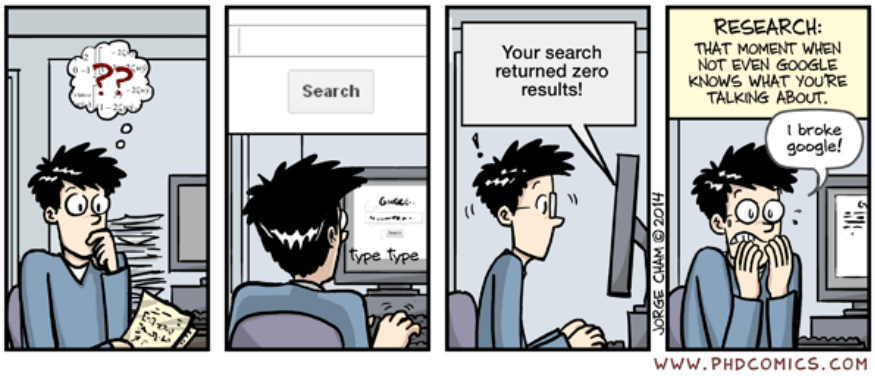

3.1 Collision Induced Dissociation

Collision Induced Dissociation (CID) corresponds to the process of fragmenting a molecule by getting some energy by one or several collisions with a background gas. The history of CID is closely related to the history of mass spectrometry as summarized in the next section. In the following, we focus on CID experiments performed on PAHs and present the procedure which has been implemented on the AROMA setup. In particular, we illustrate the effect of the dipolar excitation parameters (amplitude and duration) on the CID spectra.

3.1.1 History

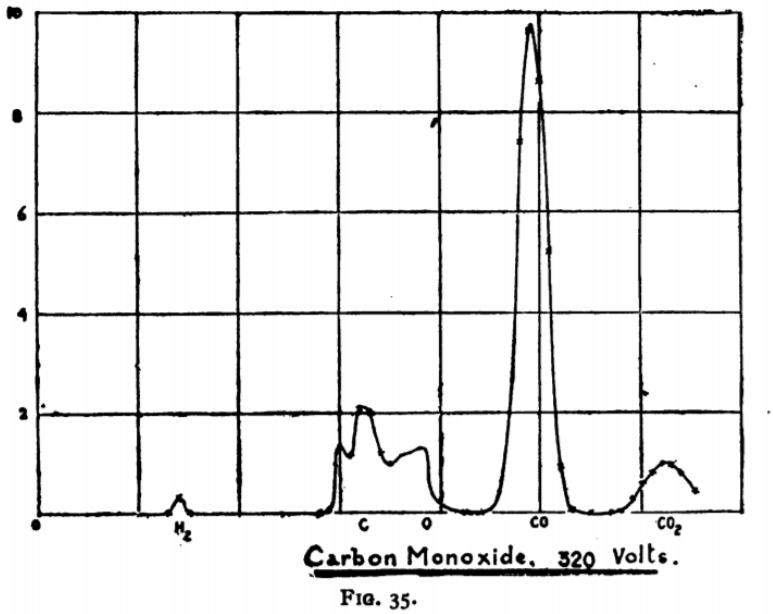

Figure 3.1 Mass spectrum of CO obtained in a sector mass spectrometer after CO dissociates in C, O and even produces CO_2 through recombination from Thomson [1914].

The first CID signal was observed by Thomson [1914] (see Figure 3.1) and by Aston [1919] to account for residual signals coming from Collision Activation (CA). Following this observation, two main directions appeared. The first aimed to reduce the effect of CA or to avoid it in order to get mass spectra dominated by the analyte parent ion. The second focused on how to use CA to obtain CID spectra and get insights into the fragmentation behavior of the studied species. After a few studies performed by Kolotyrkin et al. [1953], and Melton and Rosenstock [1957]) we have to wait until the work of McLafferty and Schuddemage [1969] and McLafferty et al. [1973b] to demonstrate the usefulness of fragmentation following CA in identifying isomeric structures. Thus the next studies focused on developing CID as a tool to differentiate isomers. Many of them were performed using keV CA (McLafferty and Schuddemage [1969], McLafferty et al. [1973b,a]). Other works led by J. Beynon and R. Cooks concentrated on describing the interaction of the ions with different gas from rare gas to H_2 or C_4H_{10} (Beynon et al. [1972], Cooks et al. [1975], Cooks [1973], Kim et al. [1974]). When the use of MS/MS (cf. Section 2.1.2) was recognized, Cooks and co-workers combined chemical ionization and sector mass spectrometers to analyse chemical mixtures (Kondrat and Cooks [1978], Busch et al. [1983]).

It is only in the late 1970s that commercial instruments using CA and MS/MS were built. All CID experiments were carried out using sector mass spectrometers with keV collision energies involving 1 to 10 collisions until the use of triple quadrupole for MS/MS as described by Yost and Enke [1978, 1979]. The use of the triple quadrupole allows access to collision energies of less than 100 eV in the center of mass (com) (Dawson and Douglas [1983], Douglas [1982], Dawson [1982, 1983]). New CA conditions were also found using a cyclotron resonance instrument (Cody and Freiser [1982]). Louris et al. [1987] used a quadrupole ion trap with a background pressure of 1 mTorr to perform CID (10^6 collisions at E_{com} = 15 eV as given in Equation 4). With increasing control of the ion motion within the quadrupolar ion trap or in FTICR setups, the collisional energy could get lower and lower as shown in Figure 3.2 from the model from Goeringer and McLuckey [1996]. The different conditions of CA in CID experiments have been reviewed by Mayer and Poon [2009].

The principle of CID can be described as follows:

- CA in which an ion P gets internally excited by the collision with a neutral target N by the transfer of a part of the kinetic energy to the internal energy of the ion.

$$P_{E_{int}^0}^{K_0\ +} + N^{K'} \rightarrow P_{E_{int}^1}^{K_1\ +} + N^{K''} \tag{2}$$

  where K is the kinetic energy and E_{int} the internal energy,
  with $K_0 > K_1$ and $E_{int}^0 < E_{int}^1$.
  Thus, after storing enough internal energy the molecule will have the possibility to relax by changing conformation or breaking one or more bonds. In our experiments, we are interested by the latter case which is referred to:

- the decomposition of the activated ion.

$$P_{E_{int}^n}^{K_n\ +} \rightarrow A_{E_{int}^A}^{K_A\ +} + B_{E_{int}^B}^{K_B} \tag{3}$$

Where E_{int}^n is the internal energy built after n collisions which can lead to fragmentation. In this process the parent ion gives birth to two fragments A and B which contain kinetic and internal energy (unless B is an atom).

MS instruments offer the possibility to optimize key parameters to get insight on the kinematics of the CA and CID process. However the mechanism of CA is difficult to quantify and models should be made to describe energy transfer during collisions. These rely on approximations that limit the use of CID for quantitative studies on the energetics of the ions.

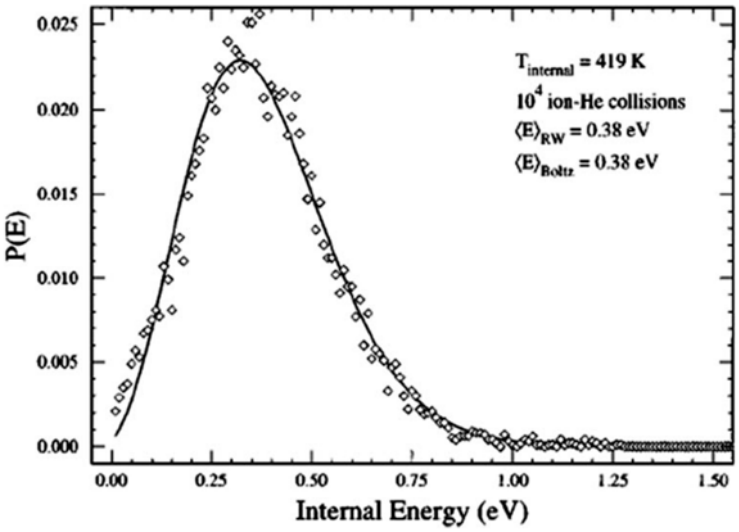

Figure 3.2 Results of random walk simulations involving 10000 collisions of n-butylbenzene ions with 150 mV resonant excitation within 10^{-3} Torr of He at 300K. The ion internal energy distribution based on the model derived by Goeringer and McLuckey [1996] corresponds to a Boltzmann distribution at a temperature of 419 K. From Goeringer and McLuckey [1996].

3.1.2 Collision Induced Dissociation of PAHs

A number of CA experiments have been carried out to differentiate PAH isomers, but some of them led to contradictory results. Shushan and Boyd [1980] demonstrated that it is possible to differentiate PAH isomers in sector instruments by using either the decomposition of metastable ions or CA at impact energies of 4 keV in He collision gas. With the latter technique, the authors concluded that it is possible to differentiate the two studied isomers at $m/z = 202.08$, namely pyrene and fluoranthene. On the opposite, Pachuta et al. [1988] studied the dissociation of several PAHs including fluoranthene and pyrene, using high-energy excitation (7, 8 keV) and concluded that it was fairly hard to differentiate isomers only relying on these experiments. They suggested that due to isomerization prior to dissociation nearly identical fragmentation patterns are experienced for different parent PAH isomers. The difference with the conclusions of Shushan and Boyd [1980] could be attributed to differences in ion production in both experiments. This has been shown to be a possible differentiation factor (Zenobi et al. [1989]). Arakawa et al. [2000] tried to use keV collision energies to achieve new ways to differentiate isomers such has pyrene and fluoranthene based on their dissociation pattern but did not succeed neither by varying the collisional gas (air, N_2 and Ar) nor

the kinetic energies (from 600 eV to 5 keV). It is only recently that Gatchell et al. [2014] and Stockett et al. [2014] evidenced another type of dissociation channel involving a single carbon loss as compared to the usual hydrogen and C_2H_2 loss. This channel was attributed to non statistical fragmentation and referred to as a knockout process (Stockett et al. [2015a]), which can be reached at high collisional energies (E_{com}=30-50 eV, ∼2 keV of collision energy for pyrene in He). Fragmentation involving knockout was applied on isomers (Stockett et al. [2015b]) and the authors concluded that they could differentiate isomers better than using statistical fragmentation.

Pyle et al. [1997] used CID at lower energies (∼100 eV collisions, E_{com} ∼16.5 eV for pyrene in Ar) showing the possibility to differentiate pyrene from fluoranthene by their number of "ortho-hydrogen" interactions (pairs of neighboring hydrogens on the same cycle), which are six and seven, respectively, and leads to fluoranthene losing more easily its hydrogens than pyrene. A similar conclusion was obtained for the two isomers chrysene and benz(a)anthracene. Nourse et al. [1992] studied the sequential fragmentation of pyrene cations using multistage CID dissociation in a quadrupolar ion trap. Guo et al. [1999] used a slow heating approach in a FTICR-MS to fragment PAH ions step by step using a multi-step MS/MS (MS^n) approach.

The possibility of using CID to quantify the energetics of PAHs has been investigated by the group of P. Mayer as an alternative to the photoelectron photoion coincidence (PEPICO) experiments carried out at the VUV synchrotron (West et al. [2018a]). Breakdown curves, which represent the evolution of the relative abundance of the parent and fragments, have been obtained as a function of the center-of-mass collision energy (E_{com}) similarly to the curves obtained as a function of the VUV photon energy. Using the Rice Ramsperger Kassel Marcus (RRKM) theory to model the dissociation, the authors could fit these breakdown curves and derive values for the activation energy and entropy of reaction/dissociation. The limitation though is that the conversion of E_{com} into internal energy of the ions presents some uncertainty leading to large error bars (West et al. [2014a,b, 2018a,b]).

3.2 CID procedure in AROMA

In AROMA experiments, the ions are kinetically excited inside a segment of the LQIT in which a pulse of rare gas is injected. From this point of view, this is similar to the experiments performed in FTICR-MS setups (Guo et al. [1999]). The pulsed injection of gas leads to some variation of the pressure during the experiment. In addition, as will be described in Chapter V, the ions in the trap are not in a uniform trajectory and their kinetic energy oscillates between zero and hundreds of eV upon dipolar excitation. Thus this leads to a wide distribution of collision energies whose range depends on the actual pressure in the trap. The CID conditions in AROMA imply then that the distributions of collision frequency and collision energy (in the laboratory frame) evolve as a function of time.

Performing CID experiments in the AROMA set-up consists in several steps:

- producing the ions in the ion source,
- transmitting them to the Q_2 segment of the LQIT. During this transfer and in Q2 the ions can be thermalized with collisions with the buffer gas.
- Isolating the species of interest (parents) and then performing CA by applying a dipolar excitation amplitude and injecting another pulse of rare gas (Ar or He).
- Performing mass analysis on the ions (remaining parents and fragments) by sending them to the TOF.

3.2.1 Cooling

After being formed in the ion source the ions are sent to the LQIT. The transit of the ions in the octapole (cf. Section 2.2.3.1) before reaching the LQIT is synchronized with a gas pulse, typically He or Ar, raising the pressure to $\sim 10^{-2}$ mbar during a 20 to 50 ms time window. The collisions with the gas will allow the cooling of the ions both in kinetic energy and in internal energy. This cooling step is important if some analysis on the energetics of ion fragmentation has to be performed.

Drahos and Vékey [2001] described the evolution of the ion energy in partially inelastic collisions. Without an additional source of excitation, the ions will lose their kinetic energy and then relax their internal energy to achieve thermalization at the gas

temperature.

At the beginning of the cooling, the kinetic energy of the background gas can be neglected and E_{com} can be expressed by:

$$E_{\mathrm{com}} = \frac{m_G}{m_{ion} + m_G} \times E_{\mathrm{kin}} \tag{4}$$

Where m_G and m_{ion} are the masses of the buffer gas and of the ions, respectively. At the end of the cooling, when the ion is slowed down (its laboratory frame kinetic energy is close to zero), one can write:

$$\langle E_{\mathrm{com}} \rangle = \langle E_{\mathrm{kin,G}} \rangle \tag{5}$$

$$\langle E_{\mathrm{kin,G}} \rangle = \frac{3}{2} \times k_{\mathrm{b}} \times T_{\mathrm{G}} \tag{6}$$

In this case a part of the internal energy of the molecule will be transferred to the whole system as kinetic energy. This leads to collisions with negative energy transfer called "super elastic collisions" in Drahos and Vékey [2001].

Thus in order to work on ion populations with more controlled energy distributions (kinetic and internal) we have to increase the pressure of gas and the interaction time at the beginning of the trapping in order to increase the number of collisions and reach the conditions of thermalization with the gas. From the simulations presented in Chapter V, we see that kinetic cooling under trapping conditions is achieved after less than 500 μs even at 10^{-3} mbar pressure of Ar. Using He as cooling gas, there is a factor 10 in cooling efficiency due to the difference in mass, which means that we need to increase the interaction time by a tenfold thus up to 5 ms.

The first step in the CID procedure was therefore to produce ions that were spatially focused, internally and kinetically cool.

In the control software of the AROMA set-up, the cooling is performed by three steps:

- Delay with the previous function to synchronize with the injection of the gas pulse
- Gas injection time whose value constrains the duration of opening of the gas valve.

Relative to Ar, the cooling power of He is lower but induces less fragmentation.

- A second delay determining the residual gas pressure before the next step. From simulations in Chapter V, this delay has to be over 10 ms to kinetically cool the ions with He (we decided to double the previous 5 ms to take in account the uncertainties on the value of the pressure). In order to achieve internal cooling we also need to add some time leading to an interaction time of 100 ms.

Cooling is performed not only after the production of ions but also after any manipulation of the ions in the trap that could lead to kinetic or internal excitation such as the isolation step (Sect. 3.2.2) and after CID.

3.2.2 Isolation

Ion isolation can be accomplished by applying to the electrodes of the Q2 segment one or several of the following excitations: a DC resolving voltage, one or several dipolar excitations (DE) or a filtered-noise-field (FNF, first described in Goeringer et al. [1994]). In the first technique, ions are put in the instability region of the ion trap as explained in Figure 3.3. Its ejection power makes it very suitable to eliminate undesired ions that are not in the close vicinity of the species of interest. However the large DC voltages that are commonly associated with this method increase the loss of ions.

Applying a DE excitation requires three parameters: the frequency which has to be chosen depending on the conditions of the ion trap and the m/z of interest, the amplitude [100 - 200 mV] and time [$\tilde{1}$0 ms] which tune the efficiency of the ejection of the ions.

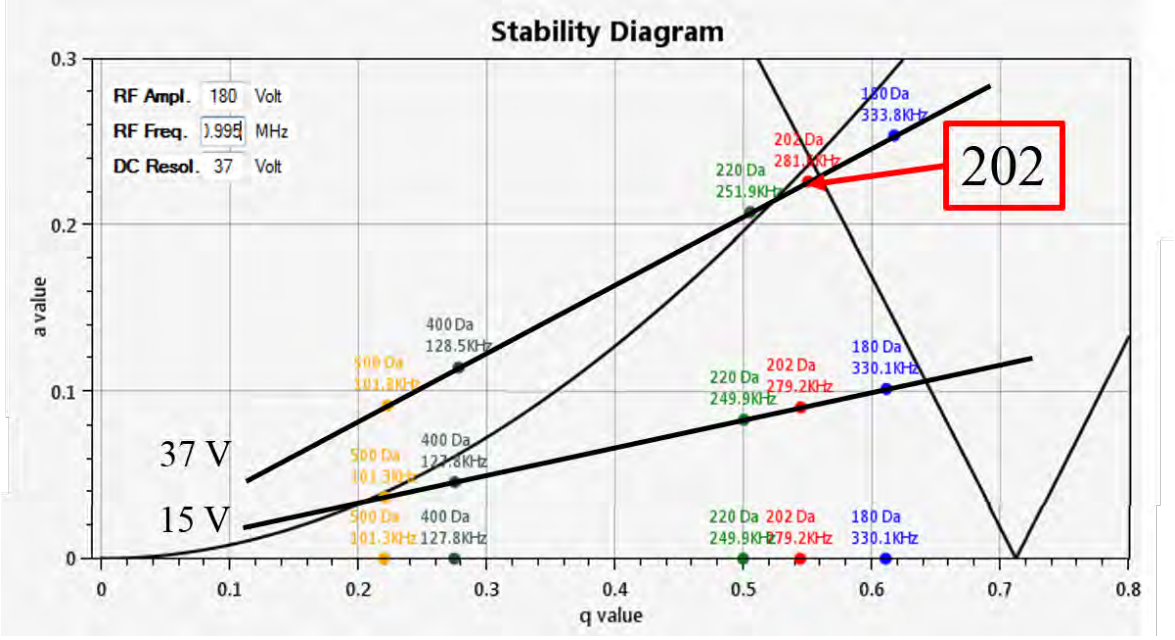

Figure 3.3 Representation of the [a, q] parameters depending on the masses with the stability regions (with dots of different colors: red = 202.08) before applying the DC resolving voltage and with DC at 15 V and 3 V. At 37 V m/z = 202.08 is the only one remaining in the stability diagram.

The FNF technique consists in generating a frequency comb which employs a single excitation waveform containing all the frequencies for a specific m/z excited range (like a comb of DE excitation). But before being converted into an analog signal, a rapid digital filtering method is applied to remove from the comb the frequencies corresponding to the m/z of interest. Thus the FNF will excite all the ions except the ones of interest. Still, FNF is more easy to apply on a large scale, whereas DE excitation isolation is easier to apply close to the m/z of interest. Combining these two techniques enables a fast, very efficient enhanced isolation procedure for any species of interest.

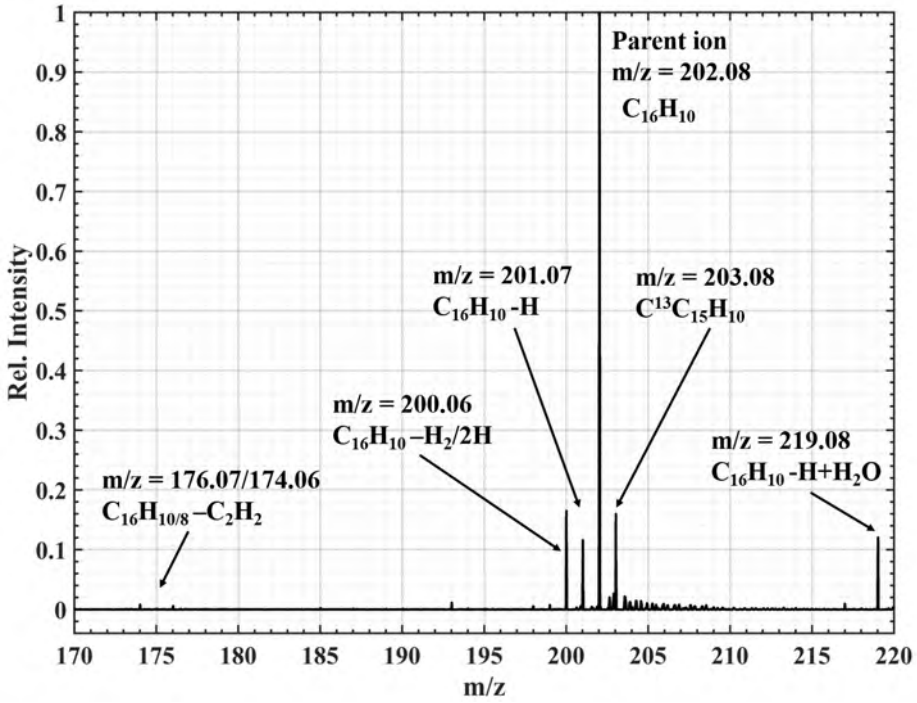

Figure 3.4 Pyrene mass spectrum in L2MS transmission mode.

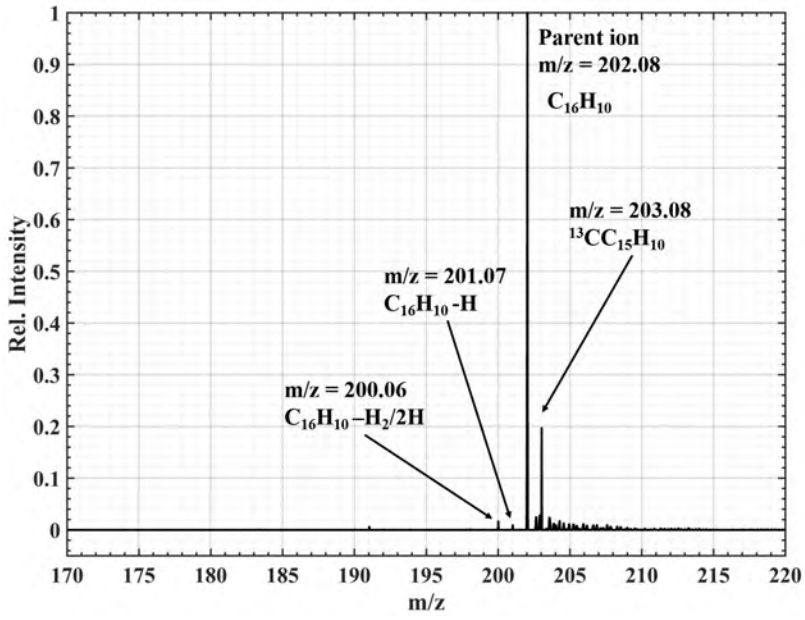

Figure 3.5 Example of DC resolving isolation (30 V in order to preserve as much m/z = 202.08 species) on a pure pyrene sample.

1 m/z resolved isolation of m/z=202.08 Figure 3.4 shows a typical spectrum of pyrene generated by L2MS and obtained in transmission mode (presented earlier in Figure 2.10 but shown here as a reminder). In order to isolate the parent ion and more

specifically the full ^{12}C isotopologue, we need to perform 1 m/z resolution at round m/z 202.08 for the isolation. We first apply the DC resolving voltage at 30 V (see Figure 3.5). The most stable species in the trap are the ones with m/z close (±1-2 m/z) to the species of interest. We then use a low amplitude (100 mV) in single DE excitation (on small ranges, even one m/z) or in FNF (on larger scales) and are able to selectively eject any m/z species even isotopomers (Figure 3.6).

More specifically in the case of m/z = 202.08 species :

- Resolving DC is applied to eliminate all the ions besides a small m/z range (200 to 204).
- A FNF/DE filter is then applied in the range from m/z = 198 to 206 which excludes excitation of m/z = 202.08.

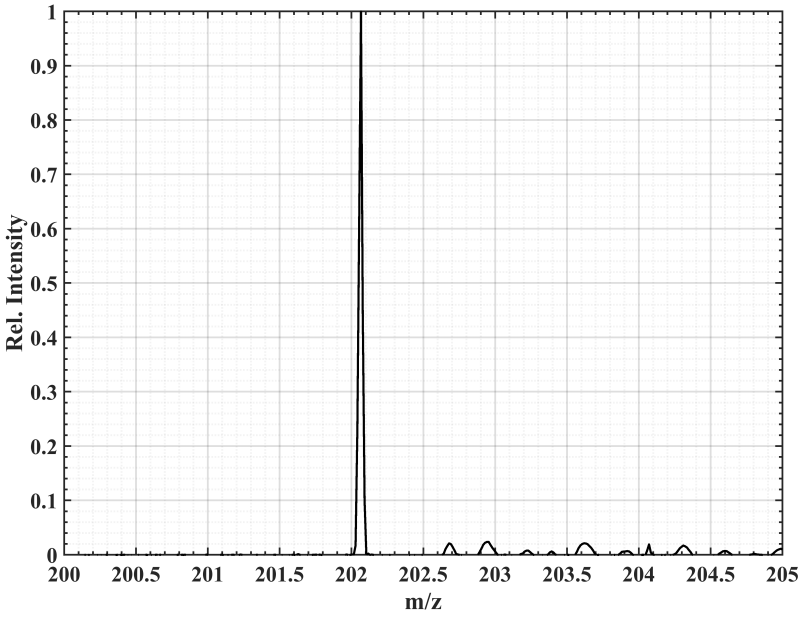

Figure 3.6 Typical spectrum with one m/z isolation of the peak at m/z = 202.08.

In Figure 3.6 we observe that a good isolation of the peak at m/z = 202.08 has been achieved. The small bumps at m/z = 202.6, 202.9, 203.6 etc... do not correspond to mass peaks but are due to the response of the MCP detector, more specifically to the ringing effect associated with a high ion intensity signal.

As a reminder it is desired to perform these steps with as less gas pressure as possible in order to avoid collisions and subsequently CA of the ions that could produce new species. Even if the ions of interest are not ejected or fragmented, there is however

no information on their kinetic and internal energy. Thus after these steps one has to remember to cool down the ions by injecting buffer gas and wait some time for the ions to kinetically and internally cool down.

3.2.3 Dipolar excitation

3.2.3.1 Principle

To perform CID in AROMA, the ions which are trapped in the RF field given by Equation 7 are kinetically excited by a DE called AC which is given by Equation 8 and is superimposed on two of the opposed electrodes (cf. Figure 3.7). Physically the DE will make the ions oscillate around their stable position with regard to the trapping conditions. From the technical data provided by Fasmatech with AROMA, we can assume that this process occurs in the presence of Ar gas at a pressure between 10^{-2} and 10^{-3} mbar. In the case of AROMA in order to improve the efficiency of the trapping it has been decided that the RF field is created using a squared waveform potential.

$$RF = U + V \cdot \sqcap(\omega_1 t + \phi_1) \tag{7}$$

$$AC = V_{op} \cdot \cos(\omega_2 t + \phi_2) \tag{8}$$

With

$$V_{op} = 0.8 \cdot V_{app} + 0.023 \tag{9}$$

$\sqcap(\omega_1 t + \phi_1)$ is the square function with 50% duty (half period -1 and half +1). This leads to $RF = U + V$ for half a period and $RF = U - V$ for the other half. Finally, V_{app} is the voltage applied on the electrodes from the User Interface and V_{op} the actual voltage on the electrodes.

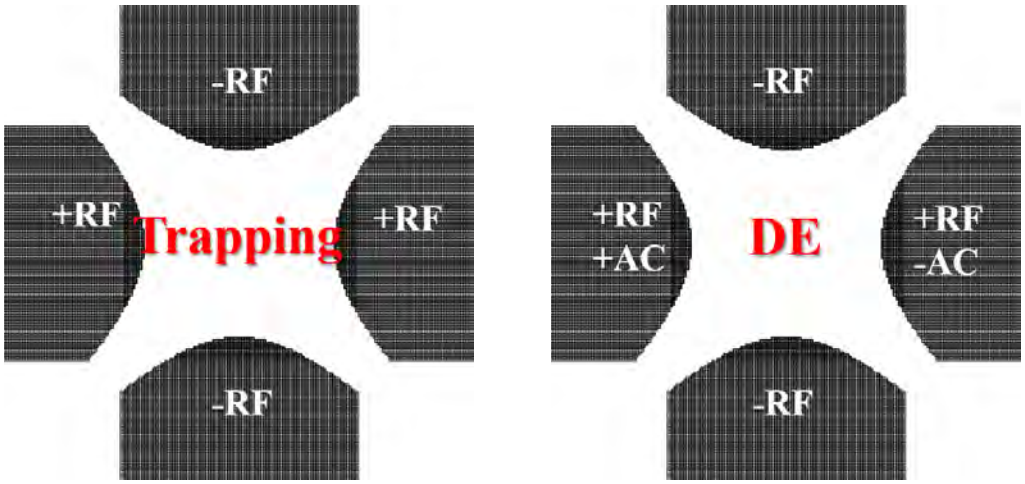

Figure 3.7 On the left, the trapping mode where a squared RF electrical field is applied to the electrode. On the right we see that a sinusoidal signal is superimposed on two of the electrodes to create the dipolar excitation (DE).

3.2.3.2 Secular frequency for m/z = 202.08

This is the resonant frequency at a given m/z. When applied through a DE it will induce the highest increase in kinetic energy. In the case of m/z = 202.08, the trapping conditions are a RF signal at 1.3 MHz with 180 V of amplitude. This leads to a secular frequency f_s of 205.6 kHz, as calculated with the following equations from Ding et al. [2004]:

$$a_u = \frac{4eU}{mr_0^2\Omega^2} \text{ with U} = 0 \Rightarrow a_u = 0 \quad (10)$$

$$q_u = -\frac{2eV}{mr_0^2\Omega^2} \Rightarrow q_u = 0.3481 \quad (11)$$

$$\beta_u = \frac{1}{\pi}\arccos\left[\cos\left(\pi\sqrt{\frac{q_u^2}{2}}\right)\cosh\left(\pi\sqrt{\frac{q_u^2}{2}}\right)\right] = 0.3290 \quad (12)$$

$$\omega_s = \frac{1}{4\pi}\beta_u \times \Omega \quad (13)$$

$$f_s = \frac{1}{2}\beta_u \times \Omega = 205.6\,\text{kHz} \quad (14)$$

with $\omega[\text{rad.s}^{-1}] = 2 \times \pi \times f[\text{s}^{-1}]$.

3.2.3.3 The excitation window

Ideally, one would like to control the excitation frequency in order to excite selectively the parent ions and avoid exciting the fragments once produced. As an example in Figure 3.8 we show the effect of the excitation amplitude and frequency on the ion excitation efficiency. This figure shows that the excitation efficiency is very important and has a large span for excitation amplitudes over 200 mV. At low voltage (here 100 mV) the DE only efficiently accelerates the m/z = 202.08 but, as we increase the voltage (200 mV), the same DE frequency will also efficiently excite molecules with m/z = 202.08 ± 1.

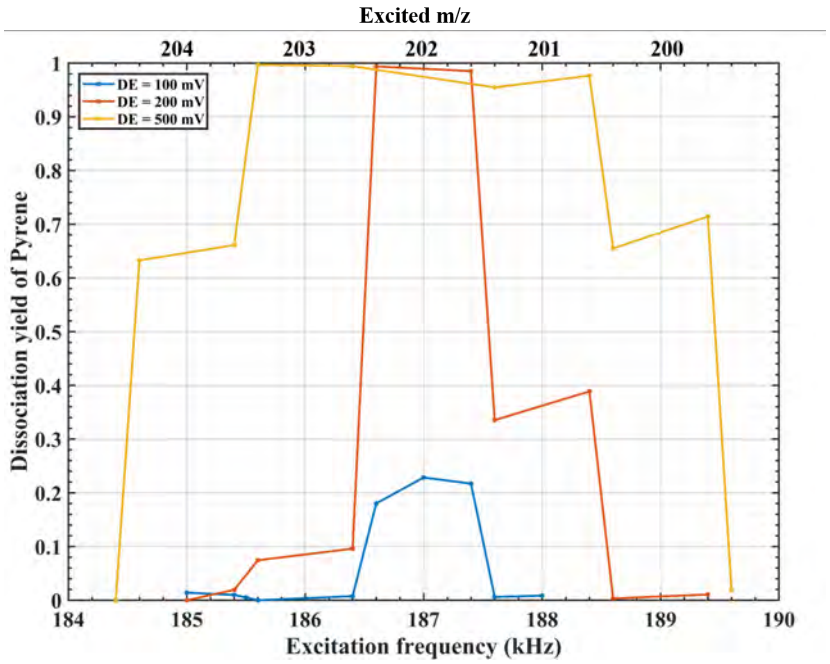

Figure 3.8 Effect of the frequency and amplitude of the DE excitation on the dissociation yield of the pyrene parent ions. We observe a widening of the excitation band with the increase of the DE amplitude. Plateaus are observed showing the experimental resolution of the DE in AROMA of 1 kHz.

With the Figure 3.8 we understand that an excitation off resonance can have the same effect on the dissociation yield as an on resonance excitation at low amplitude. For example, an excitation at 187 kHz (on resonance) with 100 mV leads to a 20% dissociation yield whereas an excitation at 188 kHz with 200 mV leads to a 40% dissociation yield.

This result has implication for both the CID and the isolation procedure. In the isolation procedure, it shows that, for a amplitude larger than 150 mV, the DE excita-

tion will definitively affect the other m/z close to the ejected ions. By increasing the DE amplitude we can therefore eject a larger range of m/z. On Figure 3.8, we have also observed a resolution of 1 kHz in frequency which happened to be centered on an integer. This peculiarity has been discussed with the Fasmatech company and has been attributed to the interaction between the squared form of the driving RF potential and the sinusoidal form of the DE.

In terms of CID it shows that, over 150 mV, the ions at m/z = 201.07 (first fragment) can also be excited and thus be subjected to fragmentation. This has to be considered in the case of fine experiments in which dissociation pathways, energetics and branching ratios are studied.

3.2.4 Global CID procedure

The capabilities of AROMA lie in the multiple collision regime consisting of hundreds of collisions of very low collisional energy < 1 eV and the capability to achieve different regimes. All the functions and parameters used in CID experiments are presented in Table 6. The mass spectra are recorded by the accumulation of 50 or 100 spectra.

Function	Subfunction	Experimental parameters
Ion source	IR laser	100-150 μJ
	UV laser	5-7 mJ
Trapping	Trapping frequency	1300 kHz
	Trapping amplitude	180 V
Kinetic and internal energy cooling	He gas pulse duration	110 μs
	Interaction time	100 ms
Low resolution isolation	DC resolving trap frequency	1150 kHz
	DC resolving voltage	32 V
	Interaction time	1 ms
Low mass filter	Trap frequency	865 kHz
	Interaction time	1 ms
Kinetic and internal energy cooling	He gas pulse duration	90 μs
	Interaction Time	50 ms
(1)DE filter	Frequencies	[172-186] [188-190] kHz
	Excitation time	5-10 ms
	Amplitudes	150-500 mV
OR		
(2)FNF	Frequency comb	[170-190] kHz
	Frequency gaps	[186.5-187.5] kHz
	Repetitions	15
	Amplitude	150 mV
Kinetic and internal energy cooling		
DE CID	Gas pulse duration	110 μs
	Delay (synchro gas/DE)	2.5 ms
	Excitation frequency	f_0
	Excitation time	**[0-100] ms**
	Excitation amplitude	**[0-3000]** mV
Kinetic and internal energy cooling		
Detection		

Table 6 Time function of the different steps involved in a CID experiment. When presenting the results we will specify the DE Excitation CID part.

3.3 CID results in AROMA

Here we present some CID experiments which have been performed in AROMA for the pyrene cation $C_{16}H_{10}^{+}$ for potential isomeric differentiation (see Chapter IV) as well as dissociation studies (see Chapter V).

Peak normalisation In the presentation of the CID results, we use two types of intensities:

$$\begin{aligned} Int_{rel}^{m/z} &= \frac{Int^{m/z}}{Int^{allm/z}} \\ Int_{rel,norm}^{m/z} &= \frac{Int_{rel}^{m/z}}{max(Int_{rel}^{m/z})} \end{aligned} \tag{15}$$

With :

- $Int_{rel}^{m/z}$ being the relative intensity of the considered m/z species,
- $Int^{m/z}$ its absolute intensity
- $Int^{allm/z}$ the sum of all the absolute intensities
- $max(Int_{rel}^{m/z})$ being the normalization factor corresponding to the highest relative intensity.
- $Int_{rel,norm}^{m/z}$ represents the normalized intensities, which can be considered as the survival yield (SY) in the case of the parent ions.

As an example, we refer to Figure 3.12, which presents a typical series of CID spectra in relative intensities on the left and the corresponding extracted SY and normalized intensities of the fragments on the right. The latter are also called breakdown curves.

3.3.1 Results

In order to take the best benefit of the capabilities of our setup in controlling the excitation window (the mass range of ions which will be efficiently excited) we performed various conditions of on resonance CID. In this type of experiments, one m/z resolution isolation has been performed and the secular frequency needed to excite the targeted ions has to be found with the highest possible precision ($\pm\,1$ kHz).

Dipolar Excitation amplitude = [0-100 mV] In Figure 3.9, with low excitation amplitude and long excitation time (50 ms), DE is in principle limited to the parent ions and this leads to the loss of m/z = 202.08 to produce m/z = 201.07 and 200.06. We can achieve 100% fragmentation of the parent ions to produce 80% of m/z = 201.07 and 20% of m/z = 200.06.

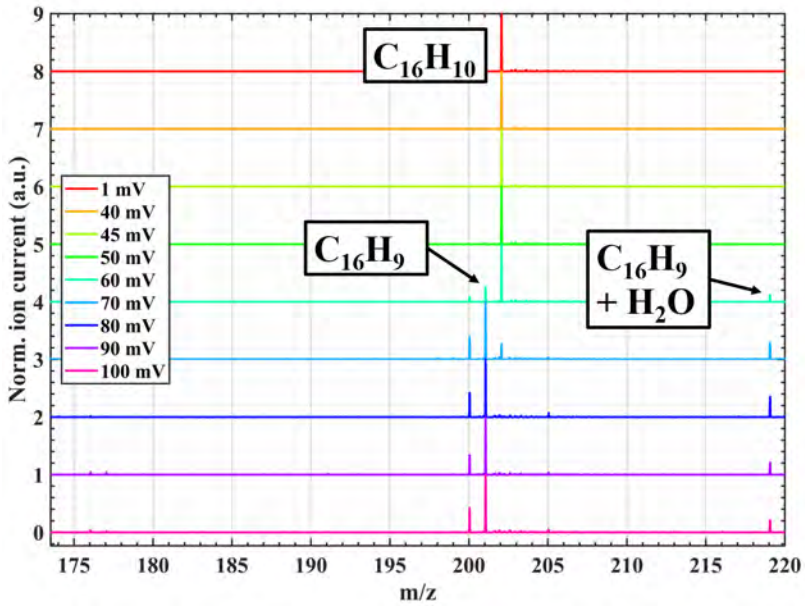

Figure 3.9 On resonance CID experiments applied on pyrene cations for 50 ms and with DE at 187 kHz±1 for amplitudes from 1 mV (upper curve) to 100 mV (lower curve).

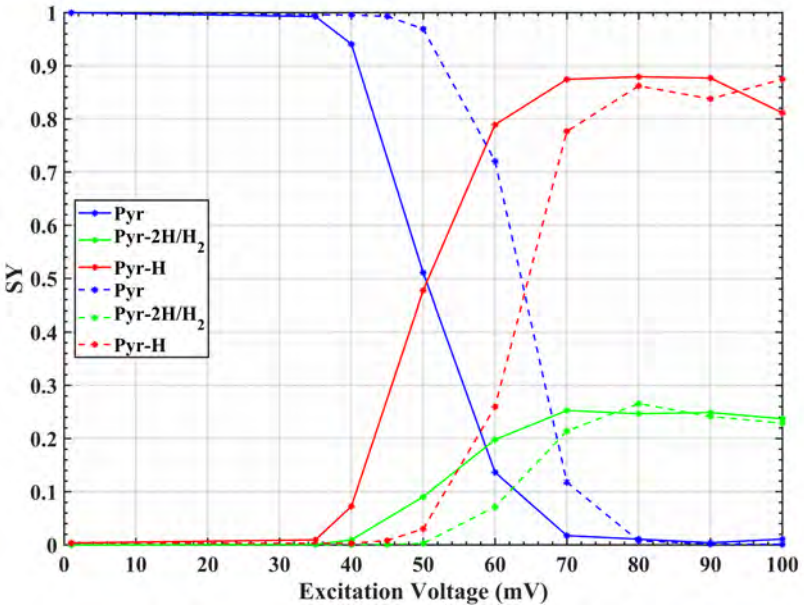

Figure 3.10 Two examples of on resonance CID experiments at low excitation amplitudes between 1 and 100 mV and for an excitation time of 50 ms. The first experiment is shown in solid lines and the second in dashed lines.

For amplitudes under 100 mV we have to use relatively long excitation time between 50 ms and 100 ms to perform dissociation of the full population. During these experiments, the parent ions (m/z = 202.08) accumulate internal energy via successive collisions at low energy leading to the possibility to depict the dissociation threshold. These low excitation conditions imply that the fragments are not significantly excited by the DE. This disables subsequent dissociation which could come from residual internal energy after the first dissociation.

Function	Subfunction	experimental parameters
DE Excitation CID	Background Gas pulse duration (Ar)	110 μs
	Delay	2.5 ms
	Frequencies	187 kHz
	Excitation Time	100 ms
	amplitudes	[0-100] mV
Translational and Internal cooling		

Table 7 DE Excitation function in the case of very slow heating CID experiments.

Table 7 reports the CID experimental conditions used to achieve this type of exper-

iments. An example is presented in Figure 3.10, in which we plot the SY of the parent ions (m/z = 202.08) and the production of the fragments (-H, -H_2/2H)). The two set of experiments have been recorded in the same conditions (excitation time = 50 ms, on resonance with excitation frequency EF = 187 kHz). The conditions for the first set (plain lines in Figure 3.10) have been optimized to loose just one or two hydrogen atoms (or an H_2 molecule). The setup was then shut down and restarted before performing the second set of experiments (dashed lines in Figure 3.10).

The onset of dissociation is around 40 mV for the first experiment and around 50 mV for the second one. This error of around 25% is found to be too high to accurately define a dissociation threshold for a specific structure. From the analysis of the data presented in Figure 3.10 we concluded that at this low excitation amplitude, it will be difficult to differentiate isomers with precision. The observed variation in the measurements could be explained by the fact that the driving amplitude of the trap is at 180 Volts and we superimpose an excitation amplitude of less than 100 mV. These low values of excitation are of the same order as the uncertainty of the power generator. Thus we decided to perform CID experiments with higher excitation amplitude (200 mV) to get farther from the limit of our instrument.

Dipolar Excitation amplitude = 200 mV At 200 mV, the excitation window is larger and we are exciting the species at m/z = 201.07. However most of the resulting fragments are in the range of HTOF window corresponding to the parent ions. Thus it is a promising method for isomer discrimination or compound identification. Table 8 reports the CID experimental conditions used to achieve this type of experiments. Figure 3.12 presents the SY recorded for pyrene as a function of the excitation time. We observe that we end breaking the parent ions (m/z = 202.08) into both m/z = 201.07 and 200.06, with a prevalence of the latter. The 50% SY of pyrene ions is reached after 1000 μs of excitation.

Function	Subfunction	experimental parameters
DE Excitation CID	Background Gas pulse duration	110 μs
	Delay	2.5 ms
	Frequencies	187 kHz
	Excitation Time	[0-2000] μs
	amplitudes	200 mV
Translational and Internal cooling		

Table 8 Dipolar Excitation experimental function description when performing slow heating CID experiments.

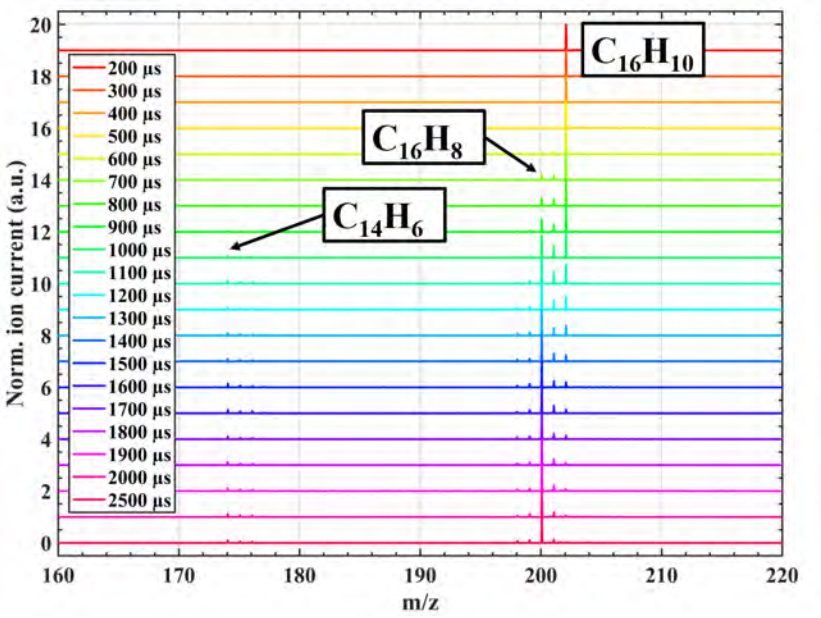

Figure 3.11 CID spectra of pyrene cations as a function of the excitation time for on-resonance DE and an excitation amplitude of 200 mV.

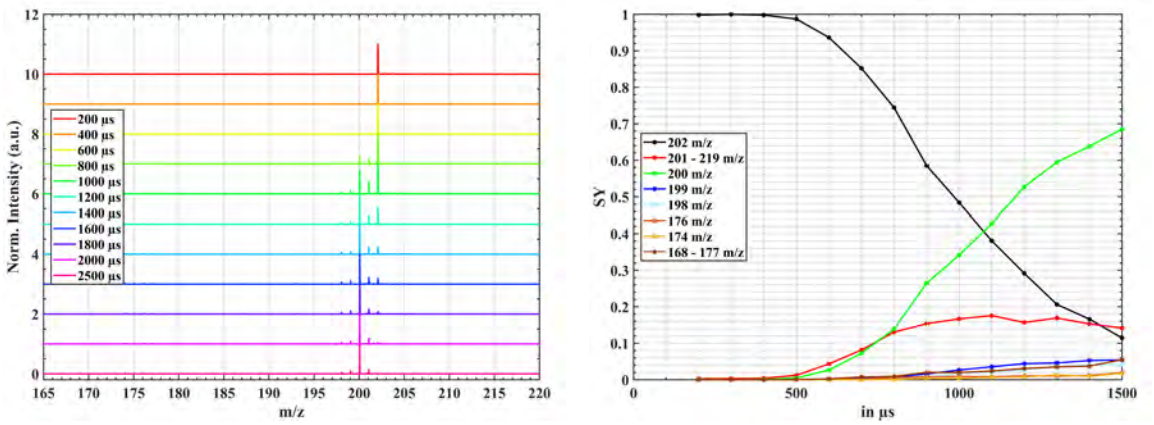

Figure 3.12 **On the left**: Spectrum of a set of CID experiments performed on resonance (187 kHz) at 200 mV on pyrene cations as a function of time. **On the right**: The extracted survival yield achieved using Equation 15.

One objective of these experiments was to optimize the conditions of excitation of the ions of interest to probe the fragmentation "thresholds". In Figure 3.11 we see that for a DE of 200 mV, the main fragment is $C_{16}H_8^+$ at m/z = 200.06 after 1.3 ms. This can be explained by the re-excitation of the m/z = 201.07 species (see Figure 3.8), which is effective at 200 mV, combined with the fact that the activation energy of m/z = 201.07 is significantly smaller than that of m/z = 202.08 (E_0 = 3.3±1.1 eV compared to 5.4±1.2 eV; West et al. [2014b]). Further comparison of the CID results obtained at 200 mV will be performed in Chapter IV.

Dipolar Excitation amplitude above 500 mV On the opposite, I also explored CID at high dipolar excitation amplitudes and short excitation time (50-100 μs) as can be seen in Figures 3.13 and 3.14. However, I noticed that the total ion signal drastically dropped as shown in these figures . This drop in ion signal is in accordance with what was shown in Nourse et al. [1992], Pachuta et al. [1988].

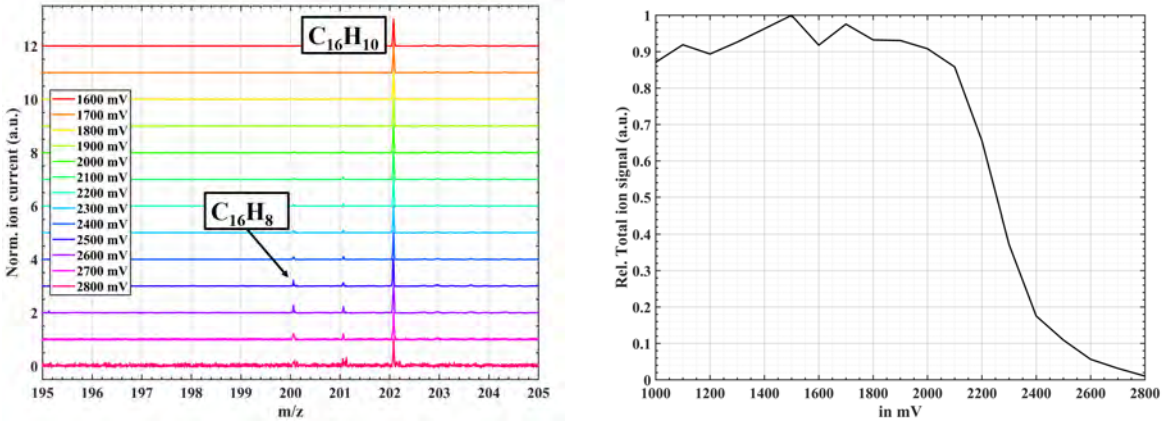

Figure 3.13 CID spectra of pyrene cations in Ar obtained with on resonance DE for 50 μs. The evolution of the total ion signal is shown on the right.

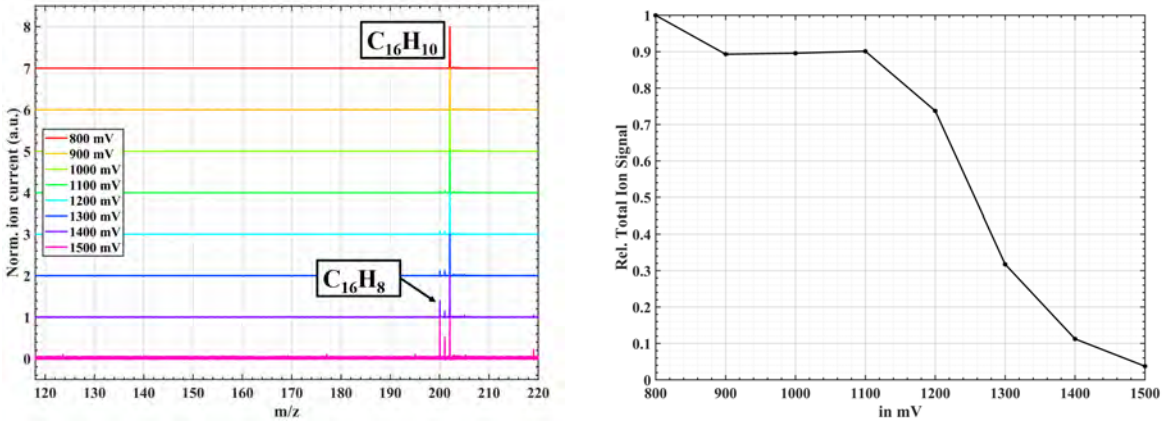

Figure 3.14 CID spectra of pyrene cations in Ar obtained with on resonance DE for 100 μs. The evolution of the total ion signal is shown on the right.

In Figure 3.15 we present a CID experiment breakdown curve achieved at a DE excitation of 500 mV. The amplitude has been chosen to minimise the loss of ions during the CID process. Compared to Figure 3.12, one can see clearly here the loss of m/z=200.06 into more dehydrogenated fragments.

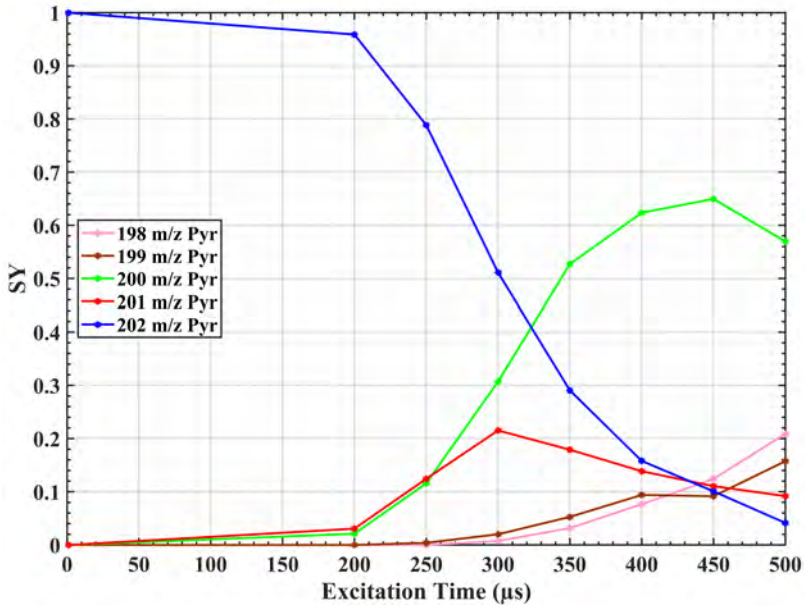

Figure 3.15 Example of decay curve of pyrene achieved at DE amplitude of 500 mV as a function of time.

3.3.2 Compilation of other techniques

In our experiment we could observe most of the fragments observed in Shushan and Boyd [1980], Pachuta et al. [1988], Nourse et al. [1992], Pyle et al. [1997], Guo et al. [1999]) and also in photodissociation experiments (West et al. [2014b]).

In Shushan and Boyd [1980] the ions are ionized by electron impact and sent on helium to provoke CID with 4 keV kinetic energy before being detected. The spectrum before CID already shows fragmentation with significant differences between isomers. The full population is then dissociated. Although there are differences between the isomers, it is hard to disentangle the contribution from dissociative ionization from that of CID. leading to differences in isomers which is hard not to link to the difference from the ionization. Using different techniques such as CID, electron-impact, surface collision and photodissociation, Pachuta et al. [1988] found the same fragments and fragments groups as our study and could observe differences in the dissociation pattern depending on the technique used and the collision energy, as was shown also by Pyle et al. [1997] and Nourse et al. [1992]. To retrieve the fragmentation pathways for these fragments, some studies have been done in Nourse et al. [1992], and Guo et al. [1999] using CID in MS^n experiments. In addition, West et al. [2014b] studied the dissoci-

ation cascade by combining photodissociation with selective ejection of intermediate fragments.

We indeed found a lot of similarities with the study by West et al. [2014b] in which the authors reported 34 fragments compared to 29 in our experiments, most of them being common in both experiments. A main difference between our CID experiments and photodissociation experiments is that, in our CID process, only the ions whose secular frequency is included in the excitation window of the DE excitation are accelerated and thus gain internal energy, whereas in photodissociation all the trapped ions can absorb the radiation and thus be excited to the point of dissociation.

In our CID experiments, we firstly form m/z = 201.07. With increasing amplitude, more m/z = 200.06 is observed similarly. A similar trend is observed in photoelectron photoion coincidence (PEPICO) experiments when increasing the energy of the VUV photon and is attributed to a sequential H+H loss [West et al., 2014b]. In our CID experiment, the m/z = 200.06 is expected to be formed from the dissociation of the intermediate at m/z = 201.07 by loss of an additional H. The dissociation of m/z = 201.07 will be easier than that of m/z = 202.08 since the dissociation energy is significantly decreased from 4.40 to 3.16 eV [West et al., 2018a]. There might therefore be enough remaining energy from the dissociation of the parent to lose an additional H. The m/z = 201.07 ion might also get reexcited since its secular frequency is in the excitation range.

From West et al. [2018a] we could retrieve energetics data on pyrene (Ionization energy IE = 7.42 ± 0.01 eV and the dissociation energy E_{diss} = 4.16 ± 0.69 eV) and fluoranthene (IE = 7.845 ± 0.010 eV and E_{diss} = 4.86 ± 1.1 eV). The two isomers are very close in E_{diss}. It is therefore expected to be difficult to differentiate them in terms of dissociation experiments as said in Nourse et al. [1992], Pachuta et al. [1988].

3.3.3 Discussion

In this part we report some plausible fragmentation patterns for the species observed in our experiment in comparison with the results obtained using other dissociation techniques from the literature. Using the excitation window from 3.2.3.3 we can try to assign the different fragments and branching ratios from our experiments to specific

parents. In our CID experiments, the fragmentation cascade stops when the fragments are out of the range of the excitation window and the internal energy of the parent ion is not enough to dissociate anymore. The branching ratios coming from our experiments are therefore related to the rate at which the internal energy is deposited. For instance, we can excite m/z = 202.08 very slowly (low excitation rate) by using a low amplitude ([0 - 100 mV]) and long excitation time (50ms). In this case, we firstly form m/z = 201.07. With increasing amplitude, more m/z = 200.06 is observed. As discussed before, it is not clear if this ion comes from the desexcitation of activated m/z = 202.08 or from reexcitation of the m/z = 201.07 fragment. In some experiments we observed that the m/z = 202.08 parent ion fragments into m/z = 200.06, 199.06 and 198.05 and even into some m/z = 176 (and even m/z = 152.05 and 126.04 in some experiments) and corresponding dehydrogenated species. This indicates that the parent ion has gained enough internal energy to reach higher dissociation channels such as C_2H_2 and C_4H_2 losses and can be explained by the high collision energy tail that is described in the collision energy distribution in Chapter V. All the results are summarized in Table 9 where we have separated the fragments in groups corresponding to the number of carbon loss compared with the parent ions at m/z = 202.08. Since the neutral products cannot be detected neither in our experiments, nor in the previous studies, the formula provided for the neutrals are tentative and does not exclude multiple fragments. An obvious case is that of $2H/H_2$ channel that was discussed in the dissociation of the pyrene cation by West et al. [2014b].

m/z peak	This work	Attribution
		H_x losses
201.07 ($C_{16}H_9$)	√	[b,c,d,e,f](202 - H)
200.06 ($C_{16}H_8$)	√	[b,c,d,e,f](202 - 2H/H_2)/[c,e,f](201 - H)
199.06 ($C_{16}H_7$)	√	[b](202 - 3H)/[c,d,e,f](200 - H)
198.05 ($C_{16}H_6$)	√	[a,b](202 - 4H)/[c,d,e,f](200 - H_2)/[c,f](199 - H)
197.04 ($C_{16}H_5$)	√	[a](202 - 5H)/[c,e,f](198 - H)
196.04 ($C_{16}H_4$)	√	[a](202 - 6H)/[c,f](197 - H)/[f](198 - H_2)
193.03 ($C_{16}H$)	√	[a](202 - 6H)/[c,f](197 - H)/[f](198 - H_2)
		C_2H_x losses
177.07 ($C_{14}H_9$)	√	[c](202 - C_2H)
176.07 ($C_{14}H_8$)	√	[b,c,f](202 - C_2H_2)
175.07 ($C_{14}H_7$)	√	[b](202 - C_2H_3)/[c](201 - C_2H_2)/[c](200 - C_2H)
174.06 ($C_{14}H_6$)	√	[a,b,c](202 - C_2H_4)/[c,d,e,f](200 - C_2H_2) / [e](199 - C_2H)
173.05 ($C_{14}H_5$)	√	[a](202 - C_2H_5) /[c](199 - C_2H_2) / [c,f](174 - H)
172.04 ($C_{14}H_4$)	√	[a](202 - C_2H_6) / [c](198- C_2H_2) / [f](173 - H)
171 ($C_{14}H_3$)	√	[c,f](197- C_2H_2)
170 ($C_{14}H_2$)	√	[c,f](196- C_2H_2) / [f](171 - H)
169 ($C_{14}H_1$)	√	[f](170 - H)
168 (C_{14})	∅	[f](169- H)
		C_4H_x losses
152.06 ($C_{12}H_8$)	√	[a,b,c](202 - C_4H_2)
151 ($C_{12}H_7$)	√	[a,b](202 - C_4H_3) / ([c]200 - C_4H)
150 ($C_{12}H_6$)	√	[a,b,c,e,f](202 - C_4H_4) / [e](201 - C_4H_3) / [c,d,e](200 - C_4H_2)/ [e](199 - C_4H)/ [e](176 - C_2H_2)
149 ($C_{12}H_5$)	√	[a,b](202 - C_4H_5) / [c](199 - C_4H_2)/ [c](150 - H)
148 ($C_{12}H_4$)	√	[a](202 - C_4H_6) / [c](198 - C_4H_2)/ [c,f](174 - C_2H_2)
147 ($C_{12}H_3$)	√	[a](202 - C_4H_7)
146 ($C_{12}H_2$)	√	[a](202 - C_4H_8) / [c](196 - C_4H_2)
		C_6H_x losses
126.04 ($C_{10}H_6$)	√	[b](202 - C_6H_4)
125 ($C_{10}H_5$)	√	[b](202 - C_6H_5)
124 ($C_{10}H_4$)	√	[c](174 - C_4H_2)/ [c](150 - C_2H_2)
123 ($C_{10}H_3$)	√	[b](202 - C_6H_7) / [c](197 - C_6H_2)/ [c](149 - C_2H_2) / [c](198 - C_6H_3)/
122 ($C_{10}H_2$)	√	[b](202 - C_6H_8) / [c](196 - C_6H_2)/ [c](148 - C_6H_2)/[c](123 - H) / [c](199 - C_6H_5)
121 ($C_{10}H_1$)	√	[c](122 - H)
120 (C_{10})	√	[c](121 - H)

Table 9 Analysis of the different m/z species detected in our CID experiments and possible assignment. Previous results published in the literature have also been gathered corresponding to [a]Shushan and Boyd [1980], [b]Pachuta et al. [1988], [c]Nourse et al. [1992], [d]Pyle et al. [1997], [e]Guo et al. [1999], and [f] West et al. [2014b] illustrating the complexity of the dissociation patterns. * m/z peaks correspond to species which are attributed to products of the reactivity in the trap of pyrene fragments with H_2O and potentially O_2 and their subsequent fragmentation by CID (see Figure B.3).

Chapter IV

Using CID to differentiate m/z = 202 PAH isomers

Contents

Through Chapters II and III, I presented the instrument AROMA and its capabilities to detect PAHs and to study their dissociation behavior via the CID technique. The main objective was to develop a CID procedure to differentiate isomeric structures at a given m/z in order to analyse cosmic dust analogues and meteorites.

In this chapter, I will present the application of the CID procedure on three isomers of $C_{16}H_{10}$, namely pyrene (PYR) and two other isomers fluoranthene (FLU) and 9-ethynylphenanthrene (ETHPH). Finally, experiments done towards differentiating these isomers in natural samples (the Allende meteorite) as well as samples produced in a dusty plasma reactor are presented.

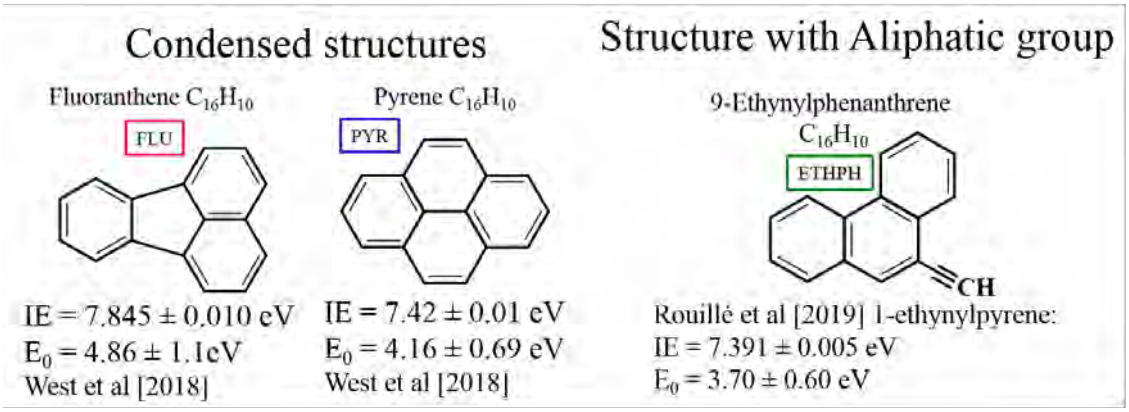

Figure 4.1 Structures, ionization energy IE and dissociation energy E_0 of the studied PAH isomers with m/z = 202

4.1 CID of m/z = 202 isomers

4.1.1 Survival yields of m/z = 202 isomers

We performed CID experiments on resonance (187 kHz) at 200 mV for PYR, ETHPH, and FLU (see Figure 4.2). The loss of the parent ions SY at 50% was investigated as a mean to differentiate the isomers according to Kertesz et al. [2009]. Figure 4.2 shows that the time at which 50% of the parent population is lost is 755/950/1000 μs for ETHPH, FLU and PYR, respectively. Therefore, we can clearly differentiate the condensed structures (PYR and FLU) from the alkylated structure, whereas the two curves corresponding to the condensed structures fall very close. The intersection at 50% is separated but the values fall within the error bars. This means that we are at

the limit of differentiating these types of isomers.

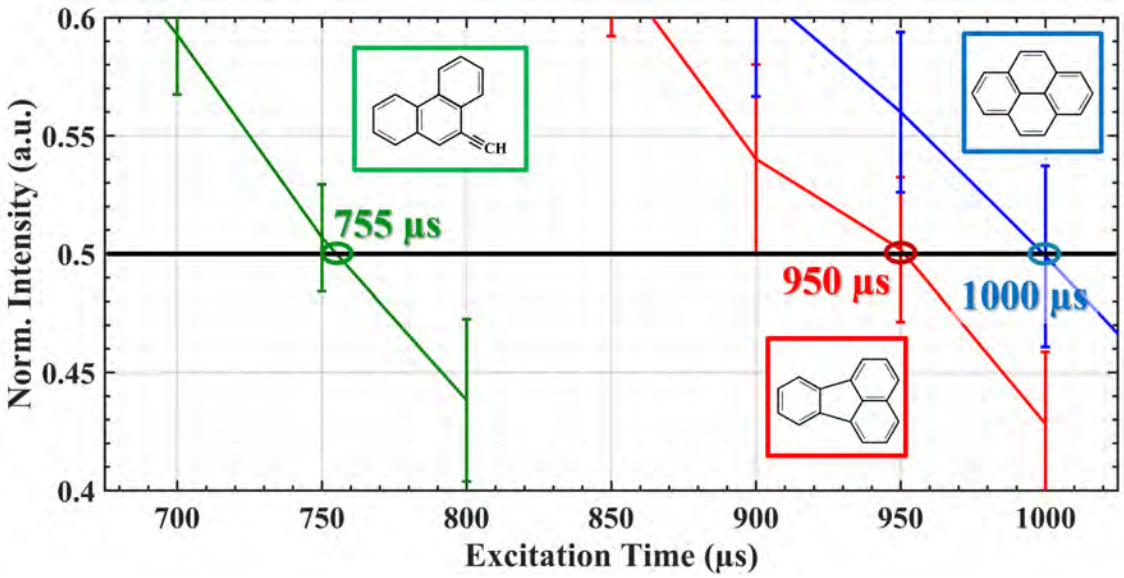

Figure 4.2 Survival yields of the three studied isomers of $C_{16}H_{10}$, namely pyrene (PYR), fluoranthene (FLU) and 9-ethynylphenanthrene (ETHPH). The CID experiments were performed in the same conditions with on resonance excitation and a DE amplitude of 200 mV. Error bars coming from the repetition of the experiments

As explained in Chapter III, the variation of SY with time is rather scattered at an excitation amplitude of 100 mV so the procedure would fail at a amplitude lower than 200 mV. To probe the complexity of any sample it would be interesting to obtain a wider separation between FLU and PYR. We decided thus to use an excitation amplitude of 500 mV leading to the breakdown curves shown in Figure 4.3. However, we observed that the decay curves of PYR and FLU overlap each other to the point that no differentiation could be achieved. This is in line with conclusions made by Pachuta et al. [1988] that using higher amplitude leads to higher internal energy transfer but also a higher probability of isomerization which could lead to undifferentiated fragmentation paths between isomers.

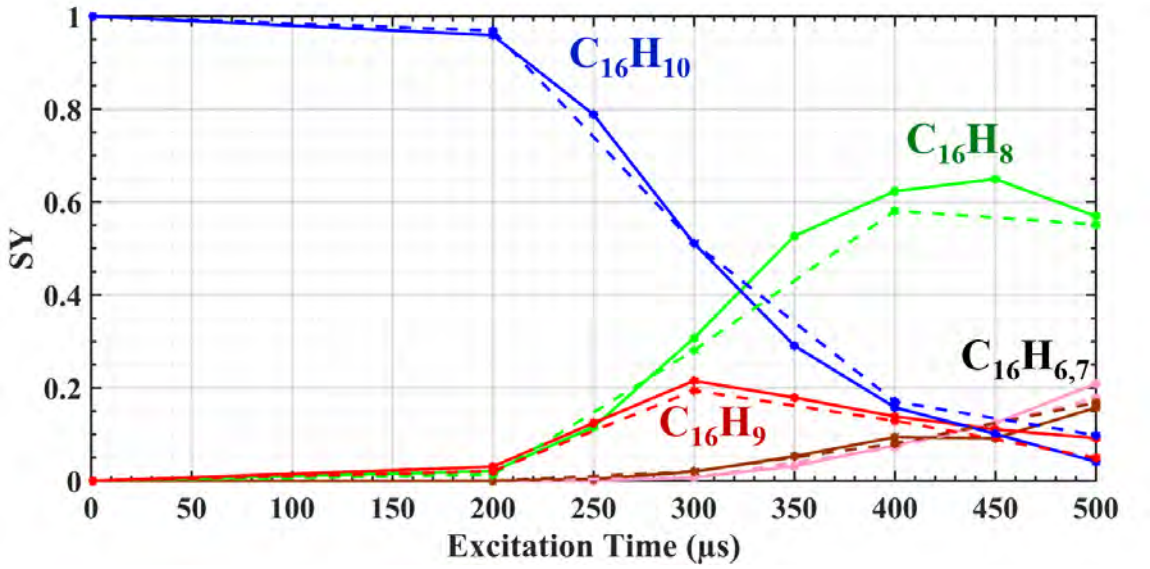

Figure 4.3 Example of a decay curve of PYR (solid Line) and FLU (dashed line) achieved at DE amplitude of 500 mV as a function of time.

4.1.2 Carbon loss of m/z = 202 isomers

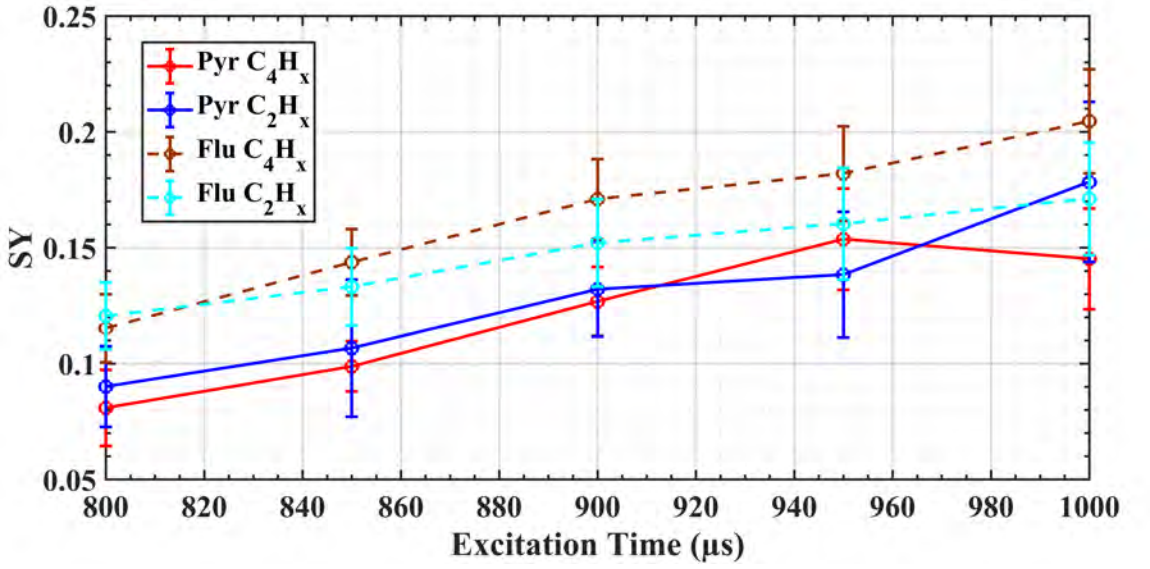

Figure 4.4 Relative evolution of the losses of C_2H_x and C_4H_x in an attempt to differentiate the two isomers FLU and PYR. From CID experiments on resonance and with a DE of 200 mV.

In addition of hydrogen loss, the compact parent isomers exhibit some very weak carbon loss channels. In Figure 4.4, we can observe that while the quantities of C_2H_x are very close for both isomers, FLU forms more C_4H_x than PYR which has also been noticed by Shushan and Boyd [1980]. However from the width of the error bars (de-

rived by repeating the experiments) it is hard to conclude that this is a differentiation criterion between FLU and PYR. A similar conclusion was obtained in the literature for experiments at high collision energy (Pachuta et al. [1988], Nourse et al. [1992], Pyle et al. [1997]). This has been explained as possible isomerization at the achieved high internal energies.

4.2 Mixture of pure PAHs

After measuring the time at which the survival yields reach 50% for each isomer, the next step was to see how this value will change if the sample contains two of these isomers. Two samples of PAH mixtures were prepared, the first one containing an equimolar mixture of PYR and FLU (PF) and the second one an equimolar mixture of PYR and ETHPH (PE). Fullerene C_{60} has been introduced in the solution to have a matrix that helps desorbing the isomers with comparable efficiency.

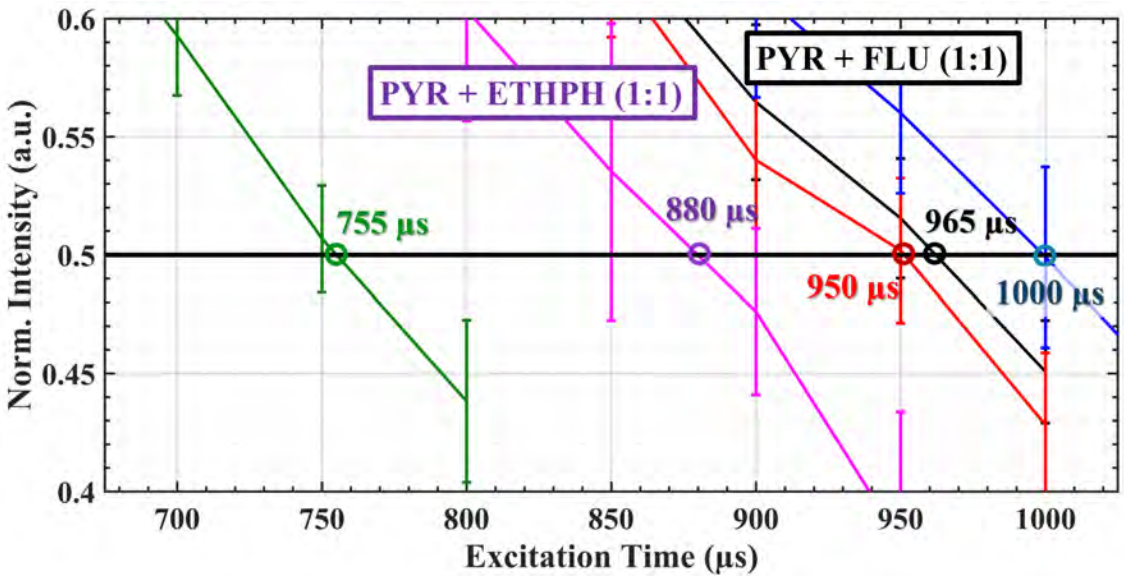

Figure 4.5 Survival yields of the three isomers and the mixtures (PE and PF) at 200 mV excitation amplitude as a function of time. The time at which 50% of the parent population is lost is 755/880/950/965/1000 μs for ETHPH/PE/FLU/PF/PYR respectively.

Figure 4.5 presents the decay curves of the two samples for a DE amplitude of 200 mV. They show the excitation time leading to 50% of dissociation of the parent ion m/z = 202. As expected, the curves of the two mixtures lie in between the decay curves of the isomers composing the mixture.

Figure 4.6 shows a different representation of the times associated with 50% survival

yield in which the width of the rectangles corresponds to the uncertainties. The latter have been determined as illustrated in Figure 4.7. We observed that the uncertainties from the mixture of PYR and ETHPH is very wide which can be explained by the fact that the curves of the two isomers are far from each other and there is likely some dispersion in the mixture associated with the ion production by L2MS.

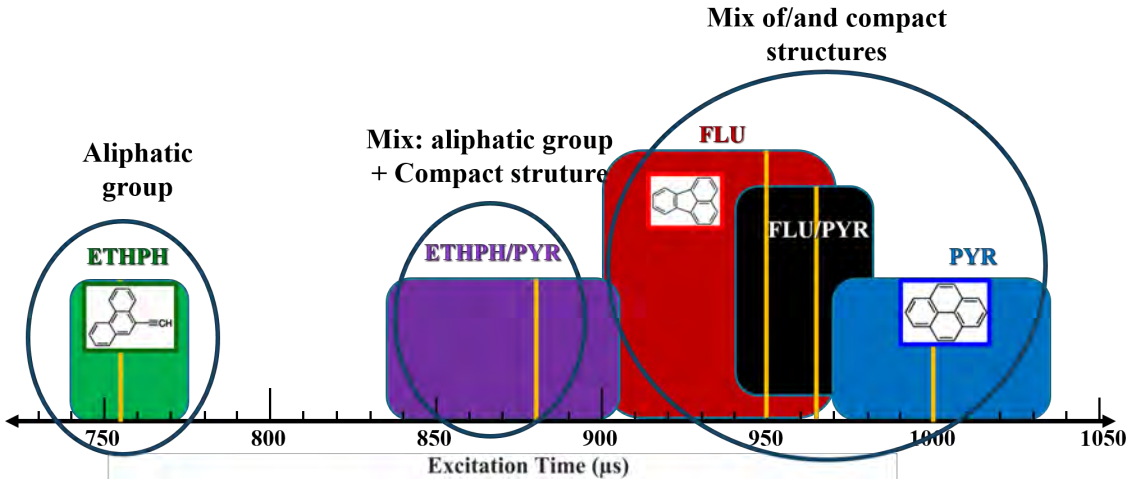

Figure 4.6 Scheme summarising the times associated with 50% survival yield of the three studied isomers of $C_{16}H_{10}$, namely pyrene (PYR), fluoranthene (FLU) and 9-ethynylphenanthrene (ETHPH), and their mixtures. The CID experiments were performed with DE on resonance (187 kHz) and at 200 mV. The values correspond to 740<755<775 μs for ETHPH (in green), 835<880<905 μs for the equimolar mixture of PYR and ETHPH (in violet), 900<950<975 μs for FLU (in red), 940<965<980 μs for the equimolar mixture of PYR and FLU (in light blue), and 970<1000<1035 μs for PYR (in dark blue).

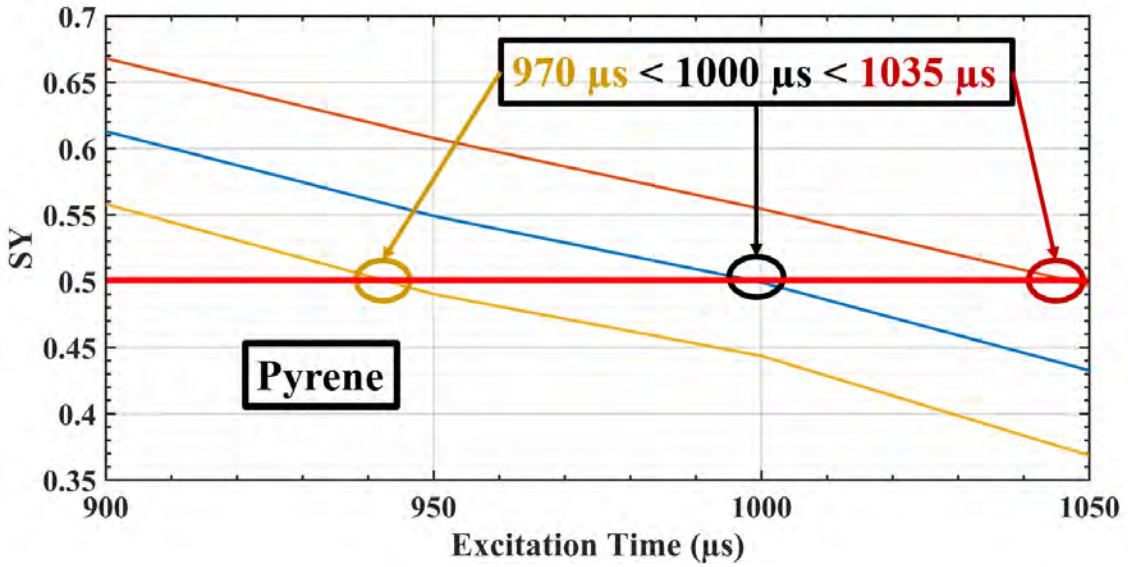

Figure 4.7 Description of the procedure of the projection to evaluate the errors of the measurements as used in Figure 4.6.

4.3 Application to complex samples

4.3.1 Plasma dust analogues

This part deals with the analysis of dust particles collected in a low-pressure plasma excited at electron cyclotron resonance (ECR) produced in pure acetylene (C_2H_2). This work is leaded by Richard Clergereaux at LAPLACE (University of Toulouse/CNRS). The reactor is described elsewhere (Rojo et al. [2019].; Lagarde et al. [2001]). It operates by coupling microwave electromagnetic field (2.45 GHz) with the cyclotron gyration of electrons in a static magnetic field, at really low-pressure (typically from 0.1 to 7 mTorr). After a cleaning procedure dealing with a 10 min of oxygen plasma followed by 5 min of argon plasma, the plasma is produced in pure acetylene. The gas is injected at a constant flow rate, monitored by a mass flow controller, resulting in a working pressure in the 0.3 – 3 mTorr range – the residual vacuum obtained by a combination of rotary and turbomolecular pumps being less than $7.5x10^{-4}$ mTorr. The plasma is ignited by optimizing the injection of 200 W in the microwave antennae. Dust particles are formed after few minutes and transported in the plasma volume Rojo et al. [2019] or on the reactor walls. For ex-situ analyses, 3 cm × 3 cm stainless steel samples were positioned above the central cusp and a carbon tape being used to have good electrical and thermal contact between the sample and the reactor. In this work, we focus on three samples that have been produced with 0.6 mTorr pressure of C_2H_2 at three different times, 5, 8 and 10 min. The AROMA spectra show that they present a really rich molecular composition: it includes various PAHs - up to coronene with a predominance of pyrene - but also, and surprisingly in cold plasmas, carbon clusters. It has been shown, using mass spectrometry and IR spectroscopy (Deschenaux et al. [1999]) as well as numerical simulations (De Bleecker et al. [2006]), that PAHs can be formed in abundance in acetylene RF capacitively-coupled plasmas. Figure 4.8 presents the mass spectrum of the sample produced at 5 min. From m/z = 100 to 250 a series of carbon cluster (C_x species) and PAHs have been detected with m/z = 202 ($C_{16}H_{10}$ dominating the spectrum of the PAHs).

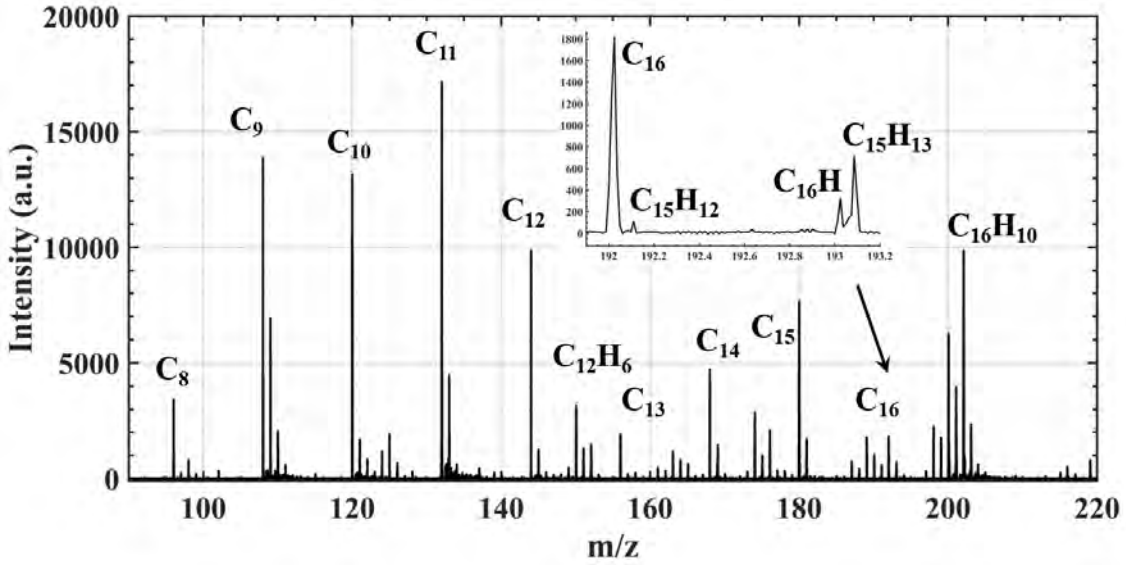

Figure 4.8 Mass spectrum of dust sample produced in 0.6mTorr of C_2H_2 for 5 minutes in a plasma reactor.

We applied the CID procedure to check which types of isomers are contributing to this peak. Figure 4.9 presents the dissociation decay curves of the m/z = 202. It intersects with the loss at 50% at 1040/1000/800 μs for the samples at 5/8/10 minutes respectively.

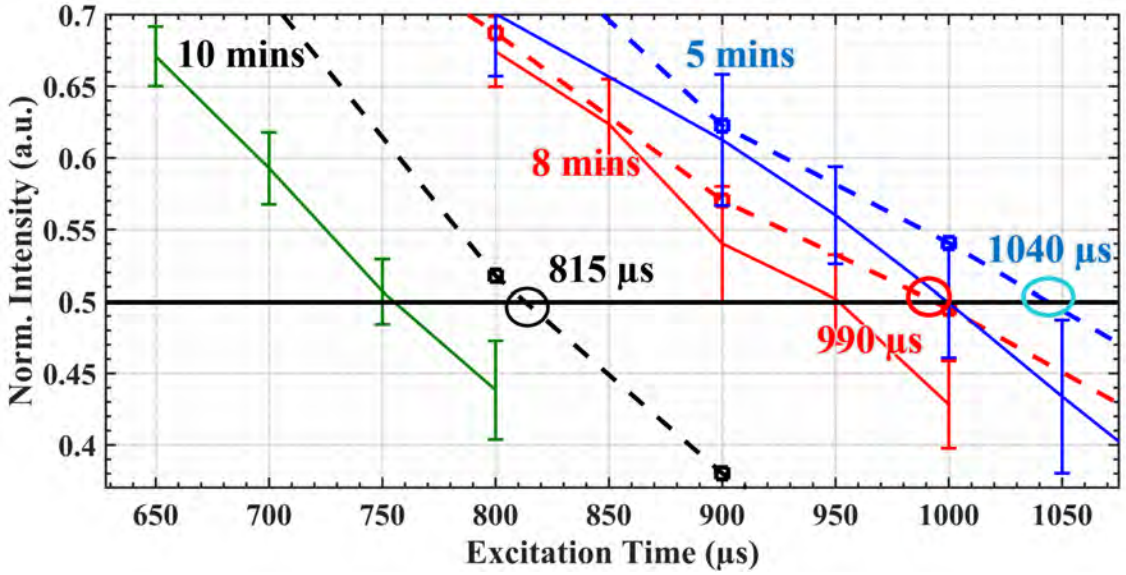

Figure 4.9 Decay curves of the isolated m/z = 202 peak, for CID experiments under on resonant excitation (187 kHz) at 200 mV. Plasma dust samples (dashed lines) using C_2H_2 as precursor for 5/8/10 minutes at 0.6mTorr pressure are compared with samples of pure isomers and their mixtures (plain lines).

From Figure 4.6, we can see that 50% dissociation of the parent ion occurs at 755

μs in the case of ETHPH and around 905-977 and 970-1035 μs for FLU and PYR, respectively. For the dusty plasma sample at 5 and 8 minutes, the SY is on the verge just at the limit of the error bars coming from PYR which suggest that it is entirely PYR or likewise. In the experiment at 10 minutes, the 50% of the SY is reached after 800 μs. This value is very close to the one of ETHPH (755 μs) which means that there is an important fraction of a less compact structure such as ETHPH.

This result suggests a change in the chemistry from short (5 mins) to longer times (>8 mins). It would be interesting to connect the trend observed in molecular structure with the evolution of dust particles in the plasma and the possibility for surface chemistry on the reactor walls.

4.3.2 Allende Meteorite

We introduced in chapter I (section 1.2.3) the presence of PAHs in meteorites especially in Murchison. The peak m/z = 202 is a major or dominant peak in this carbonaceous meteorite. To apply our technique on such complex samples we studied two samples of the Allende carbonaceous meteorite. We analyzed a fragment taken from the internal part of the meteorite and another one from the external part. The peak m/z = 202 dominates the mass spectrum of the samples taken from the internal part of the meteorite (Figure 4.10). This observation is reproduced with the sample taken from the crust (external part) of the meteorite. Our results are in great agreement with the ones achieved by Zenobi et al. [1989], considering that these species are heterogeneously distributed in the meteorite samples.

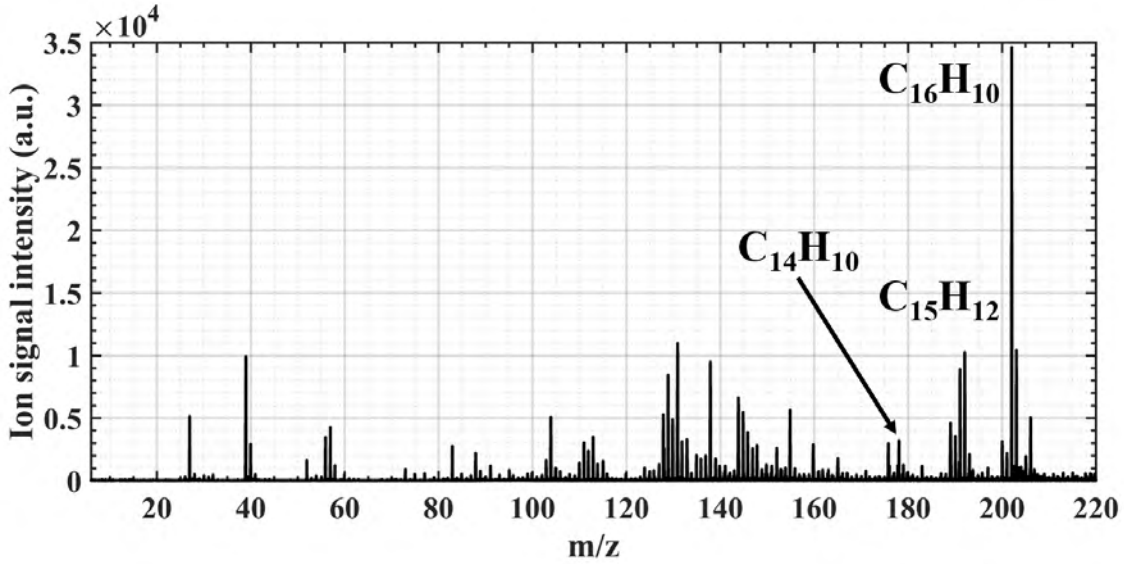

Figure 4.10 Mass spectrum from the Allende meteorite (internal part) achieved with the AROMA set-up

Thus, we decided to apply our CID technique to get insights on the isomeric structures distribution at this m/z.

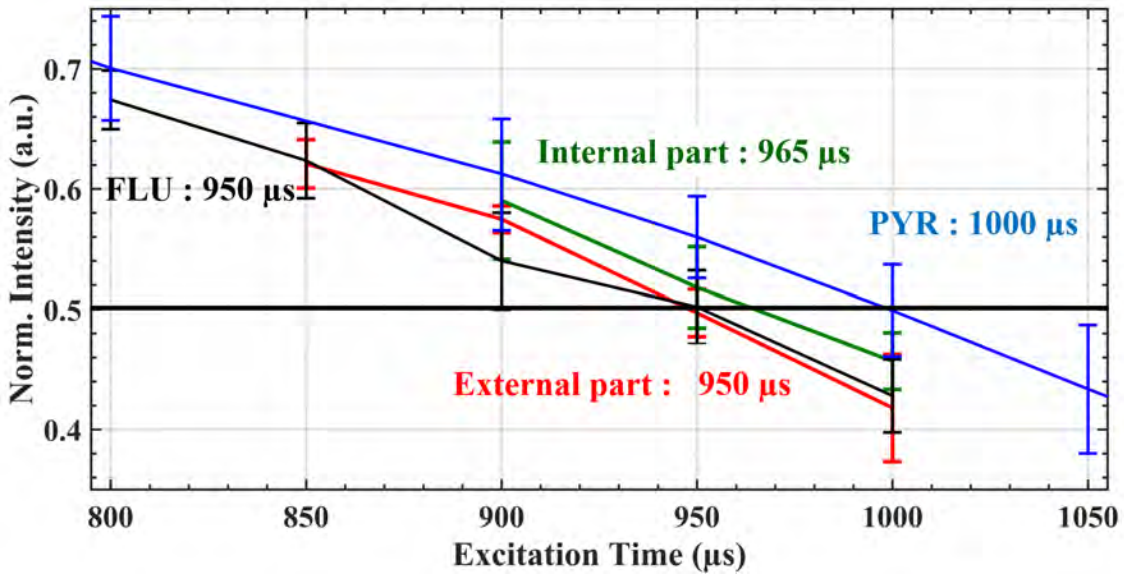

Figure 4.11 Decay curve of the isolated m/z = 202 peak from Allende samples, for CID experiments under on resonant excitation (187 kHz) at 200 mV.

In Figure 4.11, we observe that the time to reach SY of 50% is at 965 μs for the internal part and 950 μs for the external part of the Allende meteorite. Both Allende samples show the tendency to be mostly composed of compact structures of m/z =202. Their SY curves fall in between the two SY curves of FLU and PYR. The SY curve of

the external sample almost overlap with the one of FLU suggesting that the latter is dominant in this sample. The SY curve of the internal sample suggests that the peak at m/z = 202 is a mix of both PYR and FLU. Zenobi et al. [1989] suggested in his L2MS study that his technique is more sensitive to PYR than FLU. To our knowledge, our work is therefore the first discussion on isomeric structures in Allende meteorite.

Chapter V

Insights into dissociation dynamics of m/z = 202

Contents

In this chapter, we discuss three applications of the modeling of the ion dynamics, kinematics and energetics in order to:

- Get insights on the behavior of the ions in the Q_2 segment of our AROMA set-up,
- Get information on the collisional dynamics,
- Determine dissociation dynamics parameters.

5.1 Ion dynamics in the trap

The Simion software (Dahl et al. [1990]) allows us to calculate electric and magnetic fields as well as the trajectory of charged particles in these fields. We used it to model our trap and simulate the ion motion/behavior in the trap.

In Figure 5.1, we show the model,

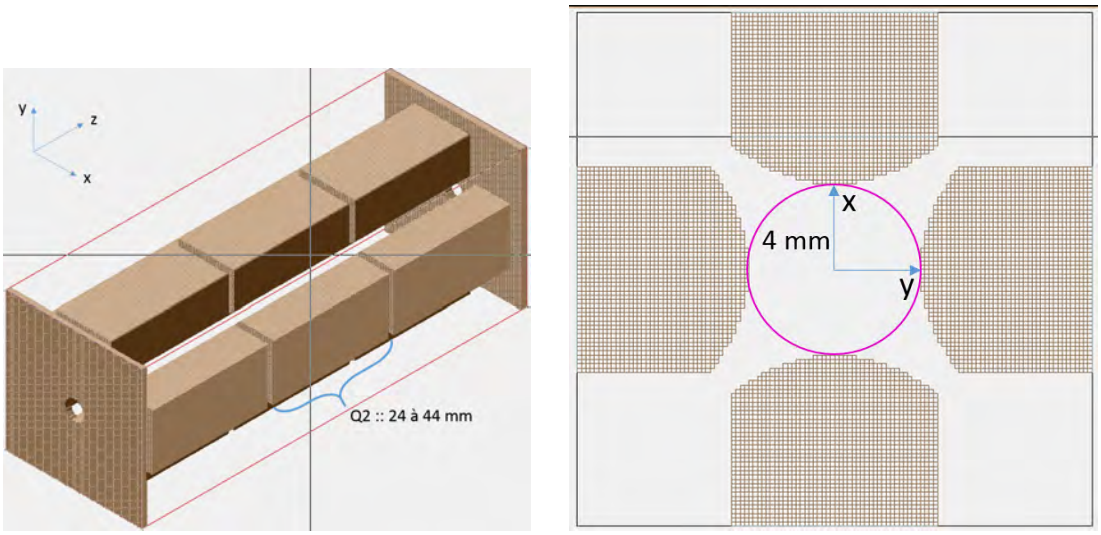

Figure 5.1 Scheme of the simplified model of the Q2 from the LQIT that is used in Simion simulations.

Simion can adapt calculations to minimize the number of operations and accelerate the simulations. To do so Simion calculates the electric potential surface (EPS) in the simulated space. Thus, at each time step, the program calculates the position and velocity of the particle depending on the parameters from the previous frame. Depending on the position of the ion on the EPS and the parameters of the EPS at this point the program determines a relative time step to achieve the highest precision in the calculations in the shortest time. A particle in a region of the EPS where the potential lines are denser (the variation of the electrical potential are sharper) will

experience much changes and thus more steps will be needed to achieve the same result in the calculations than for an ion in a uniform electrical potential.

Using the formalism of the .gem files (where an object is described by geometric forms), we could construct the 3D model presented in Figure 5.1 representing the Q_1, Q_2 and Q_3 segments of the LQIT in AROMA, used to calculate the dynamics of ions.

The simulations on the arrival of the ions in the ion trap and their translational cooling were previously performed by Fasmatech. We thus concentrated on the behavior of already trapped ions.

Trapping conditions After creating the model, we began performing simulations for an ion at m/z = 300 (coronene, $C_{24}H_{12}$). This is due to the fact that these simulations were performed at the beginning of this PhD when studies on coronene were performed for the commissioning of AROMA together with Fasmatech.

I modeled the motion of the ions in the trap to understand the conditions and get "the picture" of the behavior of the ions in the ion trap (see Figure 5.2). Here only the trapping conditions are applied which is called "driving" the ions, as described in Chapter III and recalled in Equation 16 with frequency $f_1 = 1300\,\text{kHz}$ and amplitude $V = 180\,\text{V}$ for $500\,\mu\text{s}$ of simulated lifetime of the ion.

$$RF = \quad U + V \quad \cdot \cos(\omega_1 t + \phi_1) \tag{16}$$

The following figures (5.2 and 5.3) contain 5 sections:

- on top in red, the kinetic energy (K in eV) of the ion through time,
- in the middle in blue, its distance from the center of the trap (r in mm),
- down left is a representation of the radial evolution seen in the z section of the trap (see Figure 5.1) with the pink oval circle representing the limits of the trap.
- Down right, the motion of the ions through the x and y sections of the trap is shown (see Figure 5.1).

The time of the experiment is represented with a color ladder from dark blue at $0\,\mu\text{s}$ through green, yellow orange and dark red for $500\,\mu\text{s}$.

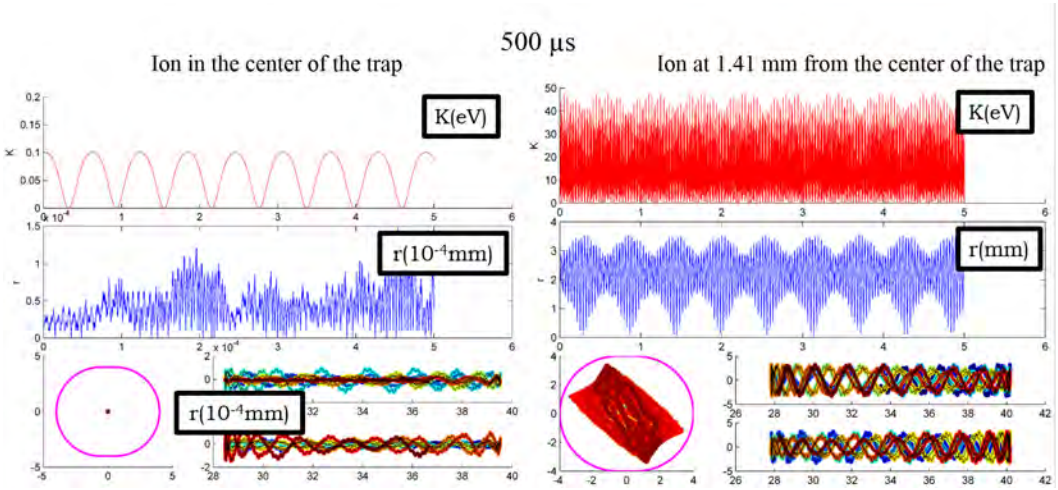

Figure 5.2 Simulations with Simion of the coronene cation motion in the Q2 segment of the AROMA set-up with trapping conditions corresponding to RF frequency = 1300 kHz and V = 180 V. The ion is "created"in the center of the trap (*on the left*), and at 1.4 mm from the center (*on the right*)

As expected under trapped conditions, the ions will stay in an orbit combining acceleration and deceleration phases, which comes from the geometry of the trap (when getting closer to an electrode the ion will slow down until stopping before being accelerated by the opposite potential of the electrode) and the alternative polarity of the electrodes which will guide the motion of the ions in another oscillating motion. Thus we noticed that, under these particular trapping conditions (V = 180 V, F = 1300 kHz), coronene cations will achieve a maximum kinetic energy at the limit of the orbit somewhere between 50 and 60 eV reaching higher kinetic energy till collision with the electrodes or escaping from the trap. We could also see that the difference in kinetic energy is closely related to their position in the LQIT.

5.2 Interaction between trapped/excited ions and rare gas

The previous simulations are interesting to understand the general behavior of the ions in the trap but they correspond to a case with no background gas, which is not realistic. Thus we also want to study the interaction of the ions with neutral gas in two conditions, one in which they experience only the trapping mode (which would lead to kinetic and internal cooling as explained in Chapter III) and one in which they are accelerated by a DE (which is the CA method of our CID experiments, see Chapter III). In the latter case, the ions are simultaneously accelerated by the DE and slowed

down through collisions with the background rare gas.

We implemented the hard sphere model code supplied in Simion to quantify ion kinematics induced by collisions with the buffer rare gas. Since Simion is not well suited to perform calculations on the internal energies of ions, the transfer from kinetic energy to internal energy is later evaluated.

We considered the studied ion as a sphere with diameter of 9 Å. The simulations for one ion is shown in Figure 5.3. It shows that after 0.5 ms, the ion will be kinetically cooled down and thus driven closer to the center of the trap.

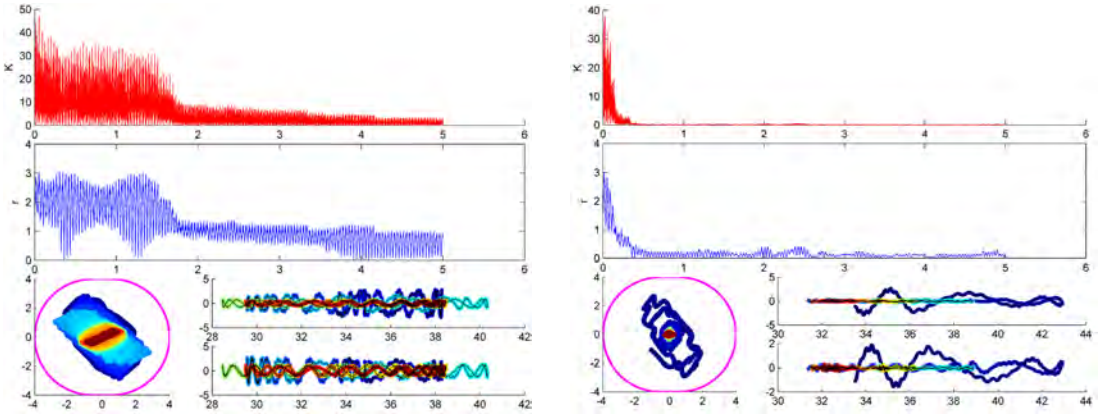

Figure 5.3 Simulations with Simion of the coronene cation motion in the Q2 segment of the AROMA set-up with trapping conditions corresponding to RF frequency = 1300 kHz and V = 180 V. In this case, the ion is"created"off the center at 1.41 mm with 10^{-3}(*on the left*) and 10^{-2} mbar(*on the right*) of Ar.

To perform these simulations, we needed to take in account the evolution of the pressure of the rare gas after injection of a gas pulse, which was obtained from the calibration provided by Fasmatech with AROMA. We therefore considered a range in the Helium pressure between 10^{-2} and 10^{-3} mbar for at least 50 ms.

Recalling the formula of the energy in the center of masses:

$$E_{\text{coll}}^{gas} = \frac{m_{gas} \cdot K_{ion}}{m_{gas} + m_{ion}} \tag{17}$$

With:

- $m_{ion} = 300$ for coronene
- $m_{gas} = 4$ for He
- $10 \cdot m_{gas} = 40$ for Argon
- and K_{ion} the kinetic energy of the ion upon collision.

$$
\begin{aligned}
E_{com}^{He} &= \frac{m_{gas} \cdot K_{ion}}{m_{gas} + m_{ion}} & E_{com}^{Ar} &= \frac{10 \cdot m_{gas} \cdot K_{ion}}{10 \cdot m_{gas} + 300} \\
E_{com}^{He} &= \frac{4 \cdot K_{ion}}{4 + 300} & E_{com}^{Ar} &= \frac{40 \cdot K_{ion}}{40 + 300} \\
E_{com}^{He} &= \frac{4}{4 + 300} \cdot K_{ion} & E_{com}^{Ar} &= \frac{40}{40 + 300} \cdot K_{ion} \\
E_{com}^{He} &= 0.013 \cdot K_{ion} & E_{com}^{Ar} &= 0.12 \cdot K_{ion}
\end{aligned} \tag{18}
$$

In order to describe the kinetic energy cooling rate by collisions, we retrieve from the Simion calculations the collisional frequency (or time between collisions T_{coll}) and E_{com} (the corresponding energy in the center of masses). To minimise the computational time, the simulations were performed using Ar as the cooling gas rather than He increasing E_{com} by a factor of 10 (see Equation 18), which implies that the ions will lose their kinetic energy ten times faster.

In Figure 5.3 we observe that after 500 μs the ions are kinetically cooled with an energy below 0.5 eV corresponding to the kinetic energy of the rare gas atoms at room temperature. At 10^{-3} mbar of Ar a bit more time would be needed to cool down (typically 5 ms). Thus in order to achieve internal energy cooling (which takes place in spans of tens of milliseconds) for all the ions, we choose to change the delay given to the ions to cool down in the experiment to 100 ms with a pressure assumed to be between 10^{-3} and 10^{-2} mbar.

Ion kinematics and energetics From this point on, the simulations are done for ions with m/z = 202. Now the aim is to accelerate the ions in the LQIT in the presence of a buffer pressure of Ar. A first step was to determine the secular frequency f_s in our numerical experiment. Figure 5.4 shows the evolution of the maximum of the kinetic energy of ions in the trap as a function of the excitation frequency.

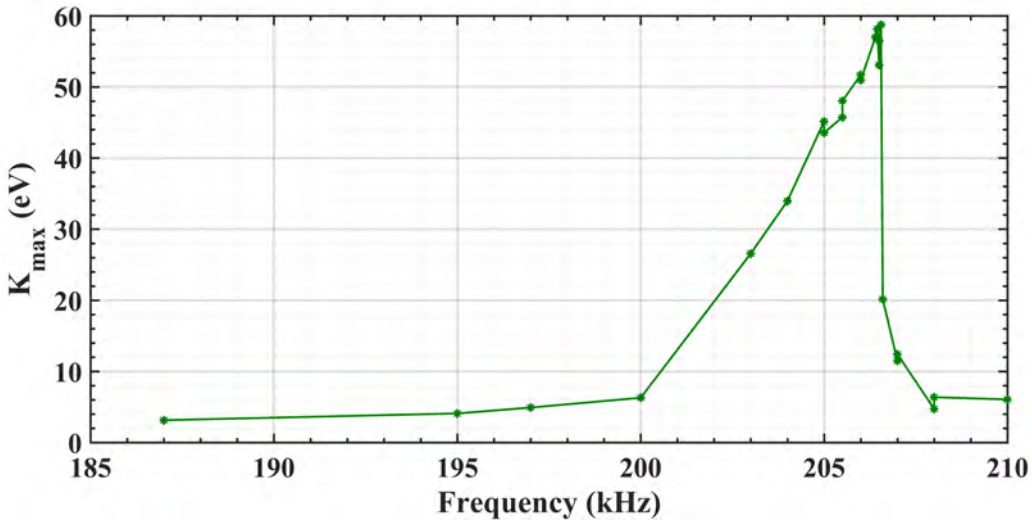

Figure 5.4 Evolution of the maximum of the kinetic energy of a ion at m/z = 202 excited through with DE amplitude at 200 mV.

We observe that the excitation efficiency is not symmetrical and the maximum is achieved for $f_s = 206.5$ kHz which corresponds to the value calculated in Section 3.2.3.2. This frequency is then used in all the simulations with a DE.

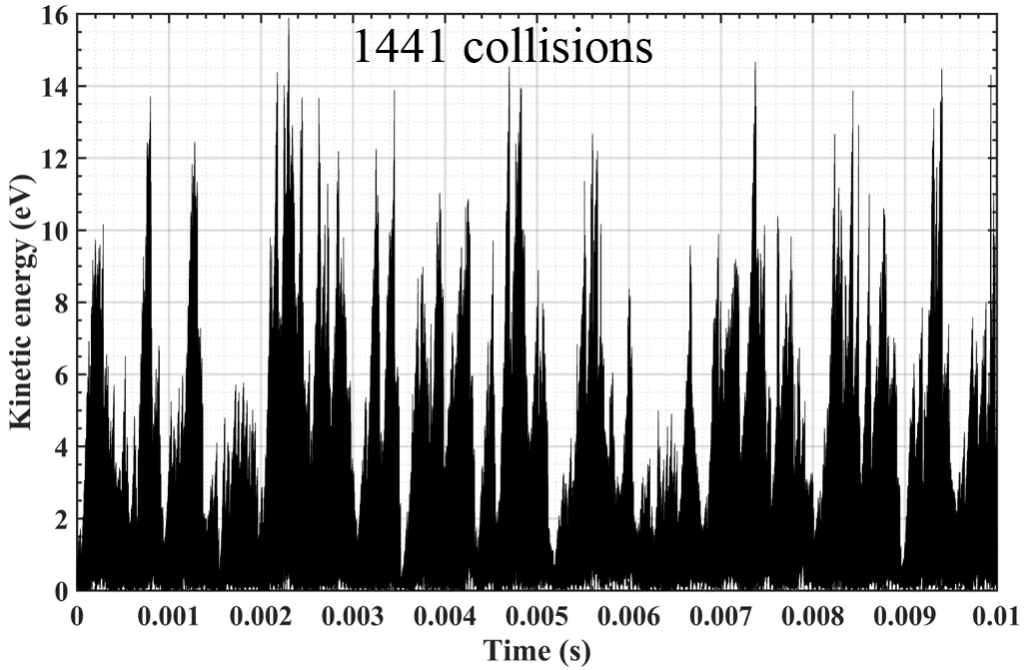

Figure 5.5 Evolution of the kinetic energy of a ion excited through on resonance DE at 200 mV with 10^{-3} mbar of Ar buffer gas pressure.

We start the simulations by selecting an ion with kinetic energy within a Boltzmann distribution at room temperature. The ion undergoes collisions and accelerations for

a long time (see Figure 5.5) and for each collision we retrieve the kinetic energy (E_{kin}) and the time between two collisions ($\mathrm{T_{coll}}$). Since both parameters are independent, we assume that letting 10 ions evolve under these conditions for a time t is the same as using a single ion for a duration of $10\,t$. We then derive the distributions for E_{kin} (E_{com}) and $\mathrm{T_{coll}}$ that are used in a script using the Monte-Carlo method described in the next section (see Figure 5.6).

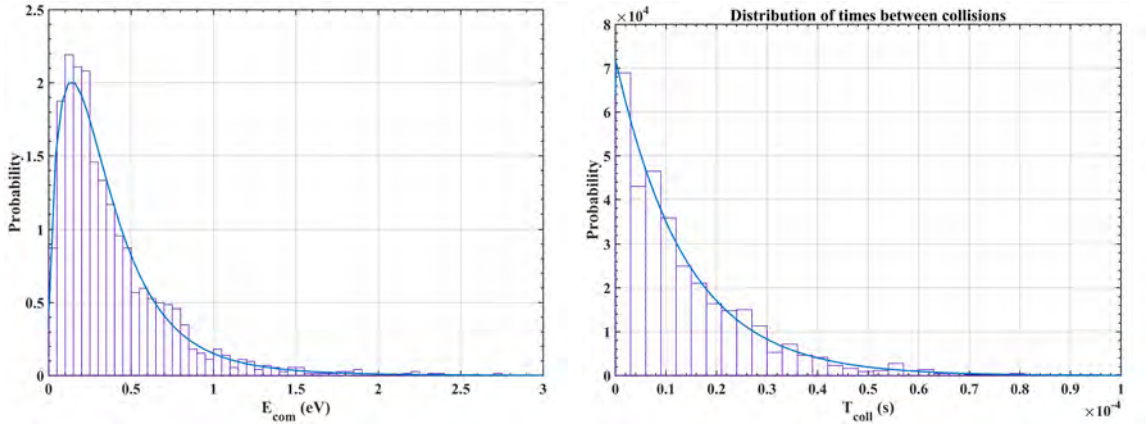

Figure 5.6 Calculated distributions of E_{com} and the time between collisions, $\mathrm{T_{coll}}$, for a DE at 200 mV and 10^{-3} mbar of Ar buffer gas pressure.

Theses distributions have been fitted using classic distribution functions available in the Matlab software (Dorf and Bishop [1998]). The best fit are an exponential distribution for the $\mathrm{T_{coll}}$ and a Burr (Type XII) distribution for $\mathrm{E_{com}}$ (see equations 19 and 21).

$$Dist_{exp}(x;\lambda) = \begin{cases} \lambda e^{-\lambda x} & x \geqslant 0 \\ 0 & x < 0 \end{cases} \tag{19}$$

$$Dist_{Burr}(x;c,k) = ck\frac{x^{c-1}}{(1+x^c)^{k+1}} \tag{20}$$

In order to get insight into the evolution of these distributions with the conditions of the simulations we reported the median of each distribution in Table 10.

As expected, we observe that increasing the amplitude of the DE leads to an increase of $\mathrm{E_{com}}$ while $\mathrm{T_{coll}}$ decreases (aka the collisional frequency increases). With increasing the background gas pressure we observe a decrease in both $\mathrm{T_{coll}}$ and $\mathrm{E_{com}}$. The increase

Pressure \ Amplitude		20 mV	40 mV	200 mV	400 mV	600 mV
10^{-3} mbar	$E_{com}^{med,Burr}$(eV)	3· 10^{-2}	4.4· 10^{-2}	0.289	0.739	1.08
	$T_{coll}^{med,exp}$ (s)	3· 10^{-5}	1.9· 10^{-5}	9.7· 10^{-6}	6.4· 10^{-6}	5.5· 10^{-6}
10^{-2} mbar	$E_{com}^{med,Burr}$(eV)	1.4· 10^{-2}		4.1· 10^{-2}		0.157
	$T_{coll}^{med,exp}$ (s)	2.6· 10^{-6}		2· 10^{-6}		1.4· 10^{-6}

Table 10 The median of the measured distributions of T_{coll} and E_{com} from the simulations performed with Simion, as a function of the DE amplitude and background gas pressure.

in pressure leads to a shorter time between collisions which prevents the ions to achieve higher kinetic energies.

5.3 The Monte-Carlo method

In order to take advantage of the collisional data extracted from the simulations with Simion we used a Monte-Carlo method in two dimensions. Randomly drawing within the E_{com} and T_{coll} distributions, it builds a 10^5x3000 matrix containing the evolution of the internal energy of 10^5 ions after they undergo 3000 collisions. The time and energy are drawn randomly for each event of each ion. Therefore the total time and internal energy depend on the ions. In order to match the experimental time window it is necessary to draw enough collisional events.

With this Monte-Carlo method the energy of the ions could increase without any limit. Since our aim is to fit the experimental breakdown curves, we need to incorporate the competition between the increase of internal energy and the dissociation. This is done by comparing T_{coll} with the inverse of the dissociation rate k_{diss}^{-1}. If the T_{coll} drawn in the distribution is lower than the k_{diss}^{-1} then the collision occurs and the heating continues. If k_{diss}^{-1} is shorter than the drawn T_{coll} then we consider that the ion will have dissociated prior to the collision.

5.4 Adjusting the η energy transfer parameter on pyrene

The value of E_{com} cannot be used directly to build up the internal energy of the ions because it represents the maximum energy that can be transferred from kinetic into internal energy. The energy that is actually transferred can be in the order of few tens of percents and even less than ten percents of E_{com} (Drahos and Vékey [2001];Mayer

and Poon [2009]). Thus we introduce a conversion parameter η which will be adjusted to reproduce the experimental data following Equation 21.

$$\Delta E_{int} = \eta \times E_{\text{com}} \tag{21}$$

with ΔE_{int} the actual kinetic energy that is transfered into internal energy upon collision. The internal energy will increase until reaching the point at which dissociation will occur ($1/k_{diss} > T_{coll}$). In these simulations, we used the value of k_{diss} for PYR, which is provided in West et al. [2018a].

Figure 5.7 represents the simulated survival yield (SY, see section 3.3) (in light blue) achieved after adjusting the values of the η parameter. The derived values for η are represented in Figure 5.8 and are found to decrease with the excitation time. This decrease can be due to the variation of the gas pressure inside the trap following the pulsed injection of the buffer gas. It can also be due to a less effective energy transfer at larger internal energies (as represented in Figure 5.8) as explained in Mayer and Poon [2009] and Drahos and Vékey [2001].

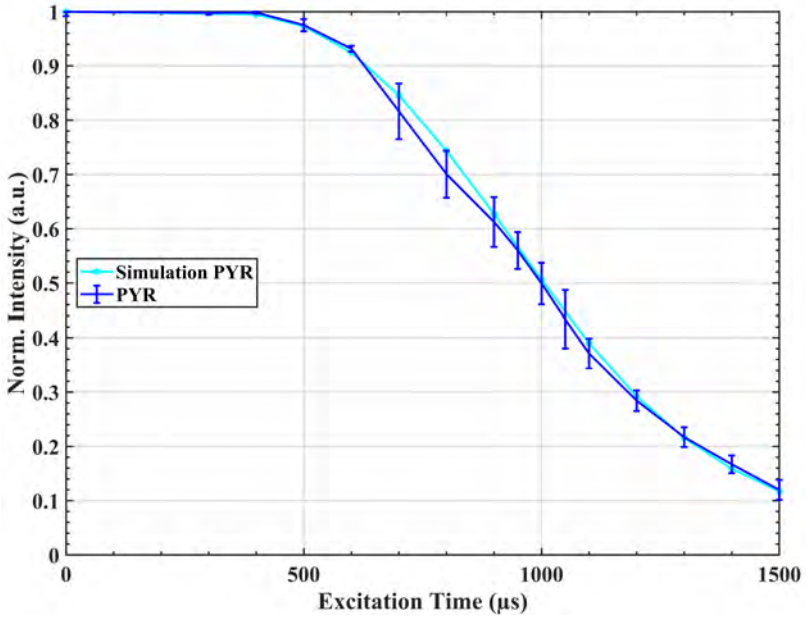

Figure 5.7 Simulated decay of PYR compared to the CID experiment performed on resonance at 200mV

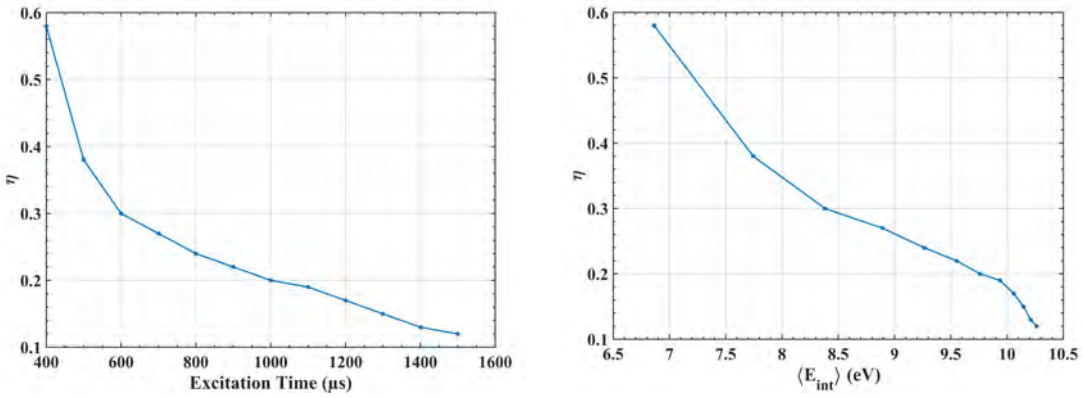

Figure 5.8 Evolution of the η parameter through excitation time and as a function of $\langle E_{int} \rangle$.

The distributions of internal energy for pyrene cations over excitation time are shown in Figure 5.9. They could be extracted from our simulations by treating the competition between heating by collisions and dissociation. They show that the highest energies as well as dissociation are reached after 0.6 ms and this corresponds to an energy E_{diss} around 11 eV.

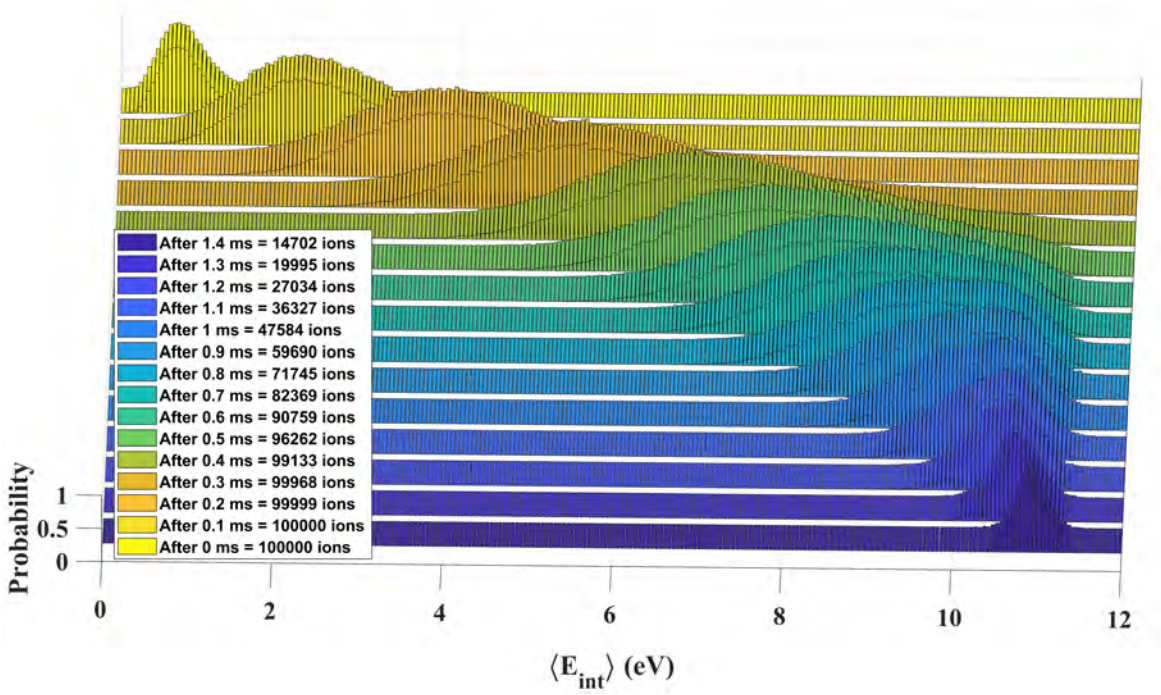

Figure 5.9 Calculated distributions of E_{int} as a function of time for pyrene ions activated by collisions in Ar gas. In the inset, we report the number of remaining ions through time.

5.5 Extracted dissociation rates for the other m/z = 202 isomers

The values of the η parameter that we derived is specific of the excitation conditions (DE characteristics, gas pressure and time). Using the same excitation conditions, we can assume that the values of η remain the same for all isomers. Since the values of E_{com} are also independent on the isomers in the Simion calculations, the only difference that we have to take into account is the variation of the dissociation rate between isomers. Since k_{diss} has been reported by West et al. [2018a] for FLU, we simulated the SY of this ion. The obtained curve appears to be in very good agreement with the experiment (see Figure 5.10), which provides support to our approach.

The value of k_{diss} for ETHPH is unfortunately not known. Rouillé et al. [2019] recently determined an activation energy $E_0 = 3.70\,eV$ for the ethynyl group in the 1-ethynylpyrene cation. From this value we decided to estimate the dissociation rate of ETHPH based on the Laplace transform of the Arrhenius law as explained in Boissel et al. [1997]:

$$k_{diss} = A_{diss}\frac{\rho(E_{int} - E_0)}{\rho(E_{int})} \tag{22}$$

where A_{diss} is a pre-exponential factor and ρ is the harmonic density of vibrational states that can be calculated using the Beyer & Swinehart algorithm (Beyer and Swinehart [1973]) and the list of harmonic vibrational modes listed in the theoretical spectral database of PAHs (Malloci et al. [2007]) (in the absence of ETHPH in this database, we used the modes of PYR).

We then performed our simulations to extract the best value for A_{diss} and therefore k_{diss}. The result of the fitting process can be seen in Figure 5.10 which shows the comparison between the experimental data (with error bars) and the calculated one. A value of A_{diss}=$5{\cdot}10^{15}\,s^{-1}$ was derived. The evolution of k_{diss} with internal energy for the different isomers is summarised in Figure 5.11. It illustrates the much higher dissociation rate of ETHPH relative to PYR and FLU.

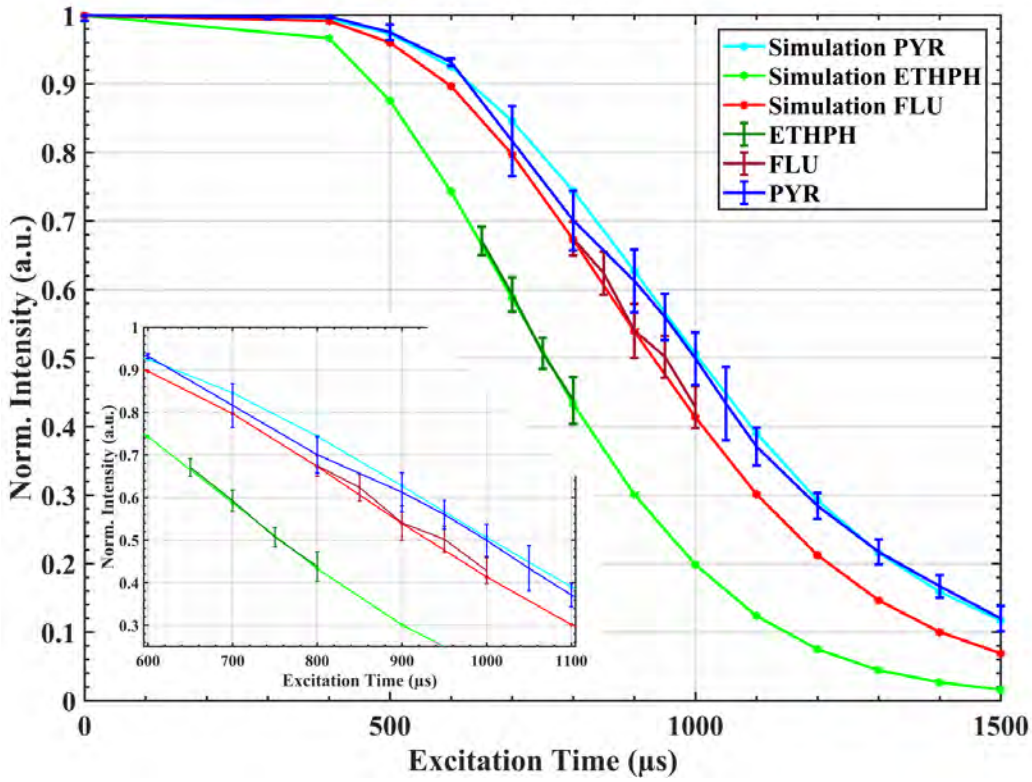

Figure 5.10 Comparison between calculated (line) and experimental (line with error bars) SY for PYR, FLU and ETHPH.

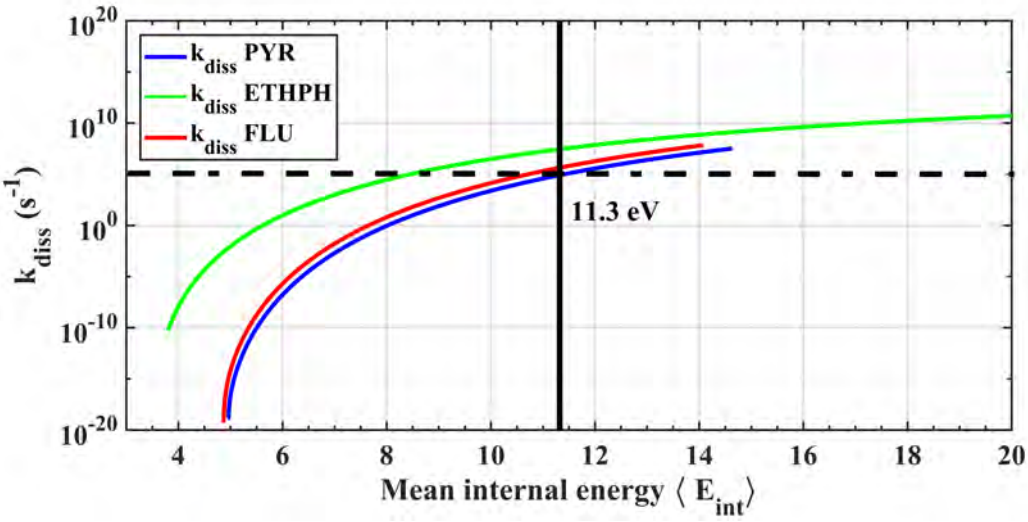

Figure 5.11 Evolution of k_{diss} with internal energy for PYR and FLU (data from West et al. [2018a]) and for ETHPH (estimated in this work).

When relating with the T_{coll} distribution for the corresponding conditions we observe a mean $\langle T_{coll} \rangle = 10^{-5}$ s leading to a $k_{excitation} = 10^{5}\,s^{-1}$. Reporting this $k_{excitation}$ in Figure 5.11 it gives $\langle E_{int} \rangle = 11.3$ eV for PYR which corresponds to the maximum

energy of the ions when using the dissociation rate of PYR.

Conclusion We could fit the PYR CID experimental data using simulated collisional data from Simion, and the dissociation rate reported in West et al. [2018a].

The derived energy transfer parameter η could then be used in the simulations of the FLU data in combination with the dissociation rate of FLU. The comparison between simulations and experimental data is satisfactory, confirming the assumption we made that the isomeric structure do not strongly impact the value of η. With this result, we could determine the dissociation rate for ETHPH.

Chapter VI

Conclusion

This work is dedicated to the study of the differentiation of PAH isomers in mass spectrometry using collision induced dissociation (CID) in a quadrupolar ion trap. It has been carried out in the framework of the NANOCOSMOS project, whose objective is to elucidate the mechanisms involved in the formation of stardust. The AROMA set-up has been developed in NANOCOSMOS to analyse the molecular composition of stardust analogues and provide insights into the chemical pathways leading to the nucleation and growth of dust. AROMA is a hybrid mass spectrometer coupled to a laser desorption/ionization source and is unique to provide a very sensitive analysis of the molecular content, in particular for PAHs.

We have studied the performances of the segmented ion trap of AROMA and created a CID procedure with the aim to disentangle isomers by their fragmentation patterns and decay curves. We have focused on the isomers of $C_{16}H_{10}$ (m/z = 202), which are major species in most of our samples including the Murchison meteorite. More specifically we have selected pyrene, fluoranthene and 9-ethynylphenanthrene, which represent respectively a planar pericondensed structure, a structure including a pentagonal cycle and one with an alkylated sidegroup. Each can reveal a different chemistry in the growth of PAHs and associated dust particles.

A CID procedure was created, which includes an isolation step at one u resolution

in m/z to isolate the ^{12}C parent species, the optimization of the excitation conditions and of the cooling of the ions before and after the CID process. This part has been guided by numerical simulations on the dynamics of the ions inside the ion trap. We found an excitation regime leading to slow heating, which allowed us to observe the fragmentation threshold of the parent ions. However this regime which can be obtained for a very low excitation voltage is sensitive to the stability of the system. This leads to significant noise while averaging decay curves obtained in different experiments. We therefore used excitation conditions at a relatively higher voltage to study the fragmentation of the three isomers at m/z=202.

Determining the characteristic excitation timescale to achieve 50% of the fragmentation of the parent ions, we were able to clearly disentangle 9-ethynylphenanthrene from the other two condensed structures. The latter could be separated at the limit of the systematic errors of the experiments. These results were confirmed when using mixtures of the three pure compounds. In order to improve the contrast in the separation of the two condensed isomers, we increased the voltage and therefore the collisional energy to better observe the carbon-loss channels but we could not improve the differentiation of these isomers.

The CID procedure was applied on complex mixtures, which include samples from a C_2H_2 dusty plasma and of the Allende meteorite. We determined that in these samples the peak at m/z=202 is due to a mix of both pyrene and fluoranthene, except for one sample in the dusty plasma, but we were not able to provide an abundance ratio due to the limited precision of our measurements.

In order to better quantify the dynamics of the CID process in the trap we performed detailed numerical simulations in the case of pyrene. Using the SIMION software package, We determined the frequencies of collisions and the time-dependent distributions of the kinetic energy. A 2D Monte-Carlo algorithm was then developed to model the evolution of the internal energy of the ions in a CID experiment. The dissociation rate of pyrene determined by West *et al* (2018) was then incorporated to take into account the competition between collisional heating and dissociation. The decay curve of pyrene was then adjusted by tuning the η parameter which describes the efficiency of conversion of collisional (kinetic) energy into internal energy in our experimental

conditions. We found that the value of η changes as a function of excitation time. Using the same dependence of η with the energy for fluoranthene, we were able to fit its decay curve. We were also able to derive a dissociation rate for 9-ethynyphenanthrene, which is in agreement with the activation energy predicted for this ion.

This work opens perspectives on the use of CID in AROMA to gain information on the molecular structures of the species analysed by mass spectrometry. It is now necessary to study in a more systematic way the case of m/z=202 and confirm or not that the condensed pyrene and fluoranthene are the dominant ones in most of our samples. If not, other less condensed isomers than 9-ethynylphenanthrene would have to be explored. The case of m/z=200, the main fragment of m/z=202, would be interesting to study in more details. Our preliminary experiments exhibit a different energetics in its fragmentation between the species produced from pyrene and fluoranthene.

It would be useful to generalise the CID procedure over an extended range of masses by determining the relevant parameters as a function of m/z. In the future, the problem related to the 1 kHz excitation resolution limitation might be fixed to extend the capability of AROMA to study dissociation at threshold and derive dissociation rates, which is crucial to quantify the stability of PAHs in astronomical environments (Montillaud *et al* 2013).

Chapter VI

Conclusion [Fr]

Ce travail est dédié à l'étude de la différenciation des isomères de molécules HAP dans des expériences de spectrométrie de masse en utilisant la dissociation induite par collisions (CID) dans un piège à ions quadrupolaire. Il a été réalisé dans le cadre du projet NANOCOSMOS dont l'objectif est d'élucider les mécanismes mis en jeu dans la formation de la poussière d'étoiles. Le dispositif AROMA a été developpé dans le projet afin d'analyser la composition moléculaire d'analogues de poussière d'étoiles et permettre de mieux comprendre les chemins chimiques conduisant à la nucléation et à la croissance de cette poussière. AROMA est un spectromètre de masse hybride couplé à une source désorption/ionisation laser qui est unique pour sa sensibilité en détection du contenu moléculaire des échantillons, en particulier concernant les HAP.

Nous avons étudié les performances du piège à ions segmenté d'AROMA et créé une procédure CID afin de séparer des isomères par leurs fragments et leurs courbes de décroissance. Nous nous sommes focalisés sur les isomères de $C_{16}H_{10}$ ($m/z = 202$), qui sont des espèces dominantes dans la plupart de nos échantillons incluant la météorite Murchison. Plus spécifiquement, nous avons sélectionné le pyrène, le fluoranthène et le 9-ethinylphenanthrène, qui représentent respectivement une structure plane pericondensée, une structure incluant un cycle pentagonal ou un groupement alkylé. Chacune de ces espèces peut révéler une chimie différente dans la croissance des HAP et des particules de poussières associées.

Une procédure CID a été mise en place qui inclut une étape d'isolation avec une résolution de 1 en m/z pour isoler l'espèce isotopologue ^{12}C, l'optimisation des conditions d'excitation et de refroidissement des ions avant et après le processus CID. Cette étape a été guidée par des simulations numériques de la dynamique des ions dans le piège.

Nous avons trouvé un régime d'excitation amenant à un chauffage lent, qui permet d'observer le seuil de fragmentation de l'ion parent. Cependant ce régime nécessite un très faible voltage pour l'excitation et est sensible à la stabilité du système. Ceci induit une source de bruit significative lors du moyennage de courbes de décroissance obtenues lors d'expériences différentes. Nous avons donc privilégié un voltage relativement plus élevé pour étudier la fragmentation des trois isomères à m/z=202.

En déterminant le temps d'excitation caractéristique pour obtenir 50% de fragmentation des ions parents, nous avons pu clairement différencier le 9-ethinylphenanthrène des autres structures condensées. Ces dernières ont pu être séparées à la limite des erreurs systématiques des expériences. Ces résultats ont été confirmés en utilisant des mélanges des trois composés purs. Afin d'augmenter le contraste pour les isomères condensés, nous avons augmenté le voltage et donc l'énergie de collision pour mieux observer les voies de fragmentation impliquant la perte de carbone. Néanmoins, nous n'avons pas réussi à améliorer la différenciation de ces deux isomères.

La procédure CID a été appliquée à des mélanges complexes incluant des échantillons de plasma poussiéreux de C_2H_2 et de la météorite Allende. Nous avons déterminé que dans ces échantillons le pic à m/z=202 peut être attribué à un mélange de pyrène et de fluoranthène, à l'exception d'un échantillon du plasma poussiéreux, mais nous n'avons pas pu déterminer un rapport d'abondance en raison de la précision limitée de nos mesures.

Afin de mieux quantifier la dynamique du processus CID dans le piège, nous avons mené des simulations numériques détaillées pour le cas du pyrène. En utilisant le logiciel SIMION, nous avons déterminé les fréquences de collisions et les distributions d'énergie cinétique dépendant du temps. Un algorithme Monte Carlo à 2D a été développé pour modéliser l'évolution de l'énergie interne des ions dans une expérience CID. Le taux de dissociation déterminé par West *et al* (2018) pour le pyrène a été incorporé dans l'algorithme afin de traiter la compétition entre chauffage par collisions et dissociation. La courbe de décroissance du pyrène a été ensuite ajustée en optimisant la valeur du paramètre η qui décrit l'efficacité de conversion de l'énergie collisionnelle (cinétique) en énergie interne dans nos conditions expérimentales. Nous avons trouvé que la valeur de η dépend du temps d'excitation. En utilisant la même

dépendance de η avec l'énergie pour le fluoranthène, nous avons pu rendre compte de sa courbe de décroissance. Nous avons également extrait un taux de dissociation pour le 9-ethinylphenanthrène qui est en accord avec l'énergie d'excitation prédite pour cet ion.

Ce travail ouvre des perspectives pour l'utilisation de la CID dans le dispositif AROMA afin d'obtenir des informations sur les structures moléculaires des espèces analysées par spectrométrie de masse. Il est maintenant nécessaire d'étudier de manière plus systématique le cas de l'espèce HAP à m/z=202 et de confirmer si les structures condensées pyrène et fluoranthène sont les espèces dominantes dans la plupart de nos échantillons. Sinon, le cas d'isomères moins condensés que le 9-ethinylphenanthrène devra être considéré. Le cas de m/z=200, fragment principal de m/z=202, mériterait une étude plus détaillée. Des expériences préliminaires suggèrent en effet une énergétique de fragmentation différente pour le fragment issu du pyrène comparé à celui du fluoranthène.

Il serait utile de généraliser la procédure CID sur un domaine étendu de masses en déterminant les paramètres pertinents en fonction du rapport m/z. Dans le futur, le problème lié à la limitation à 1 kHz en résolution de l'excitation devra être résolu afin d'augmenter la capacité d'AROMA d'étudier la dissociation au seuil et de déterminer des taux de dissociation, ce qui est crucial pour quantifier la stabilité des PAHs dans les environnements astrophysiques (Montillaud *et al* 2013).

References

References

S. Acevedo, L. B. Gutierrez, G. Negrin, J. C. Pereira, B. Mendez, F. Delolme, G. Dessalces, and D. Broseta. Molecular weight of petroleum asphaltenes: A comparison between mass spectrometry and vapor pressure osmometry. *Energy & fuels*, 19(4): 1548–1560, 2005.

L. J. Allamandola, A. G. G. M. Tielens, and J. R. Barker. Polycyclic aromatic hydrocarbons and the unidentified infrared emission bands: auto exhaust along the milky way. *The Astrophysical Journal*, 290:L25, Mar. 1985. ISSN 0004-637X. doi: 10.1086/184435. URL `https://ui.adsabs.harvard.edu/abs/1985ApJ...290L..25A/abstract`.

R. Arakawa, M. Kobayashi, and T. Nishimura. High-energy collision-induced dissociation of small polycyclic aromatic hydrocarbons. *Journal of mass spectrometry: JMS*, 35(2):178–182, Feb. 2000. ISSN 1076-5174. doi: 10.1002/(SICI)1096-9888(200002)35:2<178::AID-JMS927>3.0.CO;2-S.

M. A. Armitage. *Applications of Quadrupole Ion Storage Mass Spectrometry.* Trent Univ., Peterborough, Ontario, Canada,, m.sc. thesis edition, 1979.

M. A. Armitage, J. E. Fulford, D.-N. Hoa, R. J. Hughes, and R. E. March. The application of resonant ion ejection to quadrupole ion storage mass spectrometry: a study of ion/molecule reactions in the QUISTOR. *Canadian Journal of Chemistry*, 57(16):2108–2113, 1979.

F. Aston. The distribution of intensity along the positive ray parabolas of atoms and molecules of hydrogen and its possible explanation. In *Proc. Cambridge Philos. Soc*, volume 19, page 317, 1919.

S. Barber, A. Morse, I. Wright, B. Kent, N. Waltham, J. Todd, and C. Pillinger. Devel-

opment of a miniature quadrupole ion trap mass spectrometer for the determination of stable isotope ratios. *Advances in Mass Spectrometry*, 14, 1998.

B. P. Basile, B. S. Middleditch, and J. Oro. Polycyclic Aromatic Hydrocarbons in the Murchison Meteorite. In *Lunar and Planetary Science Conference*, Lunar and Planetary Science Conference, page 37, Mar. 1984.

L. Becker, R. J. Poreda, A. G. Hunt, T. E. Bunch, and M. Rampino. Impact event at the Permian-Triassic boundary: Evidence from extraterrestrial noble gases in fullerenes. *Science*, 291(5508):1530–1533, 2001.

O. Berné, N. L. J. Cox, G. Mulas, and C. Joblin. Detection of buckminsterfullerene emission in the diffuse interstellar medium. *Astronomy & Astrophysics*, 605:L1, Sept. 2017. ISSN 0004-6361, 1432-0746. doi: 10.1051/0004-6361/201630325. URL `https://www.aanda.org/articles/aa/abs/2017/09/aa30325-16/aa30325-16.html`.

T. Beyer and D. Swinehart. Algorithm 448: number of multiply-restricted partitions. *Communications of the ACM*, 16(6):379, 1973.

J. H. Beynon, R. M. Caprioli, and T. Ast. Charge localization: The ion kinetic energy spectra of pyrazine, pyrimidine and pyridazine. *Organic Mass Spectrometry*, 6(3): 273–282, 1972. ISSN 1096-9888. doi: 10.1002/oms.1210060305. URL `https://onlinelibrary.wiley.com/doi/abs/10.1002/oms.1210060305`.

L. Biennier. Characterization of circumstellar carbonaceous dust analogues produced by pyrolysis of acetylene in a porous graphite reactor. *Carbon*, 47, 2009. doi: 10.1016/j.carbon.2009.07.050. URL `https://doi.org/10.1016/j.carbon.2009.07.050`.

M. E. Bier and J. E. P. Syka. Ion trap mass spectrometer system and method, May 1995. URL `https://patents.google.com/patent/US5420425A/en`.

P. Boissel, P. de Parseval, P. Marty, and G. Lefèvre. Fragmentation of isolated ions by multiple photon absorption: A quantitative study. *The Journal of chemical physics*, 106(12):4973–4984, 1997.

R. Bonner, G. Lawson, and J. Todd. Ion-molecule reaction studies with a quadrupole ion storage trap. *International Journal of Mass Spectrometry and Ion Physics*, 10 (2):197–203, 1972a.

R. Bonner, G. Lawson, and J. Todd. A low-pressure chemical ionisation source: an application of a novel type of ion storage mass spectrometer. *Journal of the Chemical Society, Chemical Communications*, (21):1179–1180, 1972b.

R. F. Bonner, R. E. March, and J. Durup. Effect of charge exchange reactions on the motion of ions in three-dimensional quadrupole electric fields. *International Journal of Mass Spectrometry and Ion Physics*, 22(1):17–34, Nov. 1976. ISSN 0020-7381. doi: 10.1016/0020-7381(76)80103-9. URL `http://www.sciencedirect.com/science/article/pii/0020738176801039`.

A. A. Boogert, P. A. Gerakines, and D. C. Whittet. Observations of the Icy Universe. *Annual Review of Astronomy and Astrophysics*, 53(1):541–581, 2015. doi: 10.1146/annurev-astro-082214-122348. URL `https://doi.org/10.1146/annurev-astro-082214-122348`.

N. Bruneleau. *Le dispositif PIRENEA dans l'étude des interactions gaz/grain dans la chimie interstellaire: mise en place d'une procédure expérimentale.* PhD Thesis, 2007.

R. Brédy, C. Ortéga, M. Ji, L. Chen, J. Bernard, A. R. Allouche, C. Joblin, A. Cassimi, and S. Martin. PAH radiative cooling and fragmentation kinematics studied within an electrostatic ring. *Journal of Physics: Conference Series*, 583:012042, Jan. 2015. ISSN 1742-6596. doi: 10.1088/1742-6596/583/1/012042. URL `https://doi.org/10.1088%2F1742-6596%2F583%2F1%2F012042`.

D. J. Burke and W. A. Brown. Ice in space: surface science investigations of the thermal desorption of model interstellar ices on dust grain analogue surfaces. *Physical Chemistry Chemical Physics*, 12(23):5947–5969, June 2010. ISSN 1463-9084. doi: 10.1039/B917005G. URL `https://pubs.rsc.org/en/content/articlelanding/2010/cp/b917005g`.

K. L. Busch, R. G. Cooks, and F. McLafferty. *Tandem Mass Spectrometry Busch*. John Wiley & Sons: New York, 1983.

M. Calafat, D. Escaich, R. Clergereaux, P. Raynaud, and Y. Segui. Particle formation in acetylene very low-pressure high density magnetized plasmas. *Applied Physics Letters*, 91(18):181502, 2007.

J. Cami, J. Bernard-Salas, E. Peeters, and S. E. Malek. Detection of C60 and C70 in a young planetary nebula. *Science*, 329(5996):1180–1182, 2010.

Y. Carpentier, G. Féraud, E. Dartois, R. Brunetto, E. Charon, A.-T. Cao, L. d'Hendecourt, P. Bréchignac, J.-N. Rouzaud, and T. Pino. Nanostructuration of carbonaceous dust as seen through the positions of the 6.2 and 7.7 μm AIBs. *Astronomy & Astrophysics*, 548:A40, 2012.

P. Castellanos, O. Berné, Y. Sheffer, M. G. Wolfire, and A. G. G. M. Tielens. C60in PHOTODISSOCIATION REGIONS. *The Astrophysical Journal*, 794(1):83, Sept. 2014. ISSN 0004-637X. doi: 10.1088/0004-637X/794/1/83. URL `https://doi.org/10.1088%2F0004-637x%2F794%2F1%2F83`.

J. Cernicharo, A. M. Heras, A. G. G. M. Tielens, J. R. Pardo, F. Herpin, M. Guélin, and L. B. F. M. Waters. Infrared Space Observatory's Discovery of C_4H_2, C_6H_2, and Benzene in CRL 618. *The Astrophysical Journal*, 546:L123, Jan. 2001. ISSN ['0004-637X']. doi: 10.1086/318871. URL `https://ui.adsabs.harvard.edu/abs/2001ApJ...546L.123C/abstract`.

P. Chaurand, F. Luetzenkirchen, and B. Spengler. Peptide and protein identification by matrix-assisted laser desorption ionization (MALDI) and MALDI-post-source decay time-of-flight mass spectrometry. *Journal of the American Society for Mass Spectrometry*, 10(2):91–103, Feb. 1999. ISSN 1879-1123. doi: 10.1016/S1044-0305(98)00145-7. URL `https://doi.org/10.1016/S1044-0305(98)00145-7`.

I. Cherchneff, J. R. Barker, and A. G. Tielens. Polycyclic aromatic hydrocarbon formation in carbon-rich stellar envelopes. *The Astrophysical Journal*, 401:269–287, 1992.

R. B. Cody and B. S. Freiser. Collision-induced dissociation in a fourier-transform mass spectrometer. *International Journal of Mass Spectrometry and Ion Physics*, 41 (3):199–204, Jan. 1982. ISSN 0020-7381. doi: 10.1016/0020-7381(82)85035-3. URL http://www.sciencedirect.com/science/article/pii/0020738182850353.

M. Compiègne, L. Verstraete, A. Jones, J.-P. Bernard, F. Boulanger, N. Flagey, J. L. Bourlot, D. Paradis, and N. Ysard. The global dust SED: tracing the nature and evolution of dust with DustEM. *Astronomy & Astrophysics*, 525:A103, Jan. 2011. ISSN 0004-6361, 1432-0746. doi: 10.1051/0004-6361/201015292. URL https://www.aanda.org/articles/aa/abs/2011/01/aa15292-10/aa15292-10.html.

C. S. Contreras and F. Salama. Laboratory investigations of polycyclic aromatic hydrocarbon formation and destruction in the circumstellar outflows of carbon stars. *Astrophys. J. Suppl. Ser.*, 208, 2013. doi: 10.1088/0067-0049/208/1/6. URL https://doi.org/10.1088/0067-0049/208/1/6.

R. Cooks. *Beynon. JH; Caprioli, RM: Lester, GR "Metastable Ions"*. Elsevier: Amsterdam, 1973.

R. G. Cooks, L. Hendricks, and J. H. Beynon. Collision-induced dissociation of the lower alcohols. A thermochemical study. *Organic Mass Spectrometry*, 10(8): 625–638, 1975. ISSN 1096-9888. doi: 10.1002/oms.1210100808. URL https://onlinelibrary.wiley.com/doi/abs/10.1002/oms.1210100808.

D. Dahl, J. Delmore, and A. Appelhans. SIMION PC/PS2 electrostatic lens design program. *Review of Scientific Instruments*, 61(1):607–609, 1990.

P. Dawson and D. Douglas. Collisionally Activated Dissociation of Low Kinetic Energy Ions. *Tandem mass spectrometry*, pages 125–148, 1983.

P. Dawson and N. Whetten. Ion storage in three-dimensional, rotationally symmetric, quadrupole fields. II. A sensitive mass spectrometer. *Journal of Vacuum Science and Technology*, 5(1):11–18, 1968.

P. H. Dawson. The collision-induced dissociation of protonated water clusters studied using a triple quadrupole. *International Journal of Mass Spectrometry*

and Ion Physics, 43(2):195–209, July 1982. ISSN 0020-7381. doi: 10.1016/0020-7381(82)80007-7. URL http://www.sciencedirect.com/science/article/pii/0020738182800077.

P. H. Dawson. A study of the collision-induced dissociation of $C_2H_5OH_2^+$ using various target gases. *International Journal of Mass Spectrometry and Ion Physics*, 50(3):287–297, May 1983. ISSN 0020-7381. doi: 10.1016/0020-7381(83)87006-5. URL http://www.sciencedirect.com/science/article/pii/0020738183870065.

P. H. Dawson and N. R. Whetten. Mass Spectroscopy Using RF Quadrupole Fields. In L. Marton and C. Marton, editors, *Advances in Electronics and Electron Physics*, volume 27, pages 59–185. Academic Press, Jan. 1970a. doi: 10.1016/S0065-2539(08)60038-4. URL http://www.sciencedirect.com/science/article/pii/S0065253908600384.

P. H. Dawson and N. R. Whetten. Three-dimensional quadrupole mass spectrometer and gauge, Sept. 1970b. URL https://patents.google.com/patent/US3527939A/en.

K. De Bleecker, A. Bogaerts, and W. Goedheer. Detailed modeling of hydrocarbon nanoparticle nucleation in acetylene discharges. *Physical Review E*, 73(2):026405, 2006.

A. Deckert and S. George. Heating rates required for laser induced thermal desorption studies of surface reaction kinetics. *Surface Science Letters*, 182(1-2):L215–L220, 1987.

H. G. Dehmelt and F. G. Major. Orientation of he_4^+ Ions by Exchange Collisions with Cesium Atoms. *Physical Review Letters*, 8(5):213–214, Mar. 1962. doi: 10.1103/PhysRevLett.8.213. URL https://link.aps.org/doi/10.1103/PhysRevLett.8.213.

C. Deschenaux, A. Affolter, D. Magni, C. Hollenstein, and P. Fayet. Investigations of CH_4, C_2H_2 and C_2H_4 dusty RF plasmas by means of FTIR absorption spectroscopy and mass spectrometry. *Journal of Physics D: Applied Physics*, 32(15):1876, 1999.

F.-X. Desert, F. Boulanger, and J. L. Puget. Interstellar dust models for extinction and emission. *Astronomy and Astrophysics*, 500:313, Oct. 1990. ISSN ['0004-6361']. URL https://ui.adsabs.harvard.edu/abs/1990A&A...237..215D/abstract.

P. Desgroux, X. Mercier, and K. A. Thomson. Study of the formation of soot and its precursors in flames using optical diagnostics. *Proceedings of the Combustion Institute*, 34(1):1713–1738, Jan. 2013. ISSN 1540-7489. doi: 10.1016/j.proci.2012.09.004. URL http://www.sciencedirect.com/science/article/pii/S1540748912003914.

B. Despax, K. Makasheva, and H. Caquineau. Cyclic powder formation during pulsed injection of hexamethyldisiloxane in an axially asymmetric radiofrequency argon discharge. *Journal of applied physics*, 112(9):093302, 2012.

H. Dietze and H. Zahn. Eine Ionenquelle für Massenspektrographischen Laser Mikroanalyse an Festkorpern mit dem Laser Mikrospektral Analysator LMA-1 (An Ion Source for Mass. *Exp. Tech. Phys.*, 20:389, 1972.

H.-J. Dietze, H. Zahn, and W. Schmidt. On the form of ion impulses of a laser ion-source. *International Journal of Mass Spectrometry and Ion Physics*, 21(3-4):231–240, 1976.

L. Ding and S. Kumashiro. Ion motion in the rectangular wave quadrupole field and digital operation mode of a quadrupole ion trap mass spectrometer. *Vacuum Science and Technology*, 21(3):176–181, 2001.

L. Ding, M. Sudakov, F. L. Brancia, R. Giles, and S. Kumashiro. A digital ion trap mass spectrometer coupled with atmospheric pressure ion sources. *Journal of mass spectrometry*, 39(5):471–484, 2004. Publisher: Wiley Online Library.

R. Dorf and R. Bishop. *Modern Control Systems, eight edition*. Addison-Wesley, Menlo Park, CA, Menlo Park, 1998.

V. M. Doroshenko and R. J. Cotter. Ideal velocity focusing in a reflectron time-of-flight mass spectrometer. *Journal of the American Society for Mass Spectrometry*, 10(10):992–999, 1999.

D. J. Douglas. Mechanism of the collision-induced dissociation of polyatomic ions studied by triple quadrupole mass spectrometry. *The Journal of Physical Chemistry*, 86(2):185–191, Jan. 1982. ISSN 0022-3654. doi: 10.1021/j100391a011. URL https://doi.org/10.1021/j100391a011.

L. Drahos and K. Vékey. MassKinetics: a theoretical model of mass spectra incorporating physical processes, reaction kinetics and mathematical descriptions. *Journal of Mass Spectrometry*, 36(3):237–263, 2001. ISSN 1096-9888. doi: 10.1002/jms.142. URL https://onlinelibrary.wiley.com/doi/abs/10.1002/jms.142.

B. T. Draine and A. Li. Infrared Emission from Interstellar Dust. IV. The Silicate-Graphite-PAH Model in the Post-SpitzerEra. *The Astrophysical Journal*, 657(2): 810–837, Mar. 2007. ISSN 0004-637X. doi: 10.1086/511055. URL https://doi.org/10.1086%2F511055.

P. Ehrenfreund and S. B. Charnley. Organic Molecules in the Interstellar Medium, Comets, and Meteorites: A Voyage from Dark Clouds to the Early Earth. *Annual Review of Astronomy and Astrophysics*, 38(1):427–483, Sept. 2000. ISSN 0066-4146. doi: 10.1146/annurev.astro.38.1.427. URL https://www.annualreviews.org/doi/10.1146/annurev.astro.38.1.427.

F. Engelke, J. H. Hahn, W. Henke, and R. N. Zare. Determination of phenylthiohydantoin-amino acids by two-step laser desorption/multiphoton ionization. *Analytical Chemistry*, 59(6):909–912, Mar. 1987. ISSN 0003-2700. doi: 10.1021/ac00133a026. URL https://doi.org/10.1021/ac00133a026.

A. Faccinetto, K. Thomson, M. Ziskind, and C. Focsa. Coupling of desorption and photoionization processes in two-step laser mass spectrometry of polycyclic aromatic hydrocarbons. *Applied Physics A*, 92(4):969–974, Sept. 2008. ISSN 1432-0630. doi: 10.1007/s00339-008-4605-0. URL https://doi.org/10.1007/s00339-008-4605-0.

A. Faccinetto, P. Desgroux, M. Ziskind, E. Therssen, and C. Focsa. High-sensitivity detection of polycyclic aromatic hydrocarbons adsorbed onto soot particles using laser desorption/laser ionization/time-of-flight mass spectrometry: An approach to studying the soot inception process in low-pressure flames. *Combustion and Flame*, 158(2):

227–239, Feb. 2011. ISSN 0010-2180. doi: 10.1016/j.combustflame.2010.08.012. URL http://www.sciencedirect.com/science/article/pii/S0010218010002385.

E. Fischer. Die dreidimensionale Stabilisierung von Ladungsträgern in einem Vierpolfeld. *Zeitschrift für Physik*, 156(1):1–26, Mar. 1959. ISSN 0044-3328. doi: 10.1007/BF01332512. URL https://doi.org/10.1007/BF01332512.

M. Frenklach. Reaction mechanism of soot formation in flames. *Physical Chemistry Chemical Physics*, 4(11):2028–2037, 2002. doi: 10.1039/B110045A. URL https://pubs.rsc.org/en/content/articlelanding/2002/cp/b110045a.

M. Frenklach and E. D. Feigelson. Formation of Polycyclic Aromatic Hydrocarbons in Circumstellar Envelopes. *The Astrophysical Journal*, 341:372, June 1989. ISSN ['0004-637X']. doi: 10.1086/167501. URL https://ui.adsabs.harvard.edu/abs/1989ApJ...341..372F/abstract.

M. Frenklach and H. Wang. Detailed surface and gas-phase chemical kinetics of diamond deposition. *Physical Review B*, 43(2):1520–1545, Jan. 1991. doi: 10.1103/PhysRevB.43.1520. URL https://link.aps.org/doi/10.1103/PhysRevB.43.1520.

J. E. Fulford and R. E. March. A new mode of operation for the three-dimensional quadrupole ion store (QUISTOR): The selective ion reactor. *International Journal of Mass Spectrometry and Ion Physics*, 26(2):155–162, Feb. 1978. ISSN 0020-7381. doi: 10.1016/0020-7381(78)80018-7. URL http://www.sciencedirect.com/science/article/pii/0020738178800187.

D. A. García-Hernández, S. Iglesias-Groth, J. A. Acosta-Pulido, A. Manchado, P. García-Lario, L. Stanghellini, E. Villaver, R. A. Shaw, and F. Cataldo. THE FORMATION OF FULLERENES: CLUES FROM NEW C_{60}, C_{70}, AND (POSSIBLE) PLANAR C_{24} detections IN MAGELLANIC CLOUD PLANETARY NEBULAE. *The Astrophysical Journal*, 737(2):L30, July 2011a. ISSN 2041-8205. doi: 10.1088/2041-8205/737/2/L30. URL https://doi.org/10.1088%2F2041-8205%2F737%2F2%2FL30.

D. A. García-Hernández, N. K. Rao, and D. L. Lambert. ARE C_{60}molecules DETECTABLE IN CIRCUMSTELLAR SHELLS OF R CORONAE BOREALIS STARS? *The Astrophysical Journal*, 729(2):126, Feb. 2011b. ISSN 0004-637X. doi: 10.1088/0004-637X/729/2/126. URL https://doi.org/10.1088%2F0004-637x%2F729%2F2%2F126.

M. Gatchell, M. H. Stockett, P. Rousseau, T. Chen, K. Kulyk, H. T. Schmidt, J. Y. Chesnel, A. Domaracka, A. Méry, S. Maclot, L. Adoui, K. Støchkel, P. Hvelplund, Y. Wang, M. Alcamí, B. A. Huber, F. Martín, H. Zettergren, and H. Cederquist. Non-statistical fragmentation of PAHs and fullerenes in collisions with atoms. *International Journal of Mass Spectrometry*, 365-366:260–265, May 2014. ISSN 1387-3806. doi: 10.1016/j.ijms.2013.12.013. URL http://www.sciencedirect.com/science/article/pii/S1387380613004491.

D. E. Goeringer and S. A. McLuckey. Evolution of ion internal energy during collisional excitation in the Paul ion trap: A stochastic approach. *The Journal of Chemical Physics*, 104(6):2214–2221, Feb. 1996. ISSN 0021-9606. doi: 10.1063/1.471812. URL https://aip.scitation.org/doi/abs/10.1063/1.471812.

D. E. Goeringer, K. G. Asano, S. A. McLuckey, D. Hoekman, and S. W. Stiller. Filtered noise field signals for mass-selective accumulation of externally formed ions in a quadrupole ion trap. *Analytical Chemistry*, 66(3):313–318, Feb. 1994. ISSN 0003-2700. doi: 10.1021/ac00075a001. URL https://doi.org/10.1021/ac00075a001.

X. Guo, H. L. Sievers, and H. F. Grützmacher. Hydrogen atom elimination from polycyclic aromatic hydrocarbons with sustained off-resonance irradiation: a new approach to produce carbon/hydrogen cluster cations $C_nH_x^+$ dedicated to Professor Michael T. Bowers on the occasion of his 60th birthday. *International Journal of Mass Spectrometry*, 185-187:1–10, Apr. 1999. ISSN 1387-3806. doi: 10.1016/S1387-3806(98)14017-4. URL http://www.sciencedirect.com/science/article/pii/S1387380698140174.

J. W. Hager. Axial ejection in a multipole mass spectrometer, Jan. 2001. URL https://patents.google.com/patent/US6177668B1/en.

R. F. Haglund Jr. Microscopic and mesoscopic aspects of laser-induced desorption and ablation. *Applied surface science*, 96:1–13, 1996.

J. H. Hahn, R. Zenobi, and R. N. Zare. Subfemtomole quantitation of molecular adsorbates by two-step laser mass spectrometry. *Journal of the American Chemical Society*, 109(9):2842–2843, Apr. 1987. ISSN 0002-7863. doi: 10.1021/ja00243a057. URL https://doi.org/10.1021/ja00243a057.

J. H. Hahn, R. Zenobi, J. L. Bada, and R. N. Zare. Application of Two-Step Laser Mass Spectrometry to Cosmogeochemistry: Direct Analysis of Meteorites. *Science*, 239 (4847):1523–1525, Mar. 1988. ISSN 0036-8075, 1095-9203. doi: 10.1126/science.239.4847.1523. URL https://science.sciencemag.org/content/239/4847/1523.

M. R. Hammond and R. N. Zare. Identifying the source of a strong fullerene envelope arising from laser desorption mass spectrometric analysis of meteoritic insoluble organic matter. *Geochimica et Cosmochimica Acta*, 72(22):5521–5529, Nov. 2008. ISSN 0016-7037. doi: 10.1016/j.gca.2008.08.008. URL http://www.sciencedirect.com/science/article/pii/S0016703708004948.

E. Herbst and E. F. van Dishoeck. Complex Organic Interstellar Molecules. *Annual Review of Astronomy and Astrophysics*, 47(1):427–480, 2009. doi: 10.1146/annurev-astro-082708-101654. URL https://doi.org/10.1146/annurev-astro-082708-101654.

A. A. Herod, K. D. Bartle, and R. Kandiyoti. Characterization of Heavy Hydrocarbons by Chromatographic and Mass Spectrometric Methods: An Overview. *Energy & Fuels*, 21(4):2176–2203, July 2007. ISSN 0887-0624. doi: 10.1021/ef060642t. URL https://doi.org/10.1021/ef060642t.

F. Hillenkamp, E. Unsöld, R. Kaufmann, and R. Nitsche. A high-sensitivity laser microprobe mass analyzer. *Applied physics*, 8(4):341–348, Dec. 1975. ISSN 1432-0630. doi: 10.1007/BF00898368. URL https://doi.org/10.1007/BF00898368.

F. Hillenkamp, M. Karas, R. C. Beavis, and B. T. Chait. Matrix-assisted laser desorption/ionization mass spectrometry of biopolymers. *Analytical Chemistry*, 63

(24):1193A–1203A, Dec. 1991. ISSN 0003-2700. doi: 10.1021/ac00024a002. URL https://pubs.acs.org/doi/abs/10.1021/ac00024a002.

E. D. Hoffman and V. Stroobant. Mass spectrometry: principles and applications. *West Sussex: John Wiley & Sons, Bruxellas, Bélgica*, 1(2):85, 2007.

R. J. Hughes, R. E. March, and A. B. Young. Multiphoton dissociation of ions derived from 2-propanol in a QUISTOR with low-power CW infrared laser radiation. *International Journal of Mass Spectrometry and Ion Physics*, 42(4):255–263, May 1982. ISSN 0020-7381. doi: 10.1016/0020-7381(82)80070-3. URL http://www.sciencedirect.com/science/article/pii/0020738182800703.

S. N. Jackson, H.-Y. J. Wang, and A. S. Woods. Direct Profiling of Lipid Distribution in Brain Tissue Using MALDI-TOFMS. *Analytical Chemistry*, 77(14):4523–4527, July 2005. ISSN 0003-2700. doi: 10.1021/ac050276v. URL https://doi.org/10.1021/ac050276v.

C. Jager, S. Krasnokutski, A. Staicu, F. Huisken, H. Mutschke, T. Henning, W. Poppitz, and I. Voicu. Identification and Spectral Properties of Polycyclic Aromatic Hydrocarbons in Carbonaceous Soot Produced by Laser Pyrolysis. *The Astrophysical Journal Supplement Series*, 166(2):557–566, Oct. 2006. ISSN 0067-0049. doi: 10.1086/507272. URL https://doi.org/10.1086%2F507272.

C. Jager, H. Mutschke, T. Henning, and F. Huisken. Spectral properties of gas-phase condensed fullerene-like carbon nanoparticles from far-ultraviolet to infrared wavelengths. *Astrophys.J.*, 689:249–259, 2008. doi: 10.1086/592729.

C. Jäger, F. Huisken, H. Mutschke, I. L. Jansa, and T. Henning. FORMATION OF POLYCYCLIC AROMATIC HYDROCARBONS AND CARBONACEOUS SOLIDS IN GAS-PHASE CONDENSATION EXPERIMENTS. *The Astrophysical Journal*, 696(1):706–712, Apr. 2009. ISSN 0004-637X. doi: 10.1088/0004-637X/696/1/706. URL https://doi.org/10.1088%2F0004-637x%2F696%2F1%2F706.

R. E. Kaiser, J. N. Louris, J. W. Amy, R. G. Cooks, and D. F. Hunt. Extending the mass range of the quadrupole ion trap using axial modulation. *Rapid*

Communications in Mass Spectrometry, 3(7):225–229, 1989. ISSN 1097-0231. doi: 10.1002/rcm.1290030706. URL https://onlinelibrary.wiley.com/doi/abs/10.1002/rcm.1290030706.

R. I. Kaiser, D. S. N. Parker, F. Zhang, A. Landera, V. V. Kislov, and A. M. Mebel. PAH Formation under Single Collision Conditions: Reaction of Phenyl Radical and 1,3-Butadiene to Form 1,4-Dihydronaphthalene. *The Journal of Physical Chemistry A*, 116(17):4248–4258, May 2012. ISSN 1089-5639. doi: 10.1021/jp301775z. URL https://doi.org/10.1021/jp301775z.

R. I. Kaiser, D. S. Parker, and A. M. Mebel. Reaction Dynamics in Astrochemistry: Low-Temperature Pathways to Polycyclic Aromatic Hydrocarbons in the Interstellar Medium. *Annual Review of Physical Chemistry*, 66(1):43–67, Apr. 2015. ISSN 0066-426X. doi: 10.1146/annurev-physchem-040214-121502. URL https://www.annualreviews.org/doi/10.1146/annurev-physchem-040214-121502.

M. Karas, D. Bachmann, and F. Hillenkamp. Influence of the wavelength in high-irradiance ultraviolet laser desorption mass spectrometry of organic molecules. *Analytical chemistry*, 57(14):2935–2939, 1985.

M. Karas, D. Bachmann, U. Bahr, and F. Hillenkamp. Matrix-assisted ultraviolet laser desorption of non-volatile compounds. *International journal of mass spectrometry and ion processes*, 78:53–68, 1987.

M. Karas, U. Bahr, A. Ingendoh, E. Nordhoff, B. Stahl, K. Strupat, and F. Hillenkamp. Principles and applications of matrix-assisted UV-laser desorption/ionization mass spectrometry. *Analytica Chimica Acta*, 241(2):175–185, 1990.

P. Kelley, G. Stafford, J. Syka, W. Reynolds, J. Louris, J. Amy, and J. Todd. New advances in the operation of the ion trap mass spectrometer. *San Diego, CA*, page 707, 1985.

T. M. Kertesz, L. H. Hall, D. W. Hill, and D. F. Grant. CE50: Quantifying Collision Induced Dissociation Energy for Small Molecule Characterization and Identification. *Journal of the American Society for Mass Spectrometry*, 20(9):

1759–1767, Sept. 2009. ISSN 1044-0305. doi: 10.1016/j.jasms.2009.06.002. URL http://www.sciencedirect.com/science/article/pii/S1044030509004334.

K. C. Kim, M. Uckotter, J. H. Beynon, and R. G. Cooks. Collision-induced fragmentation of triatomic ions. *International Journal of Mass Spectrometry and Ion Physics*, 15(1):23–35, Sept. 1974. ISSN 0020-7381. doi: 10.1016/0020-7381(74)80083-5. URL http://www.sciencedirect.com/science/article/pii/0020738174800835.

V. Kolotyrkin, M. Tikhomirov, and N. Tunitskii. O MASS-SPEKTRE METANA PRI POVYSHENNYKH DAVLENIYAKH. *DOKLADY AKADEMII NAUK SSSR*, 92 (6):1193–1195, 1953.

R. W. Kondrat and R. G. Cooks. Direct Analysis of Mixtures by Mass Spectrometry. *Analytical Chemistry*, 50(1):81A–92A, Jan. 1978. ISSN 0003-2700. doi: 10.1021/ac50023a781. URL https://doi.org/10.1021/ac50023a781.

L. J. Kovalenko, C. R. Maechling, S. J. Clemett, J. M. Philippoz, R. N. Zare, and C. M. O. Alexander. Microscopic organic analysis using two-step laser mass spectrometry: application to meteoritic acid residues. *Analytical Chemistry*, 64(6): 682–690, Mar. 1992. ISSN 0003-2700. doi: 10.1021/ac00030a021. URL https://doi.org/10.1021/ac00030a021.

E. Kovačević, I. Stefanović, J. Berndt, Y. J. Pendleton, and J. Winter. A candidate analog for carbonaceous interstellar dust: formation by reactive plasma polymerization. *The Astrophysical Journal*, 623(1):242, 2005.

H. W. Kroto, J. R. Heath, S. C. O'Brien, R. F. Curl, and R. E. Smalley. C60: buckminsterfullerene. *Nature*, 318, 1985. doi: 10.1038/318162a0. URL https://doi.org/10.1038/318162a0.

T. Lagarde, Y. Arnal, A. Lacoste, and J. Pelletier. Determination of the EEDF by Langmuir probe diagnostics in a plasma excited at ECR above a multipolar magnetic field. *Plasma Sources Science and Technology*, 10(2):181, 2001.

A. Leger and J. Puget. Identification of the'unidentified'IR emission features of interstellar dust? *Astronomy and Astrophysics*, 137:L5–L8, 1984.

A. Leger, L. D'Hendecourt, and D. Defourneau. Physics of IR emission by interstellar PAH molecules. *Astronomy and Astrophysics*, 216(1-2):148, June 1989. ISSN 0004-6361. URL https://ui.adsabs.harvard.edu/abs/1989A%26A...216..148L/abstract.

J. N. Louris, R. G. Cooks, J. E. P. Syka, P. E. Kelley, G. C. Stafford, and J. F. J. Todd. Instrumentation, applications, and energy deposition in quadrupole ion-trap tandem mass spectrometry. *Analytical Chemistry*, 59(13):1677–1685, July 1987. ISSN 0003-2700. doi: 10.1021/ac00140a021. URL https://doi.org/10.1021/ac00140a021.

G. Malloci, C. Joblin, and G. Mulas. On-line database of the spectral properties of polycyclic aromatic hydrocarbons. *Chemical physics*, 332(2-3):353–359, 2007.

R. E. March. An Introduction to Quadrupole Ion Trap Mass Spectrometry. *Journal of Mass Spectrometry*, 32(4):351–369, 1997. ISSN 1096-9888. doi: 10.1002/(SICI)1096-9888(199704)32:4<351::AID-JMS512>3.0.CO;2-Y. URL https://onlinelibrary.wiley.com/doi/abs/10.1002/%28SICI%291096-9888%28199704%2932%3A4%3C351%3A%3AAID-JMS512%3E3.0.CO%3B2-Y.

R. E. March. Quadrupole ion traps. *Mass spectrometry reviews*, 28(6):961–989, 2009.

R. E. March and J. F. Todd. *Quadrupole ion trap mass spectrometry*, volume 165. John Wiley & Sons, 2005.

R. E. March and J. F. Todd. Radio frequency quadrupole technology: Evolution and contributions to mass spectrometry. *International Journal of Mass Spectrometry*, 377:316–328, Feb. 2015. ISSN 13873806. doi: 10.1016/j.ijms.2014.07.030. URL https://linkinghub.elsevier.com/retrieve/pii/S1387380614002929.

L. G. Marin, S. Bejaoui, M. Haggmark, N. Svadlenak, M. de Vries, E. Sciamma-O'Brien, and F. Salama. Low-temperature Formation of Carbonaceous Dust Grains from PAHs. *The Astrophysical Journal*, 889(2):101, 2020. Publisher: IOP Publishing.

L. Martínez, K. Lauwaet, G. Santoro, J. Sobrado, R. J. Peláez, V. J. Herrero, I. Tanarro, G. Ellis, J. Cernicharo, C. Joblin, and others. Precisely controlled fabrica-

tion, manipulation and in-situ analysis of Cu based nanoparticles. *Scientific reports*, 8(1):7250, 2018.

L. Martínez, G. Santoro, P. Merino, M. Accolla, K. Lauwaet, J. Sobrado, H. Sabbah, R. J. Pelaez, V. J. Herrero, I. Tanarro, M. Agúndez, A. Martín-Jimenez, R. Otero, G. J. Ellis, C. Joblin, J. Cernicharo, and J. A. Martín-Gago. Prevalence of non-aromatic carbonaceous molecules in the inner regions of circumstellar envelopes. *Nature Astronomy*, Oct. 2019. ISSN 2397-3366. doi: 10.1038/s41550-019-0899-4. URL `http://www.nature.com/articles/s41550-019-0899-4`.

B. Maté, G. Molpeceres, M. Jiménez-Redondo, I. Tanarro, and V. J. Herrero. HIGH-ENERGY ELECTRON IRRADIATION OF INTERSTELLAR CARBONACEOUS DUST ANALOGS: COSMIC-RAY EFFECTS ON THE CARRIERS OF THE 3.4 μm ABSORPTION BAND. *The Astrophysical Journal*, 831(1):51, 2016.

P. M. Mayer and C. Poon. The mechanisms of collisional activation of ions in mass spectrometry. *Mass spectrometry reviews*, 28(4):608–639, 2009.

C. N. McEwen, C. Jackson, and B. S. Larsen. Instrumental effects in the analysis of polymers of wide polydispersity by MALDI mass spectrometry. *International Journal of Mass Spectrometry and Ion Processes*, 160(1):387–394, Jan. 1997. ISSN 0168-1176. doi: 10.1016/S0168-1176(96)04501-6. URL `http://www.sciencedirect.com/science/article/pii/S0168117696045016`.

B. A. McGuire, A. M. Burkhardt, S. Kalenskii, C. N. Shingledecker, A. J. Remijan, E. Herbst, and M. C. McCarthy. Detection of the Aromatic Molecule Benzonitrile (c-C_6H_5CN) in the Interstellar Medium. *Science*, 359(6372):202–205, Jan. 2018. ISSN 0036-8075, 1095-9203. doi: 10.1126/science.aao4890. URL `http://arxiv.org/abs/1801.04228`. arXiv: 1801.04228.

F. W. McLafferty and H. D. R. Schuddemage. Minimization of rearrangement reactions in mass spectra by use of collisional activation. *Journal of the American Chemical Society*, 91(7):1866–1868, Mar. 1969. ISSN 0002-7863. doi: 10.1021/ja01035a057. URL `https://doi.org/10.1021/ja01035a057`.

F. W. McLafferty, P. F. Bente, R. Kornfeld, S.-C. Tsai, and I. Howe. Metastable ion characteristics. XXII. Collisional activation spectra of organic ions. *Journal of the American Chemical Society*, 95(7):2120–2129, Apr. 1973a. ISSN 0002-7863. doi: 10.1021/ja00788a007. URL https://doi.org/10.1021/ja00788a007.

F. W. McLafferty, R. Kornfeld, W. F. Haddon, K. Levsen, I. Sakai, P. F. Bente, S.-C. Tsai, and H. D. R. Schuddemage. Metastable ion characteristics. XXIV. Application of collisional activation spectra to the elucidation of organic ion structures. *Journal of the American Chemical Society*, 95(12):3886–3892, June 1973b. ISSN 0002-7863. doi: 10.1021/ja00793a011. URL https://doi.org/10.1021/ja00793a011.

C. E. Melton and H. M. Rosenstock. Collision-Induced Dissociations in the Mass Spectrum of Methane. *The Journal of Chemical Physics*, 26(3):568–571, Mar. 1957. ISSN 0021-9606. doi: 10.1063/1.1743346. URL https://aip.scitation.org/doi/10.1063/1.1743346.

L. Moenke-Blankenburg. New aspects of laser micro-spectral analysis with the LMA 1 from Jena. *Nouvelle Revue d\textquotesingleOptique Appliquée*, 3(5):243–248, Sept. 1972. ISSN 0029-4780. doi: 10.1088/0029-4780/3/5/301. URL https://doi.org/10.1088%2F0029-4780%2F3%2F5%2F301.

B. D. Morrical, D. P. Fergenson, and K. A. Prather. Coupling two-step laser desorption/ionization with aerosol time-of-flight mass spectrometry for the analysis of individual organic particles. *Journal of the American Society for Mass Spectrometry*, 9(10):1068–1073, Oct. 1998. ISSN 1879-1123. doi: 10.1016/S1044-0305(98)00074-9. URL https://doi.org/10.1016/S1044-0305(98)00074-9.

J.-O. Müller, D. S. Su, U. Wild, and R. Schlögl. Bulk and surface structural investigations of diesel engine soot and carbon black. *Physical Chemistry Chemical Physics*, 9(30):4018–4025, 2007.

H. Naraoka, A. Shimoyama, and K. Harada. Isotopic evidence from an Antarctic carbonaceous chondrite for two reaction pathways of extraterrestrial PAH formation. *Earth and Planetary Science Letters*, 184(1):1 – 7, 2000. ISSN 0012-

821X. doi: https://doi.org/10.1016/S0012-821X(00)00316-2. URL http://www.sciencedirect.com/science/article/pii/S0012821X00003162.

B. D. Nourse, K. A. Cox, K. L. Morand, and R. G. Cooks. Collisional activation of pyrene and anthracene in an ion-trap mass spectrometer. *Journal of the American Chemical Society*, 114(6):2010–2016, Mar. 1992. ISSN 0002-7863. doi: 10.1021/ja00032a012. URL https://doi.org/10.1021/ja00032a012.

M. Otsuka, F. Kemper, J. Cami, E. Peeters, and J. Bernard-Salas. Physical properties of fullerene-containing Galactic planetary nebulae. *Monthly Notices of the Royal Astronomical Society*, 437(3):2577–2593, Jan. 2014. ISSN 0035-8711. doi: 10.1093/mnras/stt2070. URL https://academic.oup.com/mnras/article/437/3/2577/1028764.

S. J. Pachuta, H. I. Kenttamaa, T. M. Sack, R. L. Cerny, K. B. Tomer, M. L. Gross, R. R. Pachuta, and R. G. Cooks. Excitation and dissociation of isolated ions derived from polycyclic aromatic hydrocarbons. *Journal of the American Chemical Society*, 110(3):657–665, Feb. 1988. ISSN 0002-7863. doi: 10.1021/ja00211a001. URL https://doi.org/10.1021/ja00211a001.

D. Papanastasiou, O. Belgacem, M. Sudakov, and E. Raptakis. Ion thermalization using pressure transients in a quadrupole ion trap coupled to a vacuum matrix-assisted laser desorption ionization source and a reflectron time-of-flight mass analyzer. *Review of Scientific Instruments*, 79(5):055103, May 2008. ISSN 0034-6748. doi: 10.1063/1.2919881. URL https://aip.scitation.org/doi/10.1063/1.2919881.

W. Paul and H. Steinwedel. A new mass spectrometer without a magnetic field. *Zeitschrift fuer Naturforschung (West Germany) Divided into Z. Nautrforsch., A, and Z. Naturforsch., B: Anorg. Chem., Org. Chem., Biochem., Biophys.,*, 8, 1953.

W. Paul and H. Steinwedel. Notizen: Ein neues Massenspektrometer ohne Magnetfeld. *Zeitschrift für Naturforschung A*, 8(7):448–450, 2014. ISSN 1865-7109. doi: 10.1515/zna-1953-0710. URL https://www.degruyter.com/view/j/zna.1953.8.issue-7/zna-1953-0710/zna-1953-0710.xml.

E. Peeters, L. J. Allamandola, D. M. Hudgins, S. Hony, and A. G. G. M. Tielens. The Unidentified InfraRed Features after ISO. *Astrophysics of Dust*, 309:141, May 2004. ISSN ['1050-3390']. URL https://ui.adsabs.harvard.edu/abs/2004ASPC..309..141P/abstract.

T. Pino, M. Chabot, K. Béroff, M. Godard, F. Fernandez-Villoria, K. C. Le, L. Breuer, M. Herder, A. Wucher, M. Bender, D. Severin, C. Trautmann, and E. Dartois. Release of large polycyclic aromatic hydrocarbons and fullerenes by cosmic rays from interstellar dust - Swift heavy ion irradiations of interstellar carbonaceous dust analogue. *Astronomy & Astrophysics*, 623:A134, Mar. 2019. ISSN 0004-6361, 1432-0746. doi: 10.1051/0004-6361/201834855. URL https://www.aanda.org/articles/aa/abs/2019/03/aa34855-18/aa34855-18.html. Publisher: EDP Sciences.

S. Pizzarello, G. Cooper, and G. Flynn. The nature and distribution of the organic material in carbonaceous chondrites and interplanetary dust particles. *Meteorites and the early solar system II*, 1:625–651, 2006.

S. M. Pyle, L. D. Betowski, A. B. Marcus, W. Winnik, and R. D. Brittain. Analysis of polycyclic aromatic hydrocarbons by ion trap tandem mass spectrometry. *Journal of the American Society for Mass Spectrometry*, 8(2):183–190, Feb. 1997. ISSN 1044-0305. doi: 10.1016/S1044-0305(96)00201-2. URL http://www.sciencedirect.com/science/article/pii/S1044030596002012.

M. Rojo, X. Glad, J. Briancon, J. Margot, S. Dap, and R. Clergereaux. Transport of Dust Particles in Very Low-Pressure Magnetized Plasma Studied by Rapid Imaging. *IEEE Transactions on Plasma Science*, 2019.

G. Rouillé, M. Steglich, P. Hemberger, C. Jäger, and T. Henning. Threshold Dissociation of the 1-ethynylpyrene Cation at Internal Energies Relevant to H i Regions. *The Astrophysical Journal*, 885(1):21, Oct. 2019. ISSN 0004-637X. doi: 10.3847/1538-4357/ab4418. URL https://doi.org/10.3847%2F1538-4357%2Fab4418.

H. Sabbah, L. Biennier, S. J. Klippenstein, I. R. Sims, and B. R. Rowe. Exploring the role of PAHs in the formation of soot: pyrene dimerization. *The Journal of Physical Chemistry Letters*, 1(19):2962–2967, 2010.

H. Sabbah, A. E. Pomerantz, M. Wagner, K. Müllen, and R. N. Zare. Laser Desorption Single-Photon Ionization of Asphaltenes: Mass Range, Compound Sensitivity, and Matrix Effects. *Energy & Fuels*, 26(6):3521–3526, June 2012. ISSN 0887-0624. doi: 10.1021/ef3002313. URL https://doi.org/10.1021/ef3002313.

H. Sabbah, A. Bonnamy, D. Papanastasiou, J. Cernicharo, J. A. Martin-Gago, and C. Joblin. Identification of PAH Isomeric Structure in Cosmic Dust Analogs: The AROMA Setup. *The Astrophysical Journal*, 843(1):34, June 2017. doi: 10.3847/1538-4357/aa73dd. URL https://hal.archives-ouvertes.fr/hal-01582963.

H. Sabbah, M. Carlos, and C. Joblin. Characterization of Large Carbonaceous Molecules in Cosmic Dust Analogues and Meteorites. *Proceedings IAU Symposium No. 350, 2019 ; F. Salama , H.J. Fraser & H. Linnartz, eds.*, 2020.

F. Salama, G. A. Galazutdinov, J. Krełowski, L. J. Allamandola, and F. A. Musaev. Polycyclic Aromatic Hydrocarbons and the Diffuse Interstellar Bands: A Survey. *The Astrophysical Journal*, 526(1):265, Nov. 1999. ISSN 0004-637X. doi: 10.1086/307978. URL https://iopscience.iop.org/article/10.1086/307978/meta.

F. Salama, G. A. Galazutdinov, J. Kre\lowski, L. Biennier, Y. Beletsky, and I.-O. Song. POLYCYCLIC AROMATIC HYDROCARBONS AND THE DIFFUSE INTERSTELLAR BANDS: A SURVEY. *The Astrophysical Journal*, 728(2):154, Feb. 2011. ISSN 0004-637X. doi: 10.1088/0004-637X/728/2/154. URL https://doi.org/10.1088%2F0004-637x%2F728%2F2%2F154.

D. C. Schriemer and L. Li. Detection of High Molecular Weight Narrow Polydisperse Polymers up to 1.5 Million Daltons by MALDI Mass Spectrometry. *Analytical Chemistry*, 68(17):2721–2725, Sept. 1996. ISSN 0003-2700. doi: 10.1021/ac960442m. URL https://doi.org/10.1021/ac960442m.

J. C. Schwartz, J. E. P. Syka, and I. Jardine. High resolution on a quadrupole ion trap mass spectrometer. *Journal of the American Society for Mass Spectrometry*, 2 (3):198–204, May 1991. ISSN 1879-1123. doi: 10.1016/1044-0305(91)80044-8. URL https://doi.org/10.1016/1044-0305(91)80044-8.

K. Sellgren. The near-infrared continuum emission of visual reflection nebulae. *The Astrophysical Journal*, 277:623, Feb. 1984. ISSN ['0004-637X']. doi: 10.1086/161733. URL https://ui.adsabs.harvard.edu/abs/1984ApJ...277..623S/abstract.

K. Sellgren, M. W. Werner, J. G. Ingalls, J. D. T. Smith, T. M. Carleton, and C. Joblin. C60 IN REFLECTION NEBULAE. *The Astrophysical Journal*, 722(1):L54–L57, Sept. 2010. ISSN 2041-8205. doi: 10.1088/2041-8205/722/1/L54. URL https://doi.org/10.1088%2F2041-8205%2F722%2F1%2Fl54.

M. A. Sephton. Organic compounds in carbonaceous meteorites. *Natural product reports*, 19(3):292–311, 2002.

M. A. Sephton. Organic matter in carbonaceous meteorites: past, present and future research. *Philosophical Transactions of the Royal Society of London Series A*, 363 (1837):2729–2742, Dec. 2005. doi: 10.1098/rsta.2005.1670.

B. Shukla and M. Koshi. A highly efficient growth mechanism of polycyclic aromatic hydrocarbons. *Physical Chemistry Chemical Physics*, 12(10):2427–2437, Feb. 2010. ISSN 1463-9084. doi: 10.1039/B919644G. URL https://pubs.rsc.org/en/content/articlelanding/2010/cp/b919644g.

B. Shukla and M. Koshi. Importance of Fundamental sp, sp2, and sp3 Hydrocarbon Radicals in the Growth of Polycyclic Aromatic Hydrocarbons. *Analytical chemistry*, 84(11):5007–5016, 2012a.

B. Shukla and M. Koshi. A novel route for PAH growth in HACA based mechanisms. *Combustion and Flame*, 159(12):3589–3596, 2012b.

B. Shukla, A. Susa, A. Miyoshi, and M. Koshi. Role of Phenyl Radicals in the Growth of Polycyclic Aromatic Hydrocarbons. *The Journal of Physical Chemistry A*, 112 (11):2362–2369, Mar. 2008. ISSN 1089-5639. doi: 10.1021/jp7098398. URL https://doi.org/10.1021/jp7098398.

B. Shushan and R. K. Boyd. Unimolecular and collision induced fragmentations of molecular ions of polycyclic aromatic hydrocarbons. *Organic Mass Spectrometry*, 15

(9):445–453, 1980. ISSN 1096-9888. doi: 10.1002/oms.1210150904. URL https://onlinelibrary.wiley.com/doi/abs/10.1002/oms.1210150904.

M. K. Spencer, M. R. Hammond, and R. N. Zare. Laser mass spectrometric detection of extraterrestrial aromatic molecules: Mini-review and examination of pulsed heating effects. *Proceedings of the National Academy of Sciences*, 105(47):18096–18101, Nov. 2008. ISSN 0027-8424, 1091-6490. doi: 10.1073/pnas.0801860105. URL https://www.pnas.org/content/105/47/18096.

G. C. Stafford, P. E. Kelley, J. E. P. Syka, W. E. Reynolds, and J. F. J. Todd. Recent improvements in and analytical applications of advanced ion trap technology. *International Journal of Mass Spectrometry and Ion Processes*, 60(1): 85–98, Sept. 1984. ISSN 0168-1176. doi: 10.1016/0168-1176(84)80077-4. URL http://www.sciencedirect.com/science/article/pii/0168117684800774.

M. H. Stockett, H. Zettergren, L. Adoui, J. D. Alexander, U. Bērziņš, T. Chen, M. Gatchell, N. Haag, B. A. Huber, P. Hvelplund, A. Johansson, H. A. B. Johansson, K. Kulyk, S. Rosén, P. Rousseau, K. Støchkel, H. T. Schmidt, and H. Cederquist. Nonstatistical fragmentation of large molecules. *Physical Review A*, 89(3):032701, Mar. 2014. doi: 10.1103/PhysRevA.89.032701. URL https://link.aps.org/doi/10.1103/PhysRevA.89.032701.

M. H. Stockett, M. Gatchell, T. Chen, N. de Ruette, L. Giacomozzi, M. Wolf, H. T. Schmidt, H. Zettergren, and H. Cederquist. Threshold Energies for Single Carbon Knockout from Polycyclic Aromatic Hydrocarbons. *The Journal of Physical Chemistry Letters*, 6(22):4504–4509, Nov. 2015a. ISSN 1948-7185. doi: 10.1021/acs.jpclett.5b02080. URL http://arxiv.org/abs/1511.05742. arXiv: 1511.05742.

M. H. Stockett, M. Gatchell, N. de Ruette, L. Giacomozzi, T. Chen, P. Rousseau, S. Maclot, J. Y. Chesnel, L. Adoui, B. A. Huber, U. Bērziņš, H. T. Schmidt, H. Zettergren, and H. Cederquist. Isomer effects in fragmentation of Polycyclic Aromatic Hydrocarbons. *International Journal of Mass Spectrometry*, 392:58–

62, Dec. 2015b. ISSN 1387-3806. doi: 10.1016/j.ijms.2015.09.005. URL http://www.sciencedirect.com/science/article/pii/S1387380615003140.

J. Syka. Commercialization of the Quadrupole Ion Trap (Chapter 4). In *Practical Aspects of Ion Trap Mass Spectrometry: Vol. 1, Fundamentals*. CRC Press Boca Raton, FL, 1995.

J. Syka and W. Fies. A Fourier transform quadrupole ion trap mass spectrometer. In *Proc. 35th ASMS Conf, Mass Spectrometry and Allied Topics*, pages 24–29, 1987.

J. J. Thomson. *Rays of positive electricity and their application to chemical analysis*. The British Institute of Radiology, 1914.

A. Tielens. The molecular universe. *Reviews of Modern Physics*, 85(3):1021, 2013.

P. Voumard, Q. Zhan, and R. Zenobi. A new instrument for spatially resolved laser desorption/laser multiphoton ionization mass spectrometry. *Review of scientific instruments*, 64(8):2215–2220, 1993.

V. Wakelam, E. Bron, S. Cazaux, F. Dulieu, C. Gry, P. Guillard, E. Habart, L. Hornekær, S. Morisset, G. Nyman, V. Pirronello, S. D. Price, V. Valdivia, G. Vidali, and N. Watanabe. H2 formation on interstellar dust grains: The viewpoints of theory, experiments, models and observations. *Molecular Astrophysics*, 9:1–36, Dec. 2017. ISSN 2405-6758. doi: 10.1016/j.molap.2017.11.001. URL http://www.sciencedirect.com/science/article/pii/S2405675817300271.

H. Wang and M. Frenklach. A detailed kinetic modeling study of aromatics formation in laminar premixed acetylene and ethylene flames. *Combustion and flame*, 110(1-2): 173–221, 1997.

B. West, A. Sit, S. Mohamed, C. Joblin, V. Blanchet, A. Bodi, and P. M. Mayer. Dissociation of the Anthracene Radical Cation: A Comparative Look at iPEPICO and Collision-Induced Dissociation Mass Spectrometry Results. *The Journal of Physical Chemistry A*, 118(42):9870–9878, Oct. 2014a. ISSN 1089-5639, 1520-5215. doi: 10.1021/jp505438f. URL https://pubs.acs.org/doi/10.1021/jp505438f.

B. West, F. Useli-Bacchitta, H. Sabbah, V. Blanchet, A. Bodi, P. M. Mayer, and C. Joblin. Photodissociation of Pyrene Cations: Structure and Energetics from $C_{16}H_{10}^{+}$ to C_{14}^{+} and Almost Everything in Between. *The Journal of Physical Chemistry A*, 118(36):7824–7831, Sept. 2014b. ISSN 1089-5639. doi: 10.1021/jp506420u. URL https://doi.org/10.1021/jp506420u.

B. West, B. Lowe, and P. M. Mayer. Unimolecular Dissociation of 1-Methylpyrene Cations: Why Are 1-Methylenepyrene Cations Formed and Not a Tropylium-Containing Ion? *The Journal of Physical Chemistry A*, 122(20):4730–4735, May 2018a. ISSN 1089-5639. doi: 10.1021/acs.jpca.8b02667. URL https://doi.org/10.1021/acs.jpca.8b02667.

B. West, S. C. Rodriguez, A. Sit, S. Mohamad, B. Lowe, C. Joblin, A. Bodi, and P. M. Mayer. Unimolecular reaction energies for polycyclic aromatic hydrocarbon ions. *Physical chemistry chemical physics : PCCP*, 20(10):7195–7205, Mar. 2018b. ISSN 1463-9076. doi: 10.1039/c7cp07369k. URL https://europepmc.org/articles/PMC6031295/.

W. Wiley and I. H. McLaren. Time-of-flight mass spectrometer with improved resolution. *Review of scientific instruments*, 26(12):1150–1157, 1955. Publisher: American Institute of Physics.

R. F. Wuerker, H. Shelton, and R. Langmuir. Electrodynamic containment of charged particles. *Journal of Applied Physics*, 30(3):342–349, 1959.

R. A. Yost and C. G. Enke. Selected ion fragmentation with a tandem quadrupole mass spectrometer. *Journal of the American Chemical Society*, 100(7):2274–2275, Mar. 1978. ISSN 0002-7863. doi: 10.1021/ja00475a072. URL https://doi.org/10.1021/ja00475a072.

R. A. Yost and C. G. Enke. Triple quadrupole mass spectrometry for direct mixture analysis and structure elucidation. *Analytical Chemistry*, 51(12):1251–1264, Oct. 1979. ISSN 0003-2700. doi: 10.1021/ac50048a002. URL https://doi.org/10.1021/ac50048a002.

R. Zenobi. Advances in Surface Analysis and Mass Spectrometry Using Laser Desorption Methods. *CHIMIA International Journal for Chemistry*, 48(3):64–71, 1994.

R. Zenobi, J.-M. Philippoz, R. N. Zare, and P. R. Buseck. Spatially resolved organic analysis of the Allende meteorite. *Science*, 246(4933):1026–1029, 1989.

L. Zhao, R. I. Kaiser, B. Xu, U. Ablikim, M. Ahmed, D. Joshi, G. Veber, F. R. Fischer, and A. M. Mebel. Pyrene synthesis in circumstellar envelopes and its role in the formation of 2d nanostructures. *Nature Astronomy*, 2(5):413–419, May 2018. ISSN 2397-3366. doi: 10.1038/s41550-018-0399-y. URL `https://www.nature.com/articles/s41550-018-0399-y`.

A General principles

A.1 Ion trap theory

A.1.1 Quadrupolar potential

The electrical potential in any point of the QIT can be described using the formalism reported in the book of March and Todd [2005]. It is developed in Cartesian coordinates as follows.

These calculations are done in a trap with no background gas and for a single ion. In case of interactions between ions and the background gas, a higher order term has to be included in the equations.

$$\phi_{x,y,z} = A \cdot (\lambda x^2 + \sigma y^2 + \gamma z^2) + C \tag{23}$$

With $A \cdot (\lambda x^2 + \sigma y^2 + \gamma z^2)$ the term depending on the position in the trap and C is a fixed parameter which is applied to all electrodes to "Float" the system.. Moreover λ, σ and γ are weighting parameters to apply to the different directions.

Satisfying the Laplace condition we get :

$$\nabla^2 \phi = \frac{\partial^2 \phi}{\partial x^2} + \frac{\partial^2 \phi}{\partial y^2} + \frac{\partial^2 \phi}{\partial z^2} = 0 \tag{24}$$

Thus we need the partial derivatives of ϕ:

$$\frac{\partial \phi}{\partial x} = \frac{\partial}{\partial x} \cdot (A(\lambda x^2 + \sigma y^2 + \gamma z^2) + C) \tag{25}$$
$$\frac{\partial \phi}{\partial x} = \frac{\partial}{\partial x} \cdot (A(\lambda x^2)) \tag{26}$$
$$\frac{\partial \phi}{\partial x} = 2 \cdot A\lambda x \tag{27}$$
$$\tag{28}$$

Which leads to the second derivative : $\dfrac{\partial^2 \phi}{\partial x^2}$ (29)

$$\frac{\partial^2 \phi}{\partial x^2} = \frac{\partial \phi}{\partial x} \cdot (2 \cdot A\lambda x) \tag{30}$$
$$\frac{\partial^2 \phi}{\partial x^2} = 2 \cdot A\lambda \tag{31}$$

Hence : (32)

$$\frac{\partial^2 \phi}{\partial y^2} = 2 \cdot A\sigma \qquad \frac{\partial^2 \phi}{\partial z^2} = 2 \cdot A\gamma \tag{33}$$

We get then :

$$\nabla^2 \phi = \frac{\partial^2 \phi}{\partial x^2} + \frac{\partial^2 \phi}{\partial y^2} + \frac{\partial^2 \phi}{\partial z^2} = A(2 \cdot \lambda + 2 \cdot \sigma + 2 \cdot \gamma) = 0 \tag{34}$$

The only way to get $A = 0$ is in the absence of electrical field, therefore the solution is given by:

$$\lambda + \sigma + \gamma = 0 \tag{35}$$

In the case of a linear QIT we can derive:

$$\lambda = -\sigma = 1 \quad \Rightarrow \quad \gamma = 0 \tag{36}$$

Thus we can retrieve the quadrupolar potential by substituting these values in the equation 23 gives :

$$\phi_{x,y} = A \cdot (x^2 - y^2) + C \tag{37}$$

A.1.2 Quadrupolar hyperbolic geometry

In the case of hyperbolic electrodes, their shape can be described by :

$$\begin{aligned} \frac{x^2}{x_0^2} - \frac{y^2}{a^2} &= \quad 1 \quad \Rightarrow \quad \text{in the x direction} \\ \frac{x^2}{b^2} - \frac{y^2}{y_0^2} &= -\ 1 \quad \Rightarrow \quad \text{in the y direction} \end{aligned}$$

$$\begin{aligned} \frac{x^2}{x_0^2} - \frac{y^2}{a^2} &= \quad 1 \quad \Rightarrow \quad \text{in the x direction} \\ \frac{x^2}{b^2} - \frac{y^2}{y_0^2} &= -\ 1 \quad \Rightarrow \quad \text{in the y direction} \end{aligned} \tag{38}$$

In most cases the electrodes are dispatched around a circle of radius r_0. In order to achieve a real quadrupolar potential we need $x_0 = y_0$, thus symmetrically it's easier to have a hyperbolas with condition :

$$x_0 = y_0 = r_0 \tag{39}$$

which changes Equation 38 into :

$$\begin{aligned} \frac{x^2}{r_0^2} - \frac{y^2}{r_0^2} &= \quad 1 \quad \Rightarrow \quad \text{in the x direction} \\ \frac{x^2}{r_0^2} - \frac{y^2}{r_0^2} &= -\ 1 \quad \Rightarrow \quad \text{in the y direction} \end{aligned}$$

$$\begin{aligned} x^2 - y^2 &= \quad r_0^2 \quad \Rightarrow \quad \text{in the x direction} \\ x^2 - y^2 &= -\ r_0^2 \quad \Rightarrow \quad \text{in the y direction} \end{aligned} \tag{40}$$

From earlier we know that the potential can be seen as the difference between the

potential from the two directions :

$$\begin{aligned} \phi_{x,y} = &\quad A \cdot (x^2 - y^2) &&+ C \\ \phi_{x,y} = &\quad Ax^2 - Ay^2 &&+ C \text{ With } C \text{ being a unknown constant} \end{aligned} \tag{41}$$

We can write :

$$\begin{aligned} \phi_{x,y} = &\quad Ax^2 + C - Ay^2 &&+ C \text{ Whence :} \\ \phi_{x,y} = &\quad \phi_x - \phi_y \end{aligned}$$

We can then define the potential on the surface by using the special cases respectively $y = 0$, $x_0 = r_0$ and $x = 0$, $y_0 = r_0$.

$$\phi_x = \quad A \cdot (r_0^2) \quad + C \tag{42}$$

$$\phi_y = \quad A \cdot (-r_0^2) \quad + C \tag{43}$$

Which gives :

$$\begin{aligned} \phi^0_{x,y} = &\quad \phi_x - \phi_y \\ \phi^0_{x,y} = &\quad 2A \cdot (r_0^2) && (44) \\ A = &\quad \frac{\phi_0}{2r_0^2} && (45) \end{aligned}$$

Whence the general equation of the potential in the trap :

$$\phi^0_{x,y} = \quad \frac{\phi_0}{2r_0^2} \cdot (x^2 - y^2) \tag{46}$$

A.1.3 Quadrupolar trap : ion motion

The potential being described, we have to describe the motion of the ions in such a potential, to simplify the expressions we can consider the expression on one component,

say x :

$$\phi^0_{x,y} = \frac{\phi_0 x^2}{2r_0^2} \tag{47}$$

$$\tag{48}$$

Since force = mass × acceleration we want the force deriving from the potential which is of the form :

$$F_x = -e\left(\frac{d\phi}{dx}\right)_y \quad \text{where } \frac{d\phi}{dx} : \tag{49}$$

$$\frac{d\phi}{dx} = \frac{2\phi_0 x}{2r_0^2} \tag{50}$$

$$\frac{d\phi}{dx} = \frac{\phi_0 x}{r_0^2} \quad \text{Whence} \tag{51}$$

$$F_x = -e\frac{\phi_0 x}{r_0^2} \tag{52}$$

From the second law of Newton we get :

$$m\left(\frac{d^2x}{dt^2}\right) = -e\frac{\phi_0 x}{r_0^2} \tag{53}$$

In the trapping conditions of the trap the potential is of form :

$$\phi_0 = U + V\cos(\omega t) \text{(we prefer to use this form of potential)} \tag{54}$$

With U the DC voltage applied on the electrodes and V the AC voltage (0-to-peak amplitude).

$$m\left(\frac{d^2x}{dt^2}\right) = -e\frac{(U + V\cos(\omega t))x}{r_0^2} \tag{55}$$

Which we can separate into two terms :

$$\left(\frac{d^2x}{dt^2}\right) = -\left(\frac{eU}{mr_0^2} + \frac{(eV\cos(\omega t))}{mr_0^2}\right)x \tag{56}$$

A.1.4 Mathieu Equation

We will use the mostly used canonical form of the Mathieu equation which form is :

$$\frac{d^2u}{d\xi^2} + (a_u - 2q_u cos(2\xi))\, u = 0 \tag{57}$$

Where ξ is a dimensionless parameter equal to $\frac{\omega t}{2}$, t being time and ω a frequency. Thus u is the displacement (in our case x). Then a_u and q_u are dimensionless stability parameters which we call trapping parameters since they are the parameters that will tune the trapping of a specific ion with a specific mass m depending on the frequency ω, DC U and AC V voltage. We can get $\frac{d^2}{d\xi^2}$ from :

$$\frac{d}{dt} = \frac{d}{d\xi} \cdot \frac{d\xi}{dt} = \frac{d}{d\xi} \cdot \frac{d\left(\frac{\omega t}{2}\right)}{dt} \tag{58}$$

$$\frac{d}{dt} = \frac{d}{d\xi} \cdot \frac{\omega}{2} = \frac{\omega}{2} \cdot \frac{d}{d\xi} \tag{59}$$

Whence

$$\frac{d^2}{dt^2} = \frac{d}{dt} \cdot \frac{d}{dt} = \left(\frac{\omega}{2} \cdot \frac{d}{d\xi}\right) \cdot \left(\frac{\omega}{2} \cdot \frac{d}{d\xi}\right) \tag{60}$$

$$\frac{d^2}{dt^2} = \left(\frac{\omega^2}{4} \cdot \frac{d^2}{d\xi^2}\right) \quad \text{Whence :} \tag{61}$$

$$\frac{d^2u}{dt^2} = \frac{\omega^2}{4} \cdot \frac{d^2u}{d\xi^2} \tag{62}$$

Then we can identify this equation to Equation 57 giving :

$$\frac{d^2u}{dt^2} = -\frac{\omega^2}{4}\,(a_u - 2q_u cos(2\xi))\, u \tag{63}$$

$$\frac{d^2u}{dt^2} = -\left(\frac{\omega^2}{4}a_u - 2\frac{\omega^2 q_u}{4}cos(2\xi)\right) u \tag{64}$$

$$a_x = \frac{4eU}{mr_0^2\omega^2} \qquad (65)$$
$$q_x = -\frac{2eV}{mr_0^2\omega^2}$$

A.2 Time of Flight theory

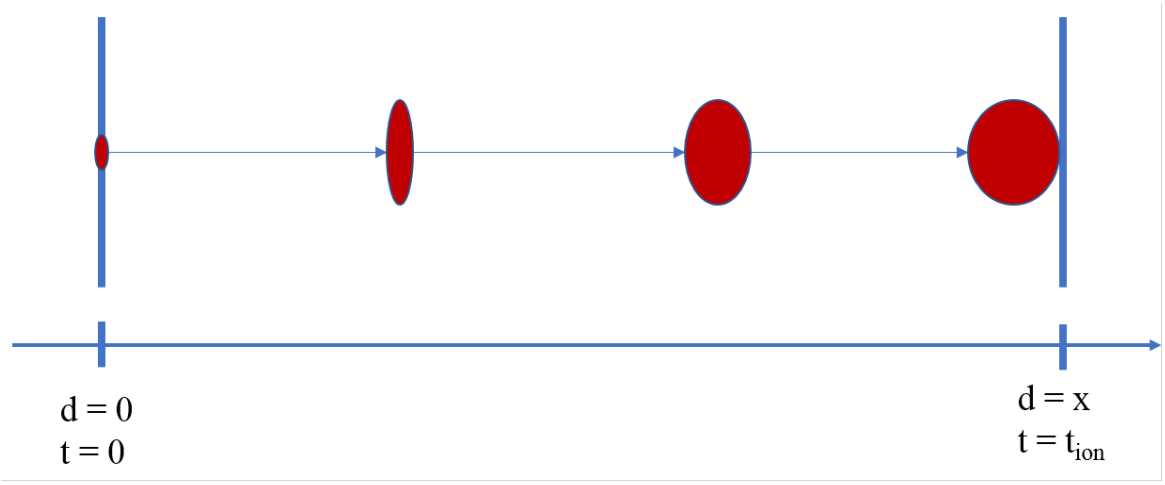

Figure A.1 Principle scheme of a TOF. Ions are sent at time t = 0 from a certain point with a given energy E_k = z· U. They travel to the point d = x and depending on their m/z arrive at different times t = t_{ion}. We can then recover the values of m/z for the ions depending on their time of arrival by using the set of equations presented below.

The TOF-MS, is based on the measurements of the time of flight of chemical species (atom, radical or molecules) in a drift tube. Ions are accelerated toward the detector, through the drift tube, by applying one or more uniform electrical fields U. To simplify, we will use one electrical field for the equations. The resulting potential energy E_{pot} is given by:

$$E_{pot} = z \cdot U$$

where z is the charge and U the voltage used to apply the uniform electrical field. This potential energy is converted to kinetic energy once the ions are accelerated. The

kinetic energy transmitted to the ions is given by:

$$\begin{aligned} E_p = E_k = z \cdot U &= \frac{1}{2} \cdot m_{ion} v_{ion}^2 \\ v_{ion} &= \sqrt[2]{\frac{2 \cdot z \cdot U}{m_{ion}}} \end{aligned} \tag{66}$$

This means that the kinetic energy E_k of the ions depends on their charge z. Two cases can be differentiated. Depending on the charge z being positive or negative the direction of the force F is, respectively, either with or against the direction of the electrical field Secondly, depending on the number of electrical charge the E_k of the ions will be different: if $z = 2$ the E_k will double, which is interesting for the differentiation of ions reaching different ionization states. As an example an actual ion of 16 ua mass with z = 1 or a doubly charged ion z = 2 with mass of 32 u will arrive at the same time on the detector. The distance being the same for all the ions they will arrive after a time t_{ion} depending on their mass from equation 67.

$$\begin{aligned} t_{ion} &= \frac{d}{v} \\ t_{ion} &= \frac{d}{\sqrt{\frac{2 \cdot z \cdot U}{m_{ion}}}} = \frac{d \cdot \sqrt{m_{ion}}}{\sqrt{2 \cdot z \cdot U}} \end{aligned} \tag{67}$$

Equation shows that the time of flight is proportional to the the square root of the m/z ratio. If only singly charged ions are present, the lightest ones reach the detector first. From this time we can derive the m/z of the ion:

$$\begin{aligned} \frac{2 \cdot z \cdot U}{m_{ion}} &= \frac{d^2}{t_{ion}^2} \\ m_{ion} &= \frac{2 \cdot z \cdot U \cdot t_{ion}^2}{d^2} \end{aligned} \tag{68}$$

This m_{ion} is the mass of the ion arriving on the detector after a time t_{ion} if its departure happened at the time $t_0 = 0\,s$. Since achieving an exact synchronization is hardly possible it can be calibrated by using ions with known mass that will solve the

equation.

$$\begin{aligned} m_{ion}^{real} &= \frac{2 \cdot z \cdot U \cdot t_{ion}^2}{d^2} + t_0 \\ m_{ion}^{real} &= \frac{2 \cdot z \cdot U}{d^2} \cdot t_{ion}^2 + t_0 \\ m_{ion}^{real} &= A \cdot t_{ion}^2 + B \end{aligned}$$

Using two known molecules we can assert the values of the A and B parameters and thus find the calibration curve of the mass spectrometer. Ions with similar m/z will arrive to the detector with a time of flight spread. This is due to the initial conditions of ions in the extraction region. The assumptions made to express the time of flight as in 67 consider that all ions are created in the same parallel plane to the electrodes and so they acquire the same kinetic energy at the same time. In practice the things occur differently, the ions generated in the ion source are created at different times and accelerated with an initial kinetic energy spread. The resulting signal of the ion arrival with the same m/z is a peak with certain width defining the resolution of the instrument.

B Other relevant experiments

B.1 Off resonance experiments.

When performing the first CID experiments, some off resonance experiments were performed with low resolution isolation (no ejection of the ^{13}C isotope and $\tilde{5}\%$ of fragmentation) leading to the formation of other fragments. Figure B.1 presents the case of an off resonance DE at 1500 mV and with different excitation times. Increasing the excitation time leads to a lower survival yield, as expected. Due to the width of the excitation pulse (in m/z) we know that we are exciting at least the fragments -H_x from pyrene. This implies that these experiments cannot be used to investigate fragmentation pathways and the origin of fragments because both parents and fragments can be excited simultaneously.

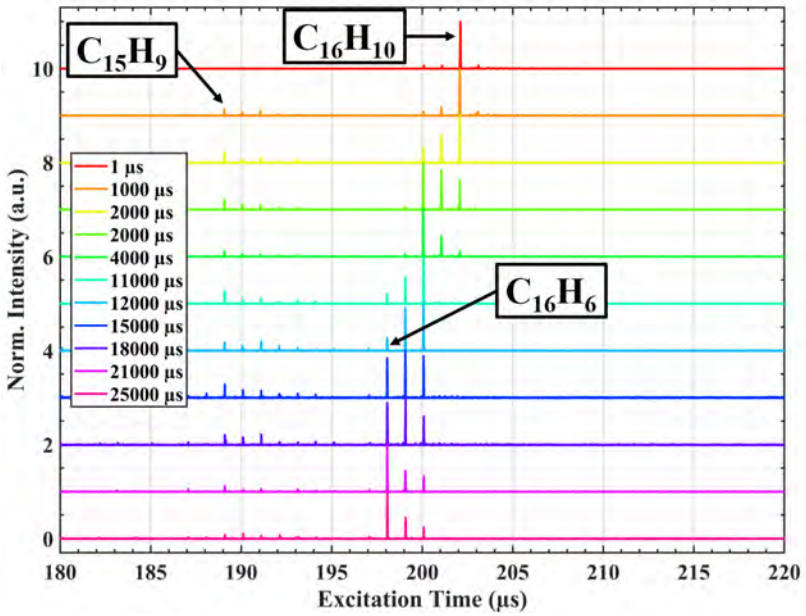

Figure B.1 CID spectra of pyrene cations as a function of the excitation time for an off resonance DE at 180 kHz (corresponding secular frequency of 210 m/z) and 1500 mV.

A second type of experiments consists in fixing the excitation time and varying the excitation amplitude as presented in Figure B.2 and Figure B.3. These present two cases in which the excitation frequency is centered at lower or higher frequency relative to the secular frequency of the parent ions, exciting the ions around $m/z = 210$ and $m/z = 199$, respectively. In the later case and for a long interaction time, the H loss fragments ($m/z = 201.07$) are 100% dissociated and do not appear in the mass spectra.

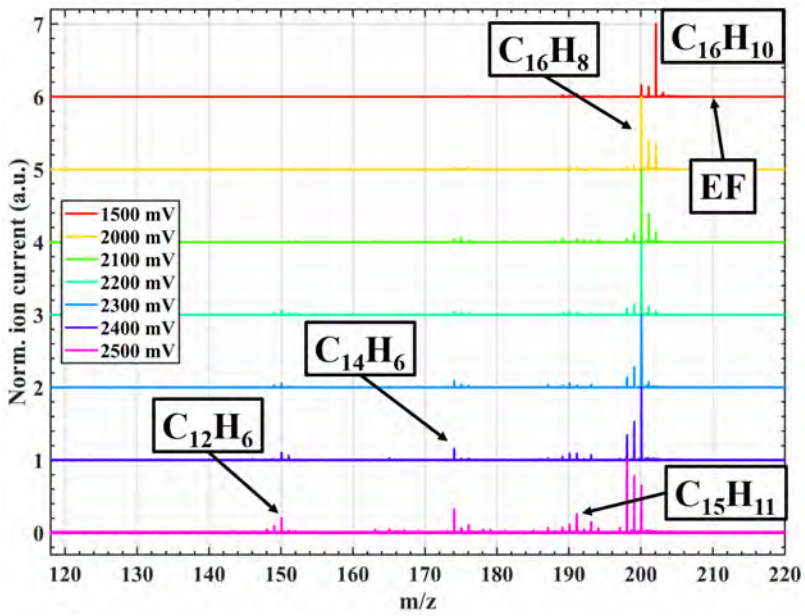

Figure B.2 Off resonance CID experiments of pyrene cations with an excitation frequency at 180 kHz (centered on m/z = 210) applied for 2 ms in the presence of He background gas.

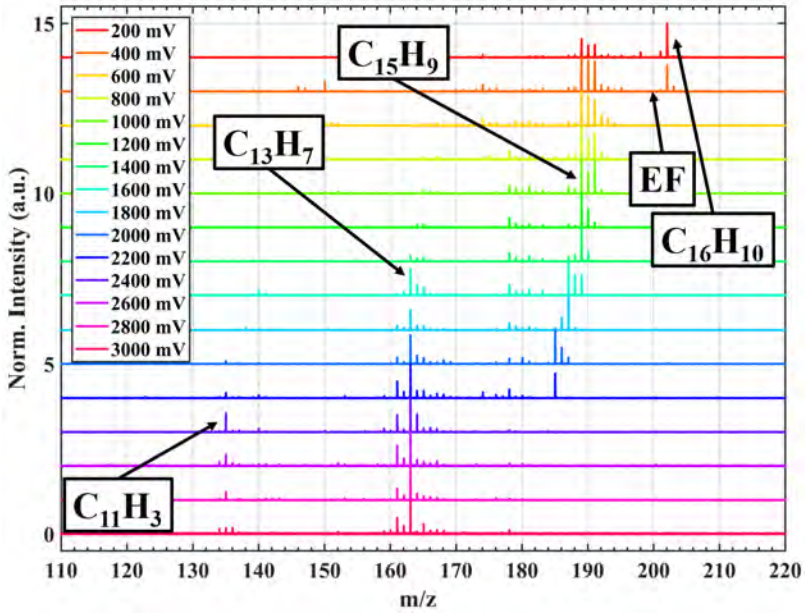

Figure B.3 Off resonance CID experiments of pyrene cations with an excitation frequency at 190 KHz (centered on m/z = 199) applied for 10 ms in the presence of He background gas.

In Table 11, The species referred by a star * are identified as reactivity products with oxygen (mainly H_2O but also O_2) in the trap. This reactivity involves the fragments of the pyrene cation which contain an odd number of hydrogens (Bruneleau [2007]). Further fragmentation by CID of these reactivity products is likely the explanation for the fragments with an odd number of carbon (e.g. $C_{15}H_x$). Other explanation

would involve the knock out process as presented in subsection 3.1.2 but the excitation energies we can achieved in our trap are not high enough to favour this process. The idea of products induced by reactivity in the trap is also strengthened by the evolution of the abundance of the odd number of carbon species as a function of time (Figure B.1) and DE frequency in off resonance excitation (Figures B.2 and B.3).

m/z peak	This work	Attribution
		H_x losses
201.07 ($C_{16}H_9$)	√	[b,c,d,e,f](202 - H)
200.06 ($C_{16}H_8$)	√	[b,c,d,e,f](202 - 2H/H_2)/[c,e,f](201 - H)
*219.08 ($C_{16}H_{11}O$)	√	(201 + H_2O)
*217.06 ($C_{16}H_9O$)	√	(219 - 2H)
*205 ($C_{15}H_9O$)	√	(217 - C) / (201-C+O)
		CH_x losses
*191.06 ($C_{15}H_{11}$)	√	(219 - CO)
189 ($C_{15}H_9$)	√	[b](202 - CH)
*189 ($C_{15}H_9$)	√	(217 - CO)
188 ($C_{15}H_8$)	√	[b](202 - CH_2)
*188 ($C_{15}H_8$)	√	(217 - HCO)
187 ($C_{15}H_7$)	√	[b](202 - CH_3)
*187 ($C_{15}H_7$)	√	(217 - H_2CO) (215 - CO)
186 ($C_{15}H_6$)	√	[a,b](202 - CH_4)
*186 ($C_{15}H_6$)	√	(215 - HCO)
185 ($C_{15}H_5$)	√	[a](200 - CH_3)
*185 ($C_{15}H_5$)	√	(215 - H_2CO) (213 - CO)
184 ($C_{15}H_4$)	∅	[a](200 - CH_4)
*184 ($C_{15}H_4$)	√	(213 - HCO)
		C_2H_x losses
177 ($C_{14}H_9$)	√	[c](202 - C_2H)
*177 ($C_{14}H_9$)	√	(205 - CO)
		C_3H_x losses
*167 ($C_{12}H_7O$)	√	(219 - C_4H_4)
		C_5H_x losses
139 ($C_{11}H_7$)	∅	[a,b](202 - C_5H_3)
138 ($C_{11}H_6$)	√	[a](202 - C_5H_4)
137 ($C_{11}H_5$)	√	[a,b](202 - C_5H_5)
135 ($C_{11}H_3$)	√	[a](200 - C_5H_7)
134 ($C_{11}H_2$)	√	[a](202 - C_5H_8)

Table 11 Analysis of specific m/z species detected in our CID experiments and possible assignment. * m/z peaks correspond to species which we attributed to products of the reactivity in the trap of pyrene fragments with H_2O and potentially O_2 and their subsequent fragmentation by CID (see Figure B.3). Previous results published in the literature have also been gathered corresponding to [a]Shushan and Boyd [1980], [b]Pachuta et al. [1988], [c]Nourse et al. [1992], [d]Pyle et al. [1997], [e]Guo et al. [1999], and [f] West et al. [2014b] illustrating the complexity of the dissociation patterns.

B.2 On resonance procedure applied with Helium

Experiments were performed at high voltages and long excitation times using helium with the aim to stretch the time corresponding to SY = 0.5. Theoretically there is a factor 10 between the achievable E_{com} between He and Ar, which leads to achievable longer excitation time when using He. Here the SY = 0.5 at DE = 500 mV is reached at 350 μs with Ar while it is reached at 5000 μs with He.

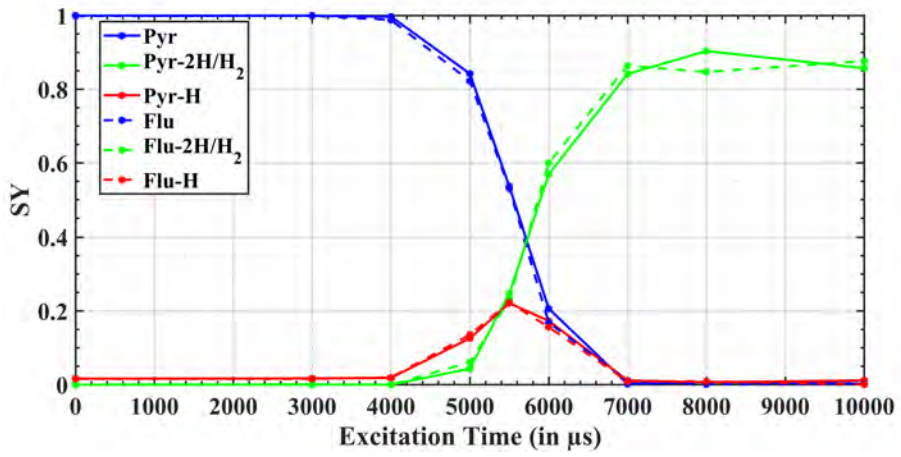

Figure B.4 Example of decay curve of PYR (continuous line) and FLU (dashed line) at 500 mV using He instead of Ar.

As observed earlier in the case of Ar, the decay curves of PYR and FLU are too close to each other to differentiate the two isomers. with values at 5500 and 5750 μs for SY = 0.5 in the case of PYR and FLU, respectively.

TITLE : Collision induced dissociation of polycyclic aromatic hydrocarbons in a quadrupolar ion trap. Differentiation of isomeric structures in cosmic dust components

---

ABSTRACT : Polycyclic aromatic hydrocarbons (PAH) are large carbonaceous molecules that are the subject of investigation in various fields from astrochemistry to environmental science. Being a major constituent of cosmic dust, they play a key role in regions of star formation, where their infrared emission is excited by ultraviolet photons. However, the mechanisms involved in their formation remain poorly understood. In simulation experiments in the laboratory as in meteorites, the mass $m/z = 202.08$ corresponding to the species $C_{16}H_{10}$, has been identified as a key species in the growth of these PAHs. This chemical formula includes several isomeric structures that need to be differentiated.

We used the AROMA molecular analyzer to study the differentiation of $C_{16}H_{10}$ isomers by collision-induced dissociation (CID), in the case of fluoranthene and pyrene (two compact structures) and that of 9-ethynylphenanthrene (structure with an alkyl group). The various experimental parameters controlling the CID were explored in order to determine optimized conditions for our experimental conditions. At low collision energy, we have shown that the criterion of 50 % dissociation of parent ions can be used to differentiate condensed from non-condensed structures but is more difficult to differentiate between condensed structures. The procedure has been applied to individual species, their mixtures, and more complex samples of meteorite (Allende) and laboratory analogues of cosmic dust (dusty plasma).

We have modeled the dynamics of the ions in the trap and extracted frequency and energy distributions of collisions. The competition with the dissociation rate was treated by Monte Carlo method. The model fit of the pyrene dissociation curve quantified the parameter η of transfer of kinetic energy into internal energy. The fluoranthene dissociation curve could be modeled using the same values for η. Finally, we were able to determine the dissociation rate of 9-ethynylphenanthrene, which is not yet known.

KEY WORDS : Laboratory astrophysics, polycyclic aromatic hydrocarbons, ion traps, dissociation by collisions, simulations

AUTEUR : Mickaël CARLOS

TITRE : Dissociation induite par collisions d'hydrocarbures aromatiques polycycliques dans un piège à ions quadripolaire. Séparation des structures isomériques des composantes de la poussière cosmique.

DIRECTEUR de THESE : Christine JOBLIN et Hassan SABBAH

LIEU ET DATE DE SOUTENANCE : Toulouse, 3 février 2020

Les hydrocarbures aromatiques polycycliques (HAP) sont des molécules carbonées de grande taille dont l'étude intéresse différents champs disciplinaires qui vont de l'environnement à l'astrochimie. Constituant majeur de la poussière cosmique, elles jouent un rôle clé dans les régions de formation stellaire, où leur émission infrarouge est excitée par les photons ultraviolets. Les mécanismes impliqués dans leur formation restent néanmoins mal connus. Dans les expériences de simulation en laboratoire comme dans les météorites, la masse $m/z = 202.08$ correspondant à l'espèce $C_{16}H_{10}$, a été identifiée comme une espèce clé dans la croissance de ces HAP. Cette espèce comprend plusieurs structures isomériques qu'il est important de pouvoir différencier.

Nous avons utilisé l'analyseur moléculaire AROMA pour étudier la différentiation des isomères de $C_{16}H_{10}$ par dissociation induite par collisions (CID), dans le cas du fluoranthène et du pyrène (structures compactes) et celui du 9-éthynylphenanthrène (structure avec un groupe alkyl). Les différents paramètres contrôlant la CID ont été explorés afin de déterminer des conditions optimisées pour notre dispositif expérimental. A basse énergie de collision, nous avons montré que le critère de 50 % de dissociation des ions parents peut être utilisé pour différencier les structures condensées des non condensées et plus difficilement pour différencier les structures condensées entre elles. La procédure a été appliquée sur des espèces individuelles, leurs mélanges et des échantillons plus complexes de météorite (Allende) et d'analogues en laboratoire de poussière cosmique (plasma poussiéreux).

Nous avons modélisé la dynamique des ions dans le piège et extrait des distributions de fréquence et d'énergie de collisions. La compétition avec le taux de dissociation a eté traitée par méthode Monte Carlo. L'ajustement par le modèle de la courbe de dissociation du pyrène a permis de quantifier le paramètre η de transfert d'énergie cinétique en énergie interne. La courbe de dissociation du fluoranthène a pu être modélisée en utilisant les mêmes valeurs pour η. Enfin nous avons pu déterminer le taux de dissociation du 9-éthynylphenanthrène, qui n'est pas connu à ce jour.

MOTS CLÉS : astrophysique de laboratoire, hydrocarbures aromatiques polycycliques, piège à ions, dissociation par collisions, simulations

DISCIPLINE : Astrophysique, Sciences de l'Espace, Planétologie

---

Institut de Recherche en Astrophysique et Planétologie - 9 av. du colonel Roche - 31028 Toulouse
Laboratoire Collision Agrégat Réactivité - 118, route de Narbonne- Bât. 3R1 - 31062 Toulouse